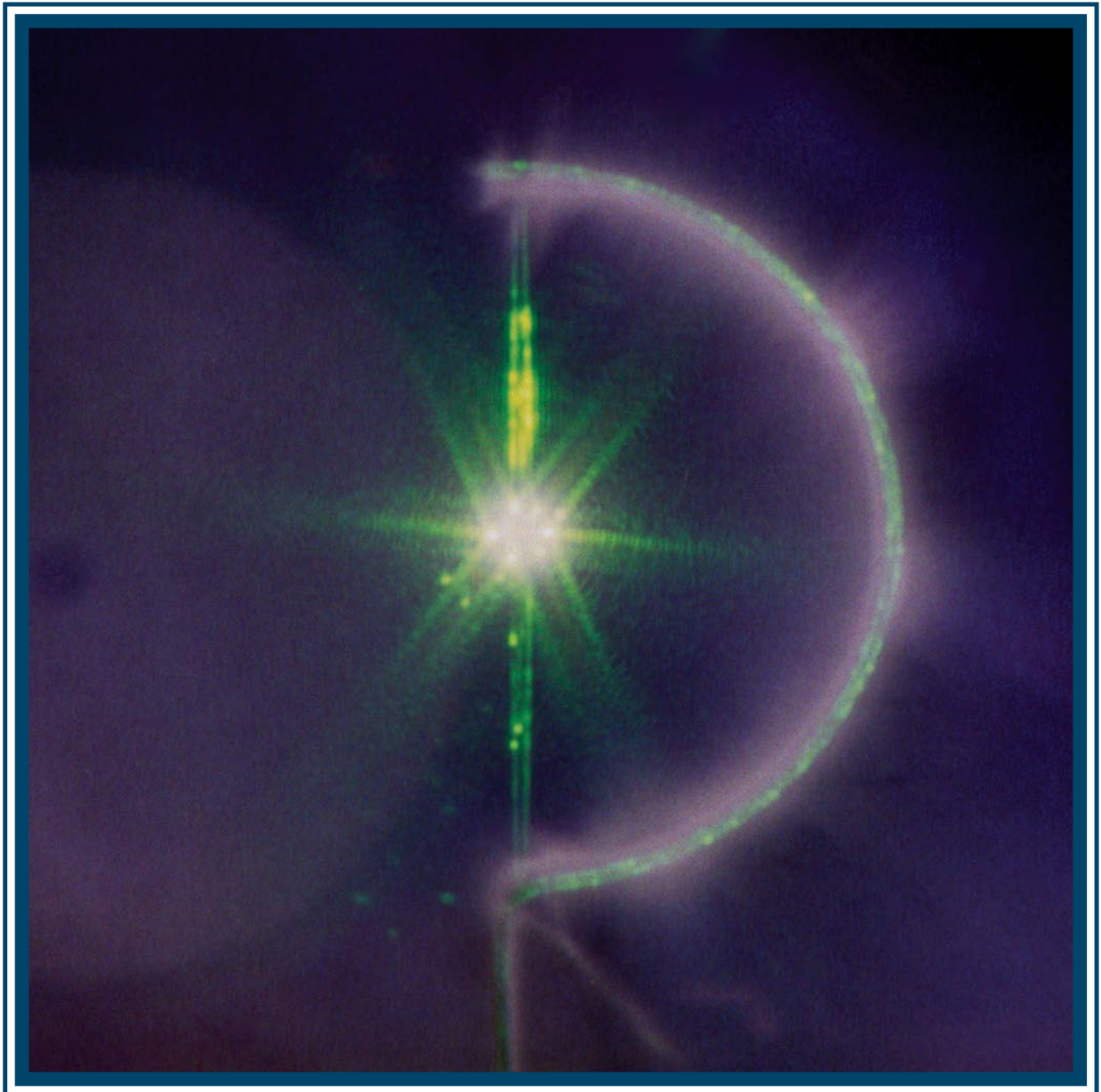# LLE Review

Quarterly Report

UR
LLE

About the Cover:

The cryogenic D_2 and DT targets imploded on the OMEGA laser are mounted at the center of a beryllium "C" mount using four strands of spider silk. The C mount provides rigidity for target alignment while keeping the mass of the frame as far as possible from the target surface to minimize beam obscuration and thermal perturbations that might affect the layer quality. The silks provide a low-mass, non-rigid option for mounting the capsule to the frame. The silks remain pliable even at cryogenic temperatures and are robust against the high-radiation dose absorbed during the DT permeation fill. The cover photograph shows a time-integrated optical image of a DT cryogenic capsule being irradiated by the OMEGA laser. The uncoverted 2ω light scatters off the silks and the beryllium C mount. Individual beam spots can be seen on the capsule itself. Data from this implosion is discussed in the article "Cryogenic DT and D_2 Targets for Inertial Confinement Fusion" on page 167.
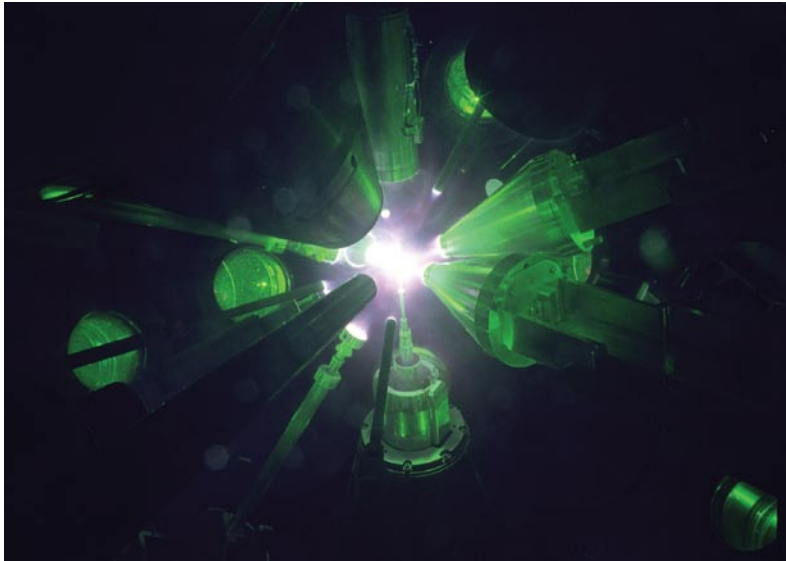
A wide-field view of the cover photograph shows the large number of target-physics diagnostics used to understand the cryogenic implosions. These include two x-ray spectrometers (on the right), charged-particle spectrometers, x-ray pinhole cameras, and a gated x-ray imager. The structure below the target is the moving cryostat docked to the lower pylon; the upper shroud is directly above the target. The upper shroud is quickly removed just prior to laser irradiation. The capsule is exposed to the chamber for less than 100 ms before the shot. This ensures that the ice layer is unaffected by the ambient chamber infrared radiation. If the exposure time is much longer than 100 ms, the chamber radiation will begin to melt the ice layer.

For questions or comments, contact Jake Bromage, Editor, Laboratory for Laser Energetics, 250 East River Road, Rochester, NY 14623-1299, (585) 273-5105.

Worldwide-Web Home Page: http://www.lle.rochester.edu/

LLE Review

Quarterly Report

UR
LLE

Contents

In Brief

This volume of the LLE Review, covering July–September 2006, features "Cryogenic DT and D_2 Targets for Inertial Confinement Fusion" by T. C. Sangster. In this article (p. 167), the author reports on the development of cryogenic targets since the need was first recognized more than 30 years ago. Virtually all ignition target designs for the National Ignition Facility (NIF) are based on a spherical low-*Z* ablator containing a solid, cryogenic-fuel layer of deuterium and tritium. Techniques developed at LLE can produce targets with an inner ice surface that meets the surface-smoothness requirement for ignition (<1-μm rms in all modes). Significant progress with the characterization of such targets is also reviewed along with results from the most-recent cryogenic implosions that simulations suggest have yielded values for ρR_{peak} as high as 190 ± 20 mg/cm^2.

Additional highlights of recent research presented in this issue include the following:

- R. F. Orsagh, J. Ulreich, L. Lund, M. Bonino, D. Turner, and D. Jacobs-Perkins present results from a study of the displacement of cryogenic targets from target chamber center (TCC) (p. 179). While beam smoothing and power balancing can ensure highly uniform illumination at TCC, target displacements of 5 μm or more from TCC can unbalance the illumination enough to initiate hydrodynamic instability. Correlation between target vibration at TCC and the response characteristics obtained in their study indicate that the modes of the spider silk are the primary cause of displacement.

- C. K. Li, F. H. Séguin, J. A. Frenje, R. Rygg, and R. D. Petrasso (Plasma Science and Fusion Center, MIT); R. P. J. Town, P. A. Amendt, S. P. Hatchett, O. L. Landen, A. J. Mackinnon, and P. K. Patel (LLNL); and V. A. Smalyuk, T. C. Sangster, and J. P. Knauer (LLE) present a novel imaging technology for measuring *E* and *B* fields in laser-produced plasmas using monoenergetic proton radiography (p. 189). The generation of electromagnetic fields by the interaction of laser light with matter is a process of fundamental interest in high-energy-density physics. They present high-resolution, time-gated radiography images of a plastic foil driven by a 10^{14}-W/cm^2 laser that imply *B* fields of 0.5 MG and *E* fields of 1.5×10^8 V/m. Furthermore, their measurements demonstrate the beneficial focal smoothing effects produced by distributed phase plates for substantially reducing medium-scale chaotic field structure.

- B. Ashe, K. L. Marshall, C. Giacofei, A. L. Rigatti, T. J. Kessler, A. W. Schmid, J. B. Oliver, J. Keck, and A. Kozlov present an evaluation of cleaning methods for multilayer-dielectric (MLD) diffraction gratings (p. 194). MLD diffraction gratings are essential components for the OMEGA EP short-pulse, high-energy laser system, and as such they must have both high optical-diffraction efficiency and high laser-damage threshold. The authors report on a study of chemical processes for cleaning MLD gratings that identifies techniques for removing contaminants left during fabrication in a way that does not compromise a grating's efficiency or damage threshold.

- C. Dorrer and J. D. Zuegel describe the design and analysis of binary beam shapers for high-power laser systems (p. 202). OMEGA EP uses square beams with high-order super-Gaussian profiles to maximize the fill factor of amplifiers without exceeding the damage fluence of the laser components. The spatially dependent gain of the amplifiers can be, to a large extent, precompensated by attenuating

regions of the input beam according to the gain they receive in the amplifiers. The authors have applied an error diffusion algorithm to the design of binary beam shapers consisting of a nonuniform array of 10-μm-sq pixels, which can be produced using standard lithographic techniques on high-damage-threshold, metal-on-glass substrates. Simulations show that this technique can produce beam shapers with the correct profile to precompensate the spatially dependent gain of OMEGA EP's amplifiers with low rms error.

- This volume concludes with a summary of LLE's Summer High School Research Program (p. 211), the FY06 Laser Facility Report (p. 213), and the National Laser Users' Facility and External Users' Programs (p. 215).

Jake Bromage
Editor

Cryogenic DT and D$_2$ Targets for Inertial Confinement Fusion

Introduction

Laboratory-based ignition via inertial confinement fusion (ICF)[1] will be achieved by imploding a spherical capsule containing a frozen layer of deuterium and tritium (DT) fuel on the MJ-class National Ignition Facility (NIF)[2] currently under construction at Lawrence Livermore National Laboratory (see Fig. 108.1). Virtually all ICF ignition target designs are based on a spherical low-Z ablator containing a solid, cryogenic DT-fuel shell surrounding a low-density DT vapor at, or slightly below, the triple point. There are two fundamental target designs for ignition: capsules directly illuminated by the laser (direct drive[3]) and capsules driven by a uniform x-ray radiation field created by illuminating the inside surface of a high-Z cylindrical hohlraum (indirect drive[4]). Figure 108.2 illustrates the drive concept and capsule design for both direct- and x-ray-drive ignition targets. X-ray-drive ignition capsules[5] are based on a thick, copper-doped Be ablator surrounding a relatively thin DT-ice layer; capsules for direct-drive ignition[3]

consist of a very thin plastic shell surrounding a relatively thick DT-ice layer. When these capsules are illuminated by either the laser or the x-ray field inside a hohlraum, the ablator material is rapidly heated and driven away from the capsule. The resulting shock compresses the DT-fuel shell, raising the pressure in the central gas region (or core) to several Mbar. Once the laser irradiation ceases, the fuel shell begins to decelerate, further compressing and heating the core as the shell's kinetic energy is converted to thermal energy via PdV work. To initiate a thermonuclear burn, the temperature and areal density of the core must reach approximately 10 keV and 300 to 400 mg/cm^2, respectively.[4] Under these conditions, the rate of energy deposited in the fuel by the 3.5-MeV ^{4}He nuclei from the DT–fusion reaction is greater than the energy lost by electron conduction or x-ray emission, and a thermonuclear burn wave propagates through the dense fuel shell in a few tens of picoseconds. This is much shorter that the fuel-disassembly time of a few hundred picoseconds.

1.8 MJ

Under construction at LLNL

OMEGA LLE

240 feet

TC4680jRC
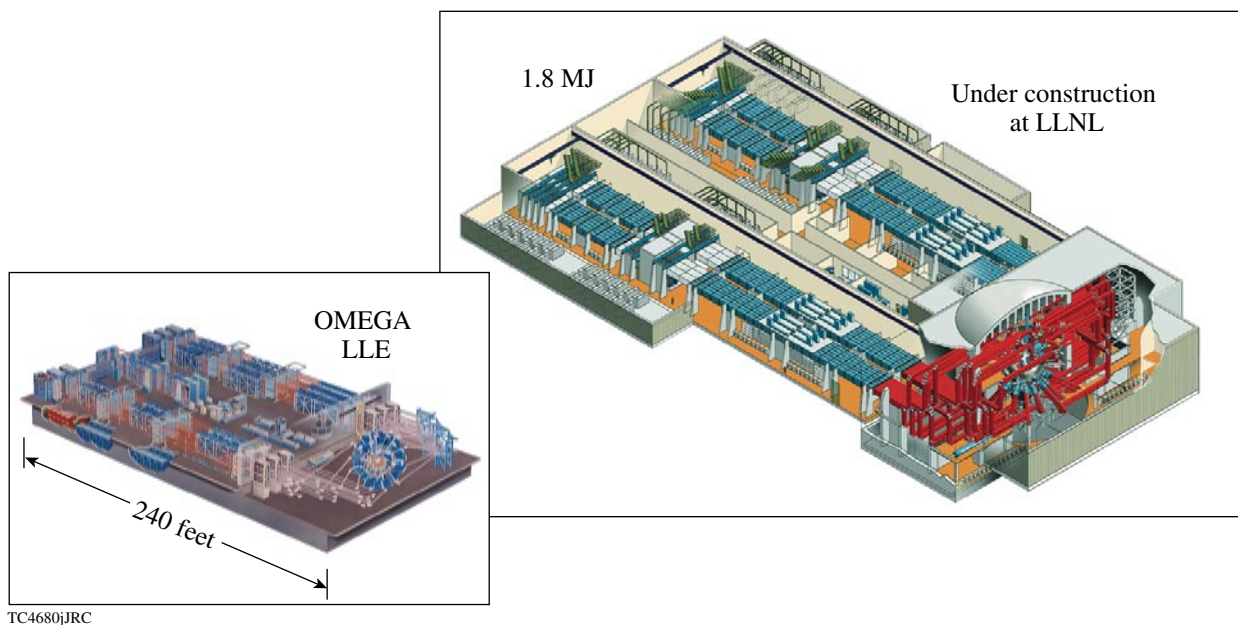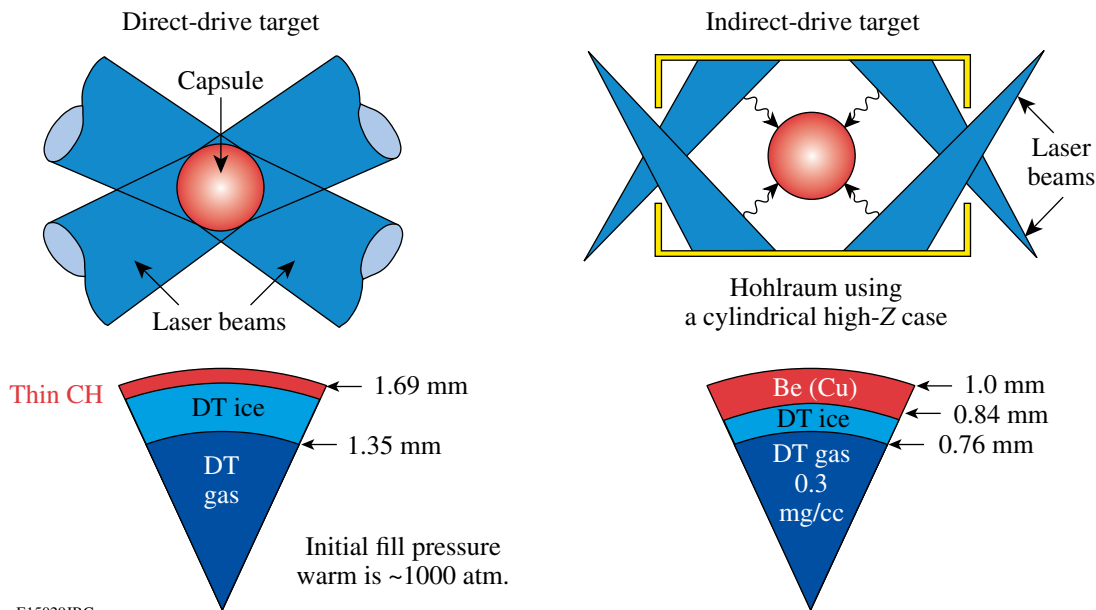
Figure 108.1

The National Ignition Facility (NIF) is under construction at Lawrence Livermore National Laboratory and will begin ignition experiments with cryogenic DT targets in 2010. LLE's OMEGA laser is being used to develop the scientific and technical basis for ignition on the NIF. OMEGA performs 40 to 50 cryogenic D$_2$ and DT implosions annually in support of the ignition mission.

Figure 108.2
The basic ignition-target designs are shown along with the fundamental concepts for direct and indirect (or x-ray) drive.

For nearly two decades, LLE has been developing the scientific and engineering basis to create and characterize cryogenic DT capsules and to study the implosion performance under scaled-ignition conditions. Cryogenic fuel shells are the preferred configuration for ICF because the fuel can be compressed isentropically, minimizing the laser energy required to achieve ignition conditions.[6] Since beginning cryogenic target implosions on the 60-beam, 30-kJ UV OMEGA laser[7] (see Fig. 108.1), 118 cryogenic D_2 (Refs. 8–11) and 15 cryogenic DT capsules have been imploded. While the compressed-fuel densities and core temperatures of these cryogenic DT implosions will never meet the criteria for ignition, measured fuel areal densities (the product of the fuel density and the radial extent of the fuel) have been inferred in excess of 100 mg/cm^2. This is an important step toward the demonstration of energy gain via ICF and ultimately the realization of inertial fusion energy.[12]

The uniformity of the inner surface of the DT-ice layer is one of the critical factors that determine target performance.[3,4] As the high-density fuel shell decelerates and compresses, inner-surface perturbations grow due to the Rayleigh–Taylor instability.[13] These perturbations include ablation-front features that feed through the fuel shell[14] and native inner-ice-surface roughness from the layering process described in **Cryogenic D_2 and DT Target Fabrication and Characterization** (p. 170). The ablation-front perturbations are generated primarily by laser non-uniformities and the feedout of inner-ice-surface perturbations carried by the reflected shock. These ablation-front perturbations

can be controlled by conditioning the laser pulse[15] or by careful design of the hohlraum used to create a homogenous radiation field around the capsule for indirect drive.[16] If the initial amplitude of the inner-surface perturbations is too large, the hot core is disrupted and the conditions for ignition and burn do not occur. This leads to an ignition requirement that the inner-surface ice roughness be less than 1-μm rms in all modes.[3,4]

The OMEGA laser is the only facility in the world routinely imploding cryogenic D_2 and DT targets. The target-handling concepts on OMEGA are based on work that began nearly 30 years ago. The next section will review some of the historical accomplishments that had a direct impact on the design of the OMEGA system. One of the fundamental breakthroughs for ignition was the realization of β-layering in 1986. The next section will also describe the β-layering process. Later sections will (1) discuss the development of optical and x-ray-characterization techniques to assess the quality of the DT layers produced by β-layering; (2) describe the systems used to implode these targets on the OMEGA and NIF lasers; and (3) present the results of the first cryogenic DT implosions on OMEGA.

Historical Perspective
Following the concept declassification, J. H. Nuckolls *et al*. first discussed the concept of laser fusion in 1972.[1] Powerful lasers would be used to implode a shell or sphere of solid DT reaching breakeven at relatively modest laser energies (at least by today's standards). While the physical assumptions in this

and other early work turned out to be overly optimistic with respect to the required laser energy, the basic target design—a shell of solid DT—has remained unchanged. After this seminal publication appeared, work began on the development of target concepts for creating thin cryogenic-DT layers (both solid and liquid). The early work (throughout much of the 1970s and 1980s) focused on thin glass shells filled with high-pressure DT gas. Typical scales were 100-μm-diam shells with up to 100 atm of DT gas. When cooled using thermal conduction, the DT layers were typically less than 10 μm thick.

In 1977, Henderson and Johnson at KMS Fusion[17] reported the first irradiation of a cryogenic DT capsule with a laser. The target was a 60-μm-diam, thin-walled glass shell filled with 10 atm of DT (60:40). The capsule was cooled via point-contact conduction and was exposed to ambient chamber infrared (IR) radiation (the point-contact cooling overwhelmed the IR heating from the chamber). These capsules were illuminated with a laser power of approximately 0.2 TW and produced a neutron yield between 10^6 and 10^7, an order of magnitude higher than the same capsules illuminated at room temperature. This demonstrated the advantage of using the high-density cryogenic-fuel layer for ICF. At about the same time, Miller[18] described a new method for producing cryogenic-fuel layers based on what came to be known as the fast-refreeze technique. This technique produced layers with a considerably more uniform thickness than point conduction. The fast-refreeze technique relies on a static heat-exchange gas (He) for rapid cooling of the capsule. Once frozen, the ice in the capsule is melted using a laser beam. The vapor then condenses uniformly on the inside of the glass shell and refreezes before gravity can induce the liquid to flow. This technique quickly became the standard for cryogenic target development well into the 1980s.

In 1978, Musinski *et al.*[19] adapted the fast-refreeze technique for the targets being imploded at KMS Fusion. To eliminate the He exchange gas prior to laser illumination and to minimize the exposure of the cold capsule to ambient IR radiation in the target chamber, they introduced the principle of a cryogenic retractable shroud. Here, the exchange gas is limited to a small volume around the capsule inside the shroud. Their calculations suggested that the exposure time had to be less than 10 ms once the shroud was removed or the thin DT-ice layer would melt due to ambient chamber IR radiation. Thus, within only a few years, three of the key concepts underpinning the success of the OMEGA Cryogenic Target Handling System had been developed: (1) redistribution of the ice using external radiation, (2) thermal control of the capsule isotherm via a cold exchange gas, and (3) a fast retractable shroud to minimize the

target exposure to ambient chamber radiation. These concepts were employed on the 24-beam OMEGA laser[20] in 1987 and 1988 to implode over 100 cryogenic-DT-filled, fast-refreeze glass capsules leading to compressed DT densities of 100 to 200 times liquid density.[21]

By the late 1980s, it was realized that the fast-refreeze technique could not be used to create thick, uniform DT-fuel layers. Thicker DT layers were required for the advanced targets being designed for the proposed upgrade of the OMEGA laser to 60 beams and 30-kJ UV. Fundamentally, the thin glass shell exploding pusher targets originally envisioned for ignition and gain did not work. The demonstration of β-layering in 1988 by Hoffer and Foreman[22] revolutionized the development of targets for ICF and fusion ignition. The "β-heating" concept to produce highly uniform DT-ice layers inside capsules had been suggested by Martin as early as 1985 (Ref. 23) and published formally in 1988 (Ref. 24). The concept is deceptively simple. The radioactive decay of the tritium produces an electron with an average energy of about 6 keV. At 6 keV, the electron range in solid DT is only 1 to 2 μm, so the energy is deposited locally and, consequently, the bulk of the ice is heated uniformly. With a spherically symmetric isotherm on the capsule surface, the radial temperature gradient induced by the β-heating causes DT to sublimate from the slightly thicker and, consequently, slightly warmer regions inside the capsule and deposit on the slightly cooler, thinner regions (see Fig. 108.3). If the capsule surface is kept just below the triple point, the ice will ultimately relax to a uniform radial thickness.

E15072JRC
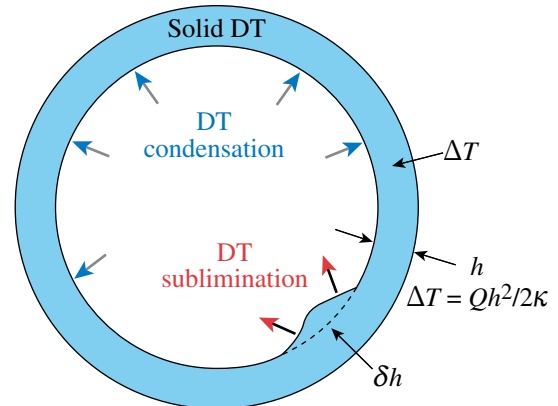
Figure 108.3
Schematic showing the basic concept behind β-layering in a cryogenic DT shell. If the outside of the shell is maintained at a temperature slightly below the DT triple point, a temperature gradient develops across the ice due to the radioactive decay of the tritium; the emitted electron (average energy of 6 keV) deposits energy, locally heating the bulk of the ice. Consequently, radially thicker (warmer) regions sublimate inside the shell and condense on radially thinner (cooler) locations, eventually relaxing to a uniformly thick shell.

In 1996, Collins et al.[25] showed that IR radiation could be used to excite the vibration–rotation band in solid D_2 (or HD), leading to a redistribution or smoothing similar to that induced by β-layering in DT. The process is virtually identical to β-layering as the IR heats the bulk of the ice. With symmetric IR illumination and adequate power, the layer uniformity in D_2 should be as good as in DT.[26] In this way, cryogenic D_2 capsules can be used as ignition surrogates without the radiological impacts associated with DT (e.g., tritium contamination, neutron activation, neutron-induced radiation effects in diagnostics, etc.). Indeed, as mentioned in the **Introduction** (p. 167), the initial ignition-scaled cryogenic capsule implosions on OMEGA were based on D_2 fuel; DT was introduced only recently following extensive operational experience and a thorough systems readiness review.

Cryogenic D_2 and DT Target Fabrication and Characterization

Physically mounting a capsule to be imploded by a multi-beam laser system presents a great challenge for both direct- and x-ray-drive illumination. Mounting the capsule can have a profound effect on the resulting layer quality due to the thermal perturbations caused by the structures around the capsule. Target performance requires a high degree of irradiation uniformity (i.e., the capsule surface cannot be shadowed) and minimal mass perturbations on the surface of the capsule (some mechanical structure must physically attach to the capsule).

To meet these criteria for a direct-drive capsule, LLE implemented a concept based on spider silks[27] [see Fig. 108.4(a)]. Here the capsule is mounted at the center of a "C"-style frame using four strands of spider silk (the silk diameter is typically less than 1 μm). The strands are either glued directly to the surface of the capsule or the entire assembly is overcoated with a thin layer (typically 0.2 μm) of parylene to bond the silks to the capsule. The diameter of the cryogenic targets imploded on the OMEGA laser is set by scaling the ignition target design for the NIF to the energy available;[3] this leads to a capsule diameter of 860 μm for implosions on the OMEGA laser.

For OMEGA, these thin CH shells are permeation filled with an equimolar mixture of DT to 1000 atm. At pressure, the shell and gas are slowly cooled to a few degrees below the DT triple point (19.8 K), while the pressure differential across the shell is maintained below 1 atm to avoid buckling. This is the most critical step in the filling process. Once the DT gas solidifies, the capsule is transferred to a moving cryostat;[8,9] this cryostat is used to maintain the appropriate thermal environment around the capsule until it is imploded. Inside the moving cryostat, the capsule is kept at the center of a gold-coated copper layering
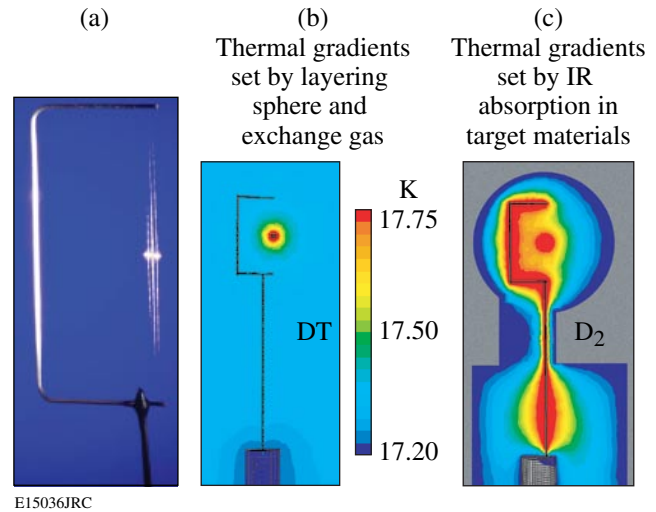

Figure 108.4
(a) To create a cryogenic target, an 860-μm-diam CH shell is initially mounted to a beryllium "C"-style frame using four strands of spider silk. (b) Thermal modeling shows that isotherm at the surface of a cryogenic DT-filled capsule is highly uniform. (c) However, the IR radiation used to layer D_2 ice also heats the beryllium "C"-mount and the spider silks, causing a significant distortion in the isotherm at the surface of the capsule. This can lead to a significant asymmetry in the ice thickness for cryogenic D_2 targets.

sphere with two orthogonal viewing ports for alignment and ice-surface characterization (discussed below). A thermal model of this system [see Figs. 108.4(b) and 108.4(c)] shows that the isotherm at the surface of a DT capsule is spherical and that none of the target-support structures or layering-sphere asymmetries (e.g., sapphire windows for viewing the target) influence the isotherm [Fig. 108.4(b)]. By controlling the pressure of the exchange gas and the temperature of the copper layering sphere, a spherical isotherm at the DT triple point can be maintained at the ice surface inside the capsule and β-layering produces high-quality layers within a matter of hours.

With IR illumination, the thermal model indicates that there can be significant geometrical distortions in the capsule surface isotherm [Fig. 108.4(c)]. These distortions are caused by IR radiation absorbed on the target support structures (the Be C-mount and the silk).[26] For example, the D_2 ice facing the Be C-mount is typically thinner since the Be frame is warmer than the He exchange gas. This modeling suggested three changes that significantly improved the D_2-ice-layer quality: (1) the pressure of the exchange gas was increased to further homogenize the thermal perturbations, (2) the target structures were plated with gold to reduce the IR absorption, and (3) a diffuser was added to the IR heating port to more uniformly distribute the radiation in the layering sphere (which acts as an integrating sphere for
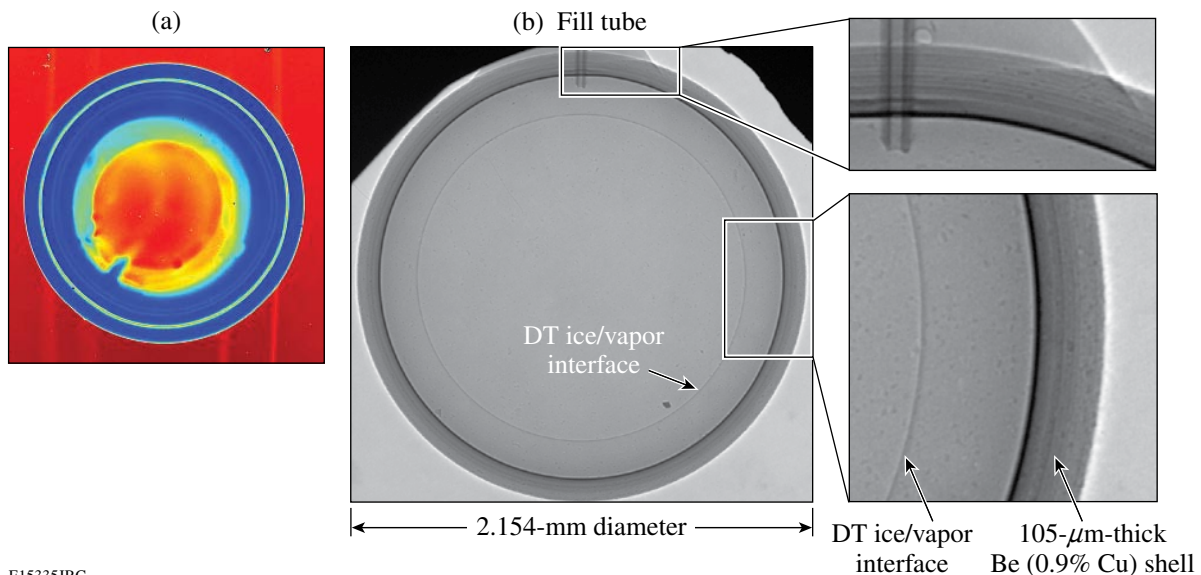
the IR). With these improvements, the average ice-layer quality in D$_2$ capsules improved by a factor of 2.

For x-ray drive on the NIF, Be capsules are mounted at the center of a cylindrical high-Z hohlraum using a "tenting" scheme.[5] The thermal environment around the capsule is established by the hohlraum geometry. Azimuthally symmetric heaters are placed along the hohlraum axis to produce a more spherically symmetric isotherm at the capsule surface.[28] The Be shells are filled in generally less than 30 min using a narrow fill tube connected to a DT reservoir. Simulations suggest that the fill-tube perturbation will not significantly affect implosion performance.[29] The β-layering process inside the hohlraum has been rigorously tested in the laboratory and will be incorporated into the Load, Layer, and Characterization System (LLCS) under development for the NIF Cryogenic Target System (NCTS). Once a uniform layer is achieved, the temperature of the ice is cooled further to reduce the DT vapor density in the central void region. At 1.5 K below the triple point, the vapor density is 0.3 mg/cc; this is the x-ray-drive-ignition requirement. Cooling the capsule below the triple point is not a requirement for the baseline direct-drive-ignition design.

Apart from the need to monitor the ice layers during formation, simulation codes require inner-ice-surface characterization information to properly predict target performance; therefore, it is important to image the liquid/ice-layer surface with high resolution. For transparent ablators (e.g., CH or CD shells), the location of the inner ice surface is measured using optical shadowgraphy.[30] The capsule is backlit using an optical plane wave (typically a pulsed source with a duration of less than 1 ms to minimize any motional blurring; the energy absorbed by the capsule is negligible). The light is totally internally reflected off the inner surface of the ice, creating a bright ring in the image plane that represents the location of the inner surface relative to the center of the capsule. This bright ring can be seen in Fig. 108.5(a)—a shadowgraph of the first DT capsule to achieve an inner-ice-surface smoothness of 1-μm rms. The resolution of the shadowgraph is less than 0.1 μm. The ring represents an azimuthal measure of the radial variation of the ice along a slice through the center of the capsule normal to the optical viewing axis. This ring is "unwrapped" azimuthally around the center of the capsule to form a line in radius-azimuth space. A power spectrum of the ice roughness as a function of the mode number is generated by fitting the Fourier amplitudes of the radial variation as a function of the azimuth.[31]

For opaque ablators (e.g., Be or low-density foams), x-ray phase-contrast imaging is used to determine the location of the inner ice surface.[32] Phase-contrast imaging relies on spatial gradients in the real part of the refractive index to produce image contrast. These gradients occur at the Be/ice and ice/vapor (the

(a)   (b) Fill tube

DT ice/vapor interface

2.154-mm diameter

DT ice/vapor interface   105-μm-thick Be (0.9% Cu) shell

E15335JRC

Figure 108.5
(a) A typical optical shadowgraph of a cryogenic DT layer. The bright band is a measure of the radial variation of the inner ice surface for a slice through the center of the target. (b) A typical x-ray phase-contrast image of a beryllium shell containing a DT-ice layer. The phase-contrast image provides structural detail within the shell and the ice. The inner band represents a measure of the radial variation of the inner ice surface along a slice through the center of the capsule.

central void region) interfaces of a layered target, causing local curvature in the transmitted wave that leads to interference and a modulation in the x-ray intensity. Even for a virtually transparent medium (e.g., the region around the interface of the ice and DT vapor), phase gradients modulate the intensity of an x-ray wave and can be used to determine the precise location of the ice surface along a slice through the capsule normal to the x-ray-propagation axis. Figure 108.5(b) shows an example of an x-ray phase-contrast image. The capsule is a 105-μm-thick Be shell containing an ~180-μm-thick DT-ice layer. The ice/vapor interface is unwrapped in radius-azimuth space, and a power spectrum as a function of the mode number is generated as described above.

Because of the inherent symmetry of the direct-drive layering sphere, it is possible to rotate a direct-drive capsule with respect to the viewing axes in the characterization station. By rotating the capsule, any number of independent shadowgraphs can be obtained and used to create a 3-D representation of the inner ice surface. Such a representation (based on 48 independent shadowgraphs) is shown in Fig. 108.6 for two different DT-ice layers. Since the viewing axes are not orthogonal to the rotation axis, the poles of the capsules cannot be characterized. The contours represent surface deviations in microns relative to a perfect sphere at the average ice-surface radius. The peak-to-valley surface variation for both capsules is ~2 μm out of a total ice thickness of ~95 μm. Full $Y_{\ell m}$ Legendre amplitudes can be fit to this surface for modes up to 12 (the limiting factor is the missing data at the poles), and the procedure described by Hatchett and Pollaine[33] is used to estimate the 2-D equivalent of the Legendre modes for $\ell > 12$. The ignition specification is typically quoted as a power spectrum for modes from 1 to 1000, although in practice the resolution of the measurement limits meaningful power to modes less than 100 or so.[34] For direct drive, this specification is 1.0-μm rms in all modes and ≤ 0.25-μm rms in modes greater than 10. Both of the targets shown in Fig. 108.6 meet the inner-ice-surface smoothness requirement for direct-drive ignition on the NIF. Figure 108.7 compares the power-spectrum decomposition of the ice-surface roughness for six targets imploded consecutively on the OMEGA laser and the ignition specification (heavy solid line). For the best capsule, the measured power spectrum is 0.72-μm rms in all modes and 0.24-μm rms above mode 10, comfortably exceeding the ignition requirement.

Layering and characterization of a DT-fuel layer in a hohlraum for x-ray-drive ignition present significant challenges. For capsules in a hohlraum, the presence of the fill tube can create a thermal asymmetry leading to a low-mode variation in the ice thickness around the fill tube (generally thicker ice since the fill
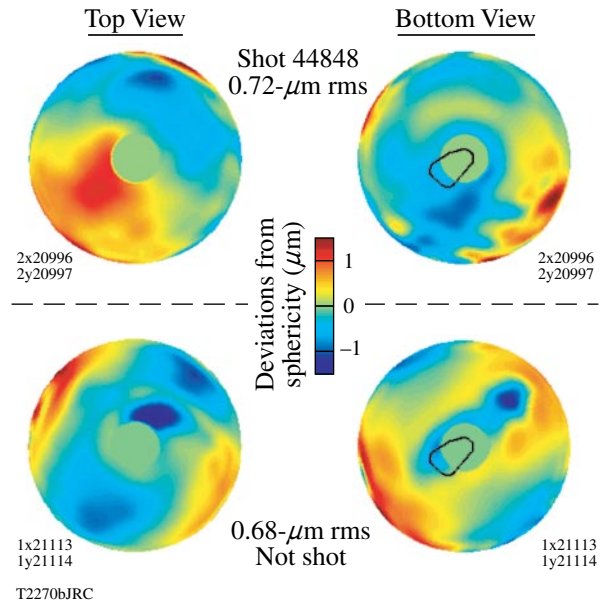
Figure 108.6
A 3-D representation of the inner ice surface can be created by fitting to a large number of independent shadowgraphs. Top and bottom views are shown for two different capsules that meet the direct-drive-ignition requirement for the inner ice smoothness. The contour mapping represents deviations of the inner ice surface from a sphere at the average radius. Because the viewing axes are not orthogonal to the rotation axis, there is no data at the poles.

Figure 108.7
The power per mode for six DT cryogenic targets as a function of mode number. These targets were shot consecutively over a period of several weeks on OMEGA. The direct-drive-ignition specification for the inner ice smoothness is shown as the heavy solid line.

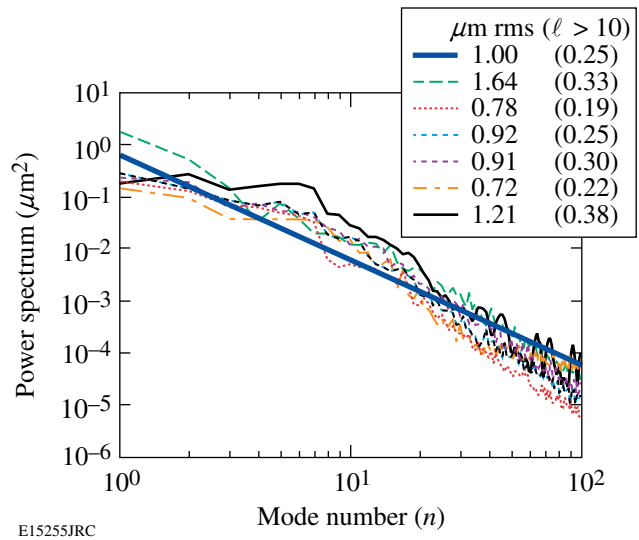tube is colder). Furthermore, as the ice as cooled below the triple point, mid- and high-mode roughness begins to appear as the ice contracts and the β-layering process begins to shut down. However, by cooling very slowly from the triple point to 18.3 K (the ignition requirement), the ice roughness remains at the ignition specification for modes 10 and above. The behavior of the ice roughness in modes 10 to 128 as a function of ice temperature is shown in Fig. 108.8.
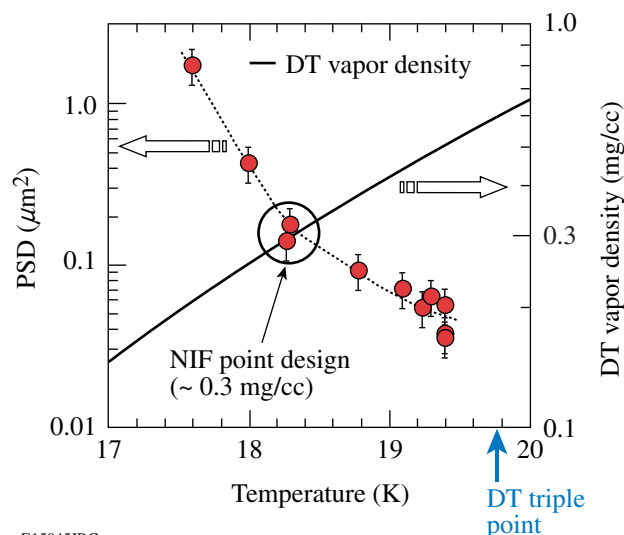

E15045JRC

Figure 108.8
The power-spectral density for a prototype x-ray-drive cryogenic DT target as a function of the ice temperature. The power spectral distribution (PSD) is summed for modes 10 to 128. The ice-temperature requirement for x-ray-drive ignition is 18.3 K. This target meets the ignition requirement over this mode range at the required ice temperature.

Imploding Cryogenic Targets on OMEGA and the NIF

The original Cryogenic Target Handling System (CTHS) on the 24-beam OMEGA laser[20] incorporated the concepts discussed in **Historical Perspective** (p. 168). These concepts included an opposed-port shroud-retraction scheme using a linear induction motor and He gas cooling to support the fast-refreeze layering process. A shearing interferometer was implemented for layer characterization (thickness and uniformity). The thermally passive shroud and the actively cooled target stalk are shown in Fig. 108.9. The inset picture in Fig. 108.9 shows the "horseshoe" target assembly with a 300-μm-diam glass shell mounted using several strands of spider silk (rather than using glue to bond the silk to the capsule, the capsule and silk were overcoated with 0.2 μm of parylene following assembly). During the late 1980s, this system imploded over 100 glass-shell targets with 5-μm-thick DT layers, achieving 200 times liquid density in the DT.[21]
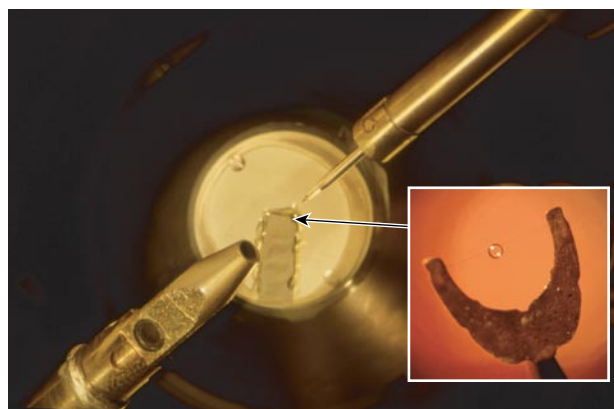
E15336JRC

Figure 108.9
The shroud and target inserter from the 24-beam OMEGA Cryogenic Target Handling System are shown. The thermally passive removable shroud is the structure at the lower left. The inset shows a picture of the "horseshoe"-style mount for the capsule. Strands of spider silk are used to mount the capsule between the tips of the mount.

By the early 1990s, target designs were being developed for ignition that required considerably thicker DT layers with very high layer uniformity.[35] The fast-refreeze technique and thin glass shells were no longer adequate. New concepts were developed by General Atomics and LLE to support scaled-ignition target implosions on the new 60-beam OMEGA laser (completed in 1996). The new requirements for the CTHS included (1) a separate high-pressure-permeation fuel-filling system that was both D_2 and DT capable, (2) variable ice-layer thickness up to 100 μm in mm-diameter-scale, thin-walled CH capsules, (3) the capability to fill up to 12 targets per week, (4) IR-enhanced layering for D_2 and β-layering for DT fuel, (5) an independent layer-characterization station based on optical shadowgraphy, (6) a moving cryostat to deliver the target from the tritium facility to the target chamber, (7) target-alignment accuracy relative to the target chamber center (TCC) of 5 μm, (8) an opposed-port shroud-retraction scheme with a target exposure time of less than 100 ms before laser irradiation, and (9) a vertical shroud pull.

The operation of the CTHS on OMEGA has been well documented.[8–11] Since 2001, 118 cryogenic D_2 and 15 cryogenic DT capsules have been imploded. The key to the success of the OMEGA CTHS is the moving-cryostat concept. A photograph of the moving cryostat is shown in Fig. 108.10 with and without the thermally passive upper shroud. The moving cryostat includes a local He-gas cryogenic cooler on the thermally controlled lower shroud, a four-axis position controller (X, Y, Z, and θ) for the target stalk, a rigid docking interface to the target chamber, He exchange-gas regulation, and a thermally passive upper shroud with sapphire windows aligned to the OMEGA Target

Viewing System. With the moving-cryostat concept, critical target functions are performed away from the target chamber (i.e., permeation filling, layering, and characterization). Consequently, there is little or no impact on the utilization of the laser system when imploding cryogenic targets. An overview of the target handling process is shown in Fig. 108.11. The targets are permeation filled in a separate cryostat over a period of approximately four days and then transferred to the moving cryostat. The moving cryostat is then mated to the Characterization Station (still within the tritium facility). Once the appropriate layer is achieved (this typically requires 1 to 2 days for D$_2$ and less than 1 day for DT), the moving cryostat is taken to the bay beneath the OMEGA target chamber (a distance of about 200 ft). The moving cryostat is aligned with the lower pylon and then raised 22 ft through a vacuum interface to the center of the target chamber. Target alignment is performed using an automated centering routine to predetermined coordinates that account for static alignment offsets due to the sapphire windows. At shot time, a linear induction motor (LIM) removes the upper shroud using a precise acceleration/deceleration trajectory. The trajectory minimizes mechanical coupling between the LIM motion and the target. The target is exposed to the ambient chamber radiation for 90 ms prior to laser irradiation.

The conceptual basis for the NIF Cryogenic Target System (NCTS)[28,36] is significantly different from the OMEGA CTHS. The Load, Layer, and Characterization System (LLCS) is being developed to operate just outside the NIF target chamber but mechanically integrated with the target inserter and target chamber. Using the LLCS, DT will be loaded at about 50 psi into a 1-cc reservoir at the target base. This reservoir is connected to the Be capsule via a narrow (of the order of 10-μm OD) fill tube. The entire assembly is cooled to within a few degrees of the DT triple point (19.8 K). The reservoir is then heated to between 50 and 70 K, causing the DT to condense inside the Be shell. X-ray phase-contrast imaging will be used to monitor the DT meniscus (and consequently the amount of fuel in the shell) during the fill. Once the required amount of fuel is in the shell, the layering and characterization process proceeds as described in **Cryogenic D$_2$ and DT Target Fabrication and Characterization** (p. 170). Following the final characterization, the target is moved to the center of the NIF target chamber and aligned with the 192 laser beams. The target is protected from condensation and room-temperature IR radiation from the chamber by a clam-shell shroud (see Fig. 108.12). Several seconds before the shot, the shroud is opened. Heaters on the hohlraum compensate for the sudden IR illumination and maintain a constant hohlraum temperature. Any target vibration induced by the shroud opening damps during the 1 to 2 s prior to laser illumination.

Cryogenic DT Target Performance

All of the DT (and a few of the recent D$_2$) capsules imploded to date on OMEGA have been driven with a laser pulse designed to keep the fuel on an adiabat α of approximately 1 to 3, where α is the ratio of the internal pressure to the Fermi-degenerate pressure.[3]
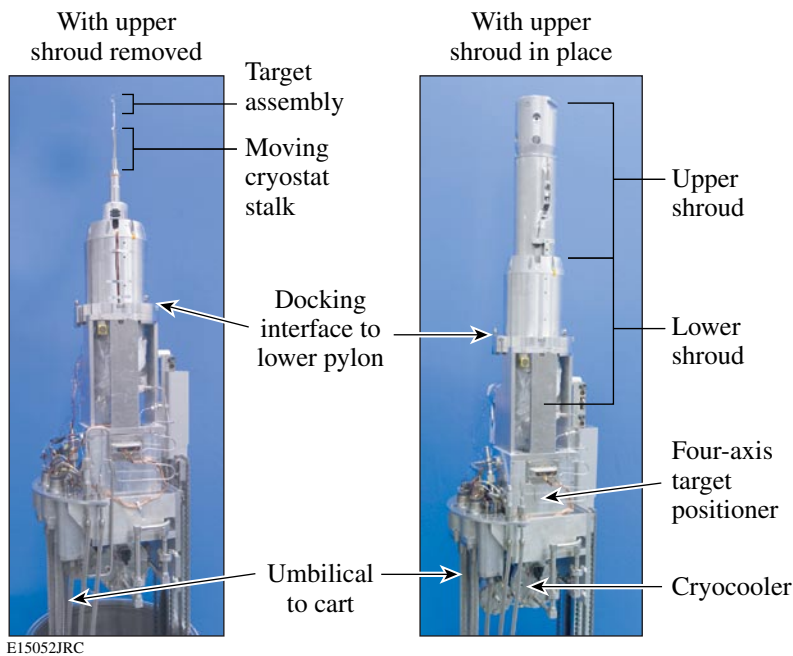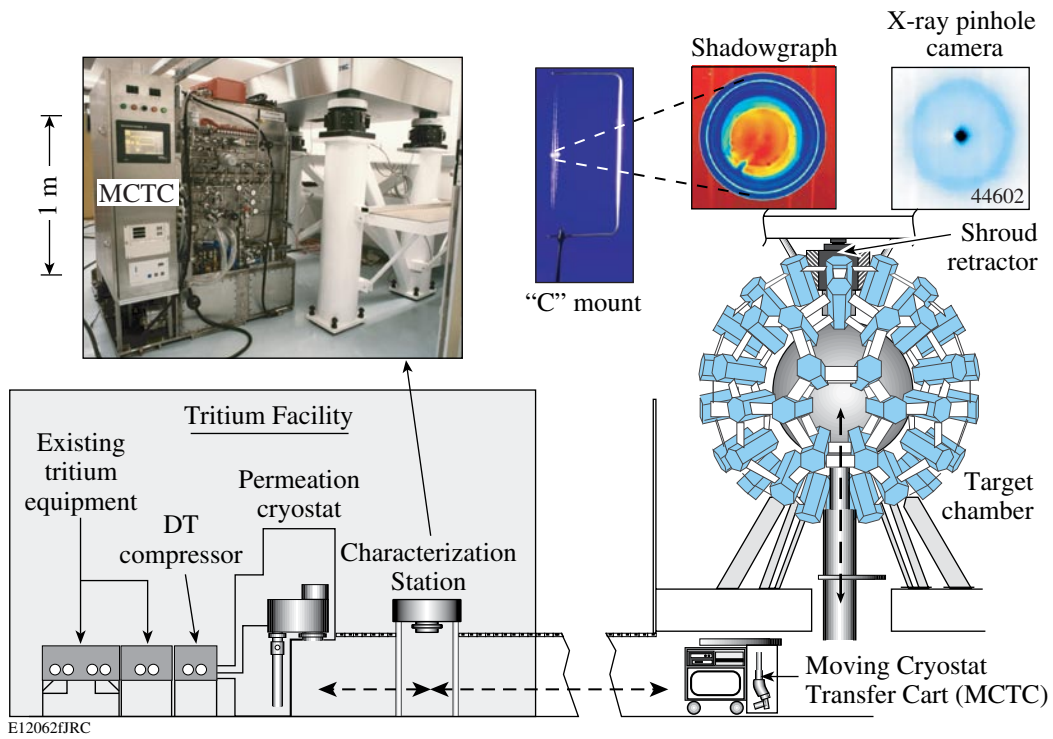

E15052JRC

Figure 108.10
The 60-beam OMEGA moving cryostat with (right) and without (left) the upper shroud. The moving cryostat is the heart of the OMEGA Cryogenic Target Handling System. The upper shroud is removed to expose the capsule at shot time. The capsule exposure time is approximately 90 ms.

Figure 108.11

Target-handling operations are conducted away from the target chamber to increase the utilization of the laser facility. This includes the filling, layering, and characterization steps that are done within the LLE tritium facility. Once a target is ready to implode, the Moving Cryostat Transfer Cart (MCTC) is positioned below the chamber and the moving cryostat with the target is raised 22 ft to dock with the support structures on the target chamber. The entire shot sequence can be repeated approximately every 2 h.
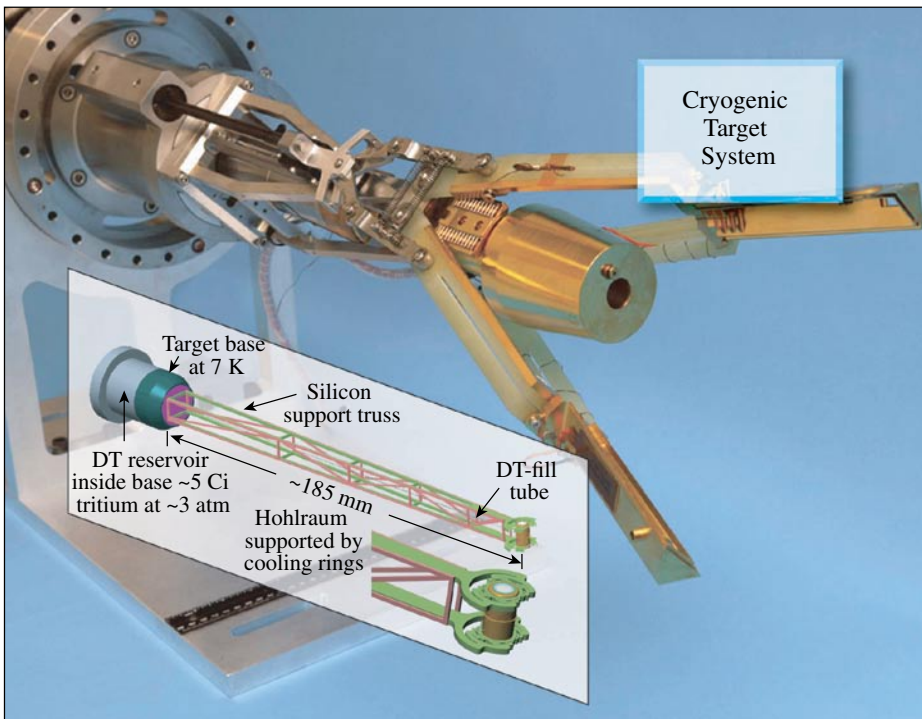
Figure 108.12

An x-ray-drive target on the NIF will be protected from the ambient chamber radiation using a clam-shell-style retractor. The clam-shell retractor can be opened slowly to avoid inducing excessive vibration because the target can withstand several seconds of chamber exposure before significant temperature perturbations develop on the capsule surface. The hohlraum/reservoir schematic shown in the inset fits on the end of the cold head in the middle of the figure.

These drive pulses scale to ignition, and consequently the areal densities during the fusion burn are expected (based on a 1-D radiation hydrocode simulation[36]) to be in excess of 200 mg/cm² (this corresponds to ~300× liquid density for the DT) and to approach 250 mg/cm² at peak density. The areal density monotonically increases during the fusion burn, and the neutron- or burn-averaged areal density $\langle \rho R \rangle_n$ will be less than the peak areal density ρR_{peak}. The fusion burn truncates prior to peak density (or compression) due to the thermal quenching caused by mixing of colder fuel with the hot spot.[37] Charged-particle diagnostics[38] are used to infer $\langle \rho R \rangle_n$ from D_2 implosions, while x-ray diagnostics[39] are used to infer ρR_{peak} from both D_2 and DT implosions.

The energy loss of secondary protons in the compressed D_2-fuel shell shows that the neutron-averaged areal density for $\alpha \sim 2$ implosions is as high as 100 to 110 mg/cm². A secondary proton spectrum from shot 45009 is shown in Fig. 108.13. The figure shows both the measured spectrum (solid circles with statistical error bars) and the birth spectrum (shaded region) in the core. The average energy loss in the dense-fuel shell is several MeV, corresponding to an areal density of 110 mg/cm². The low-energy tail suggests considerable low-mode instability growth late in time. These late-time protons probe regions of significantly higher fuel areal density but not necessarily regions representative of the overall shell areal density. For example, the
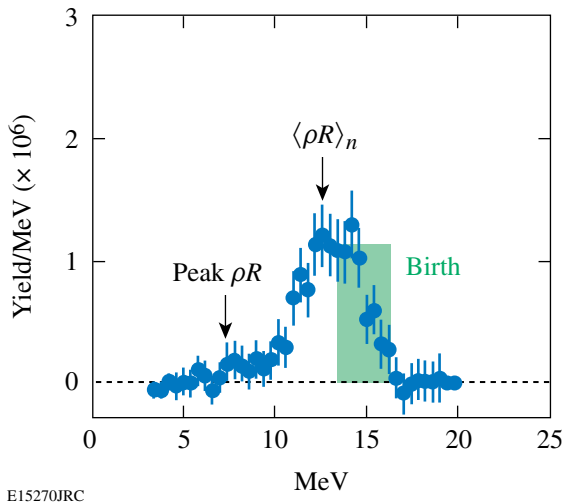
end point of this spectrum (at about 7 MeV) would correspond to an areal density of approximately 250 mg/cm² (based on a total dE/dx of over 5 MeV). For higher-yielding implosions, the areal-density evolution during the burn $\rho R(t)$ can be fit based on the technique described by Frenje and Smalyuk.[40]

The ρR_{peak} can be inferred based on the opacity of the shell by using the core self-emission to effectively backlight the shell. Figure 108.14 shows the measured x-ray spectrum from the core of shot 44948. This shot used a drive pulse to put the fuel shell on an adiabat close to 1. Since the x rays are generated by bremsstrahlung in the hot core, the spectrum is expected to be exponential with the slope related to the electron temperature near peak compression. If the fuel shell is sufficiently dense, x-ray absorption (free-free scattering) occurs and the spectrum deviates from the expected exponential behavior, and this deviation can be used to infer the density of the compressed fuel.[41] The x-ray spectrum in Fig. 108.14 indicates significant absorption between 1 and 2 keV. The opacity of the fuel shell is proportional to $\rho^2 R T^{-1/4}$, where ρ is the mass density of the compressed fuel, ρR is its areal density, and T is the electron temperature (inferred from the slope of the spectrum). The 1-D radiation hydrodynamic code *LILAC*[42] has been used to estimate the mass density ρ and minimum temperature of the compressed fuel by adjusting the temperature of the cold fuel and the thermal conductivity of the

E15270JRC

Figure 108.13
A measured secondary proton spectrum (solid circles) from a cryogenic D_2 implosion ($\alpha \sim 2$) is compared with the expected birth spectrum (shaded box). The protons lose energy as they pass through the dense fuel layer surrounding the hot core. The energy loss is proportional to the areal density of the dense fuel layer. For this implosion, the energy loss implies an areal density in excess of 100 mg/cm²; the low-energy tail suggests the peak areal density is well above 100 mg/cm².

E15271JRC

Figure 108.14
Significant absorption is seen in the continuum x-ray spectrum emitted from the core of a cryogenic D_2 implosion ($\alpha \sim 1$) at x-ray energies below 2 keV. The emitted spectrum is expected to be exponential, and the deviation at low x-ray energies is consistent with a significant fuel areal density. The compressibility of the fuel shell in the 1-D radiation hydrocode *LILAC* can be modified to fit the emitted spectrum to estimate the fuel density. The dashed line shows the expected exponential behavior of the x-ray emission if the opacity is artificially removed in the simulation.

hot core to match the emitted spectrum in both absolute fluence and shape (these adjustments mimic multidimensional mode growth and the consequent reduction in shell compression). The *LILAC* simulation that best agrees with the data is shown as the solid curve. The fuel density in the simulation suggests that ρR_{peak} may be as high as 190 ± 20 mg/cm^2. Two-dimensional simulations are underway to confirm this 1-D fuel-density estimate. The dashed curve in Fig. 108.14 is the predicted x-ray spectrum based on zero opacity. The curve is not purely exponential below 2 keV. If the opacity is calculated based on a purely exponential source spectrum and the density is taken from the *LILAC* simulation, the inferred ρR_{peak} would still be 180 mg/cm^2. Note that, if confirmed by further simulations, this estimate of the density represents a lower limit on the inferred peak areal density—if the density is less than predicted by the simulation, the measured opacity suggests that ρR_{peak} must be larger than the 180- to 190-mg/cm^2 estimate.

Summary

The cryogenic DT targets being imploded on OMEGA are energy-scaled versions of the baseline direct-drive-ignition design for the National Ignition Facility. This is the culmination of nearly three decades of research and development. Most of the components for the x-ray-drive ignition targets are at or near specification.

The β-layering process for producing a smooth inner ice surface in the direct-drive cryogenic DT targets imploded on OMEGA is well understood. The most important aspect of this process is controlling the symmetry of the isotherm on the outer surface of the capsule. This can now be done routinely, and over half of the cryogenic DT capsules imploded on OMEGA met the ignition requirement for the smoothness of the inner ice surface (<1-μm rms in all modes) at shot time. Optical shadowgraphy and phase-contrast imaging are used to characterize the inner ice surface for transparent (e.g., CH or CD shell) and opaque (e.g., Be and foam shells) ablators, respectively. The resolution of these techniques is adequate to characterize the ice smoothness to well below the ignition requirements for both direct and x-ray drives.

The Cryogenic Target Handling System on the OMEGA laser has deep roots in past work. Many of the fundamental concepts employed today were developed nearly three decades ago to perform the first cryogenic DT implosions using DT-filled, thin-glass-shell targets and two-beam irradiation. While these early target designs ultimately did not scale to ignition, the success of the current OMEGA program and the anticipated success of the future NIF ignition experiments owe much to these early pioneers.

REFERENCES

1. J. Nuckolls *et al.*, Nature **239**, 139 (1972).

2. W. J. Hogan, E. I. Moses, B. E. Warner, M. S. Sorem, and J. M. Soures, Nucl. Fusion **41**, 567 (2001).

3. P. W. McKenty, V. N. Goncharov, R. P. J. Town, S. Skupsky, R. Betti, and R. L. McCrory, Phys. Plasmas **8**, 2315 (2001).

4. J. D. Lindl, *Inertial Confinement Fusion: The Quest for Ignition and Energy Gain Using Indirect Drive* (Springer-Verlag, New York, 1998); J. D. Lindl *et al.*, Phys. Plasmas **11**, 339 (2004).

5. S. W. Haan *et al.*, Fusion Sci. Technol. **49**, 553 (2006); S. W. Haan *et al.*, Phys. Plasmas **12**, 056316 (2005); S. W. Haan *et al.*, Nucl. Fusion **44**, S171 (2004).

6. S. Atzeni and J. Meyer-ter-Vehn, *The Physics of Inertial Fusion: Beam Plasma Interaction, Hydrodynamics, Hot Dense Matter*, International Series of Monographs on Physics (Clarendon Press, Oxford, 2004).

7. T. R. Boehly, D. L. Brown, R. S. Craxton, R. L. Keck, J. P. Knauer, J. H. Kelly, T. J. Kessler, S. A. Kumpan, S. J. Loucks, S. A. Letzring, F. J. Marshall, R. L. McCrory, S. F. B. Morse, W. Seka, J. M. Soures, and C. P. Verdon, Opt. Commun. **133**, 495 (1997).

8. C. Stoeckl, C. Chiritescu, J. A. Delettrez, R. Epstein, V. Yu. Glebov, D. R. Harding, R. L. Keck, S. J. Loucks, L. D. Lund, R. L. McCrory, P. W. McKenty, F. J. Marshall, D. D. Meyerhofer, S. F. B. Morse, S. P. Regan, P. B. Radha, S. Roberts, T. C. Sangster, W. Seka, S. Skupsky, V. A. Smalyuk, C. Sorce, J. M. Soures, R. P. J. Town, J. A. Frenje, C. K. Li, R. D. Petrasso, F. H. Séguin, K. Fletcher, S. Padalino, C. Freeman, N. Izumi, R. Lerche, and T. W. Phillips, Phys. Plasmas **9**, 2195 (2002).

9. T. C. Sangster, J. A. Delettrez, R. Epstein, V. Yu. Glebov, V. N. Goncharov, D. R. Harding, J. P. Knauer, R. L. Keck, J. D. Kilkenny, S. J. Loucks, L. D. Lund, R. L. McCrory, P. W. McKenty, F. J. Marshall, D. D. Meyerhofer, S. F. B. Morse, S. P. Regan, P. B. Radha, S. Roberts, W. Seka, S. Skupsky, V. A. Smalyuk, C. Sorce, J. M. Soures, C. Stoeckl, K. Thorp, J. A. Frenje, C. K. Li, R. D. Petrasso, F. H. Séguin, K. A. Fletcher, S. Padalino, C. Freeman, N. Izumi, J. A. Koch, R. A. Lerche, M. J. Moran, T. W. Phillips, and G. J. Schmid, Phys. Plasmas **10**, 1937 (2003).

10. P. W. McKenty, T. C. Sangster, M. Alexander, R. Betti, R. S. Craxton, J. A. Delettrez, L. Elasky, R. Epstein, A. Frank, V. Yu. Glebov, V. N. Goncharov, D. R. Harding, S. Jin, J. P. Knauer, R. L. Keck, S. J. Loucks, L. D. Lund, R. L. McCrory, F. J. Marshall, D. D. Meyerhofer, S. P. Regan, P. B. Radha, S. Roberts, W. Seka, S. Skupsky, V. A. Smalyuk, J. M. Soures, K. A. Thorp, M. Wozniak, J. A. Frenje, C. K. Li, R. D. Petrasso, F. H. Séguin, K. A. Fletcher, S. Padalino, C. Freeman, N. Izumi, J. A. Koch, R. A. Lerche, M. J. Moran, T. W. Phillips, G. J. Schmid, and C. Sorce, Phys. Plasmas **11**, 2790 (2004).

11. F. J. Marshall, R. S. Craxton, J. A. Delettrez, D. H. Edgell, L. M. Elasky, R. Epstein, V. Yu. Glebov, V. N. Goncharov, D. R. Harding, R. Janezic, R. L. Keck, J. D. Kilkenny, J. P. Knauer, S. J. Loucks, L. D. Lund, R. L. McCrory, P. W. McKenty, D. D. Meyerhofer, P. B. Radha, S. P. Regan, T. C. Sangster, W. Seka, V. A. Smalyuk, J. M. Soures, C. Stoeckl, S. Skupsky, J. A. Frenje, C. K. Li, R. D. Petrasso, and F. H. Séguin, Phys. Plasmas **12**, 056302 (2005).

12. J. D. Sethian *et al.*, Nucl. Fusion **43**, 1693 (2003); J. D. Lindl, B. A. Hammel, B. G. Logan, D. D. Meyerhofer, S. A. Payne, and J. D. Sethian, Plasma Phys. Control. Fusion **45**, A217 (2003); R. L. McCrory, S. P. Regan, S. J. Loucks, D. D. Meyerhofer, S. Skupsky, R. Betti, T. R. Boehly, R. S. Craxton, T. J. B. Collins, J. A. Delettrez, D. Edgell, R. Epstein, K. A. Fletcher, C. Freeman, J. A. Frenje, V. Yu. Glebov, V. N. Goncharov, D. R. Harding, I. V. Igumenshchev, R. L. Keck, J. D. Kilkenny, J. P. Knauer, C. K. Li, J. Marciante, J. A. Marozas, F. J. Marshall, A. V. Maximov, P. W. McKenty, J. Myatt, S. Padalino, R. D. Petrasso, P. B. Radha, T. C. Sangster, F. H. Séguin, W. Seka, V. A. Smalyuk, J. M. Soures, C. Stoeckl, B. Yaakobi, and J. D. Zuegel, Nucl. Fusion **45**, S283 (2005).

13. V. A. Smalyuk, V. N. Goncharov, J. A. Delettrez, F. J. Marshall, D. D. Meyerhofer, S. P. Regan, and B. Yaakobi, Phys. Rev. Lett. **87**, 155002 (2001).

14. R. Betti, V. Lobatchev, and R. L. McCrory, Phys. Rev. Lett. **81**, 5560 (1998).

15. S. P. Regan, J. A. Marozas, R. S. Craxton, J. H. Kelly, W. R. Donaldson, P. A. Jaanimagi, D. Jacobs-Perkins, R. L. Keck, T. J. Kessler, D. D. Meyerhofer, T. C. Sangster, W. Seka, V. A. Smalyuk, S. Skupsky, and J. D. Zuegel, J. Opt. Soc. Am. B **22**, 998 (2005).

16. S. H. Glenzer *et al.*, Phys. Plasmas **7**, 2585 (2000).

17. T. M. Henderson and R. R. Johnson, Appl. Phys. Lett. **31**, 18 (1977).

18. J. R. Miller, in *Advances in Cryogenic Engineering*, edited by K. D. Timmerhaus (Plenum Press, New York, 1978), Vol. 23, pp. 669–675.

19. D. L. Musinski *et al.*, Appl. Phys. Lett. **34**, 300 (1979).

20. F. J. Marshall, S. A. Letzring, C. P. Verdon, S. Skupsky, R. L. Keck, J. P. Knauer, R. L. Kremens, D. K. Bradley, T. Kessler, J. Delettrez, H. Kim, J. M. Soures, and R. L. McCrory, Phys. Rev. A **40**, 2547 (1989).

21. R. L. McCrory, J. M. Soures, C. P. Verdon, F. J. Marshall, S. A. Letzring, S. Skupsky, T. J. Kessler, R. L. Kremens, J. P. Knauer, H. Kim, J. Delettrez, R. L. Keck, and D. K. Bradley, Nature **335**, 225 (1988).

22. J. K. Hoffer and L. R. Foreman, Phys. Rev. Lett. **60**, 1310 (1988).

23. A. J. Martin, R. J. Simms, and D. L. Musinski, *KMS Annual Technical Report*, 99, KMS Fusion, Inc., Ann Arbor, MI, KMSF Report No. 1348 (1985) (unpublished).

24. A. J. Martin, R. J. Simms, and R. B. Jacobs, J. Vac. Sci. Technol. A **6**, 1885 (1988).

25. G. W. Collins *et al.*, J. Vac. Sci. Technol. A **14**, 2897 (1996).

26. D. R. Harding, D. D. Meyerhofer, S. J. Loucks, L. D. Lund, R. Janezic, L. M. Elasky, T. H. Hinterman, D. H. Edgell, W. Seka, M. D. Wittman, R. Q. Gram, D. Jacobs-Perkins, R. Early, T. Duffy, and M. J. Bonino, Phys. Plasmas **13**, 056316 (2006).

27. M. J. Bonino, "Material Properties of Spider Silk," M.S. Thesis, University of Rochester, 2003.

28. J. D. Moody *et al.*, J. Phys. IV France **133**, 863 (2006).

29. J. Edwards *et al.*, Phys. Plasmas **12**, 056318 (2005).

30. J. A. Koch *et al.*, Fusion Technol. **38**, 123 (2000).

31. D. H. Edgell, W. Seka, R. S. Craxton, L. M. Elasky, D. R. Harding, R. L. Keck, and M. D. Wittman, Fusion Sci. Technol. **49**, 616 (2006).

32. D. S. Montgomery, A. Nobile, and P. J. Walsh, Rev. Sci. Instrum. **75**, 3986 (2004); B. J. Kozioziemski *et al.*, J. Appl. Phys. **97**, 063103 (2005).

33. S. Pollaine and S. Hatchett, Nucl. Fusion **44**, 117 (2004).

34. D. H. Edgell, W. Seka, R. S. Craxton, L. M. Elasky, D. R. Harding, R. L. Keck, L. D. Lund, and M. D. Wittman, J. Phys. IV France **133**, 903 (2006); D. S. Montgomery *et al.*, J. Phys. IV France **133**, 869 (2006).

35. *LLE Review Quarterly Report* **23**, 125, Laboratory for Laser Energetics, University of Rochester, Rochester, NY, LLE Document No. DOE/SP40200-03 (1985).

36. T. P. Bernat *et al.*, Phys. IV France **133**, 857 (2006).

37. P. B. Radha, J. Delettrez, R. Epstein, V. Yu. Glebov, R. Keck, R. L. McCrory, P. McKenty, D. D. Meyerhofer, F. Marshall, S. P. Regan, S. Roberts, T. C. Sangster, W. Seka, S. Skupsky, V. Smalyuk, C. Sorce, C. Stoeckl, J. Soures, R. P. J. Town, B. Yaakobi, J. Frenje, C. K. Li, R. Petrasso, F. Séguin, K. Fletcher, S. Padalino, C. Freeman, N. Izumi, R. Lerche, and T. W. Phillips, Phys. Plasmas **9**, 2208 (2002).

38. F. H. Séguin, J. A. Frenje, C. K. Li, D. G. Hicks, S. Kurebayashi, J. R. Rygg, B.-E. Schwartz, R. D. Petrasso, S. Roberts, J. M. Soures, D. D. Meyerhofer, T. C. Sangster, J. P. Knauer, C. Sorce, V. Yu. Glebov, C. Stoeckl, T. W. Phillips, R. J. Leeper, K. Fletcher, and S. Padalino, Rev. Sci. Instrum. **74**, 975 (2003).

39. B. Yaakobi, R. Epstein, and F. J. Marshall, Phys. Rev. A **44**, 8429 (1991).

40. V. A. Smalyuk, P. B. Radha, J. A. Delettrez, V. Yu. Glebov, V. N. Goncharov, D. D. Meyerhofer, S. P. Regan, S. Roberts, T. C. Sangster, J. M. Soures, C. Stoeckl, J. A. Frenje, C. K. Li, R. D. Petrasso, and F. H. Séguin, Phys. Rev. Lett. **90**, 135002 (2003); J. A. Frenje, C. K. Li, F. H. Séguin, J. Deciantis, S. Kurebayashi, J. R. Rygg, R. D. Petrasso, J. Delettrez, V. Yu. Glebov, C. Stoeckl, F. J. Marshall, D. D. Meyerhofer, T. C. Sangster, V. A. Smalyuk, and J. M. Soures, Phys. Plasmas **11**, 2798 (2003).

41. F. J. Marshall, J. A. Delettrez, R. Epstein, and B. Yaakobi, Phys. Rev. E **49**, 4381 (1994).

42. M. C. Richardson, P. W. McKenty, F. J. Marshall, C. P. Verdon, J. M. Soures, R. L. McCrory, O. Barnouin, R. S. Craxton, J. Delettrez, R. L. Hutchison, P. A. Jaanimagi, R. Keck, T. Kessler, H. Kim, S. A. Letzring, D. M. Roback, W. Seka, S. Skupsky, B. Yaakobi, S. M. Lane, and S. Prussin, in *Laser Interaction and Related Plasma Phenomena*, edited by H. Hora and G. H. Miley (Plenum Publishing, New York, 1986), Vol. 7, pp. 421–448.

Structural Dynamics of Cryogenic Target Assemblies

Introduction

The laser direct-drive approach to inertial confinement fusion (ICF) utilizes an array of high-power laser beams to uniformly compress a target capsule filled with hydrogen isotopes in a spherically symmetric implosion. Higher fuel densities, and therefore higher yields, may be achieved from targets that are filled with fuel under high pressure and cooled to form an ice layer on the inner surface of the capsule.[1] Cryogenic target assemblies for the OMEGA Laser System currently consist of a 900-μm-diam $\times$ 4- to 6-μm-wall glow discharge polymer (GDP) capsule[2] filled with a 100-μm layer of deuterium and tritium (DT) or deuterium (D_2) ice around a gaseous core. The capsule is suspended on four strands of spider silk from a beryllium frame[3] as shown in Fig. 108.15. During a typical implosion, laser illumination of the target rapidly heats and ablates the outer capsule material. Conservation of momentum drives the remaining capsule material and fuel toward the center of the target sphere where the initially gaseous fuel forms a "hot spot" that ignites fusion reactions, which propagate radially outward through the main fuel layer.[4]

During an implosion, hydrodynamic instabilities in the ablation front can reduce the energy yield by distorting the hot spot or dispersing the main fuel layer. These instabilities, like Rayleigh–Taylor instability in classical fluids, initiate at small irregularities or perturbations in the ablation front. Asymmetries such as uneven laser illumination of the target or the presence of features on the outside surface of the capsule are potential triggers of instability during the acceleration phase of an implosion. While beam smoothing and power balancing can ensure highly uniform illumination at target chamber center (TCC),[5,6] target displacements of 5 μm or more[7] from TCC can unbalance the illumination enough to initiate hydrodynamic instability. Consequently, stringent requirements are imposed on the position of ICF targets at the time of implosion. Target-positioning systems must address both static and dynamic (oscillatory) displacements. While static displacements due to position control resolution, window offsets, and events such as removal of thermal shielding (shroud) immediately before firing the laser are a significant concern, they will be addressed in a future article.

In addition to meeting stringent position stability requirements, the mechanical supports for target capsules must also satisfy thermal and mass symmetry requirements. The mechanical supports must have a low thermal conductivity to minimize thermal gradients that perturb the ice layer within the capsule. Furthermore, the supports must not contribute a significant mass asymmetry to the capsule. Consequently, cryogenic target capsules for the OMEGA Laser System are suspended on four strands of spider silk that have a high modulus of elasticity (6.4 GPa), low density (1200 Kg/m^3), and is available in small diameters (0.9 μm), all of which minimize thermal and mass asymmetries. Furthermore, spider silk remains flexible at cryogenic temperatures.

The displacement amplitude of a capsule assembly is a function of the applied excitation force and the dynamic
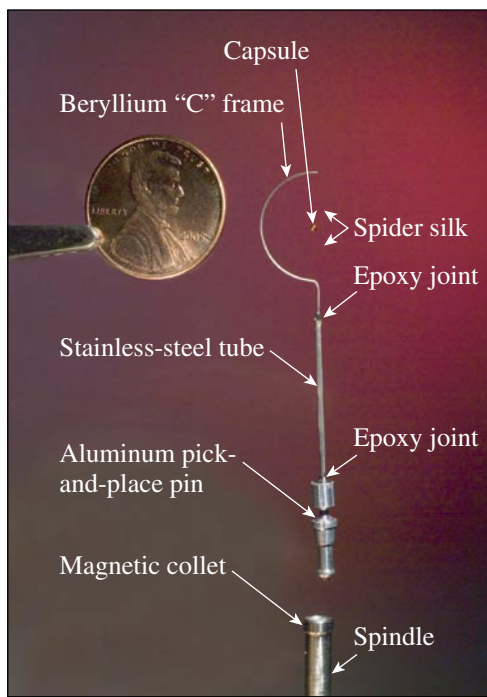

G7559JRC

Figure 108.15
OMEGA Cryogenic Target Assembly.

response characteristics of the target assembly and surrounding structure. Numerous mechanical systems in and around the target chamber may generate periodic or transient forces that excite target vibration. Potential excitation sources include the cryogenic cooling system (helium compressor and cold head), vacuum pumps, solenoids, and forces applied by shroud retraction immediately before firing the laser. Continuously running systems such as induction motors typically excite vibration at discrete frequencies, whereas events that generate transient forces (impulses) such as opening and closing valves usually excite vibration over a broad frequency range. Either reducing excitation forces or isolating the target from the excitation is a very effective means for controlling target vibration, but doing so is not always practical. In such cases, the structural dynamics of the system become important.

The response of multidegree-of-freedom systems, such as the target assembly, to a given forcing function (F) is governed by a set of second-order differential equations so long as the stiffness remains constant; $M\ddot{X} + C\dot{X} + KX = F$. This set of equations relating the masses (M) of the degrees of freedom to the damping (C) and stiffness (K) linking the degrees of freedom constitutes an eigenvalue problem. Under the assumption of a harmonic response, the equations may be solved for eigenvalues that represent the natural frequencies of the system and associated eigenvectors that represent the relative displacement amplitudes of each degree of freedom or mode shape. To avoid high vibration amplitudes due to resonance, the natural frequencies must not coincide with those of forces that are strongly coupled with the associated mode shape. In situations where it is not possible to detune the natural frequencies from excitation sources, such as in the presence of broadband excitation, the vibration amplitude is then limited only by the system damping.

Finite element and experimental modal analyses are used to identify natural frequencies and characterize the associated mode shapes of cryogenic target assemblies for OMEGA. This information is used to interpret *in-situ* vibration data collected at TCC and to investigate the effect of proposed design changes on vibration.

Experimental Modal Analysis

Modal testing is a procedure for directly measuring the natural frequencies and mode shapes of a structure. For reasons of convenience, the target assembly was tested in air at room temperature and atmospheric pressure. A test article, identified as Cryo-ME-21, was constructed using a capsule with mass that is equivalent to a typical production capsule filled with

hydrogen. It is important to note that the dynamic response characteristics under cryogenic conditions are likely to differ from those measured under the test conditions due to changes in the effective stiffness (strain) of the spider silk supporting the capsule and to the reduced damping under vacuum. Differential thermal expansion between the spider silk and beryllium frame and temperature dependence of the elastic moduli are expected to shift the natural frequencies of the target assembly. Material properties of the spider silk are not known at temperatures in the vicinity of the hydrogen's triple point.[8] The impact of cooling on a target's natural frequencies has not been studied in depth, but high-speed video of a few targets suggests that cooling the target increases the silk's natural frequencies by 0% to 7%.

A commercially available shaker system consisting of an electrodynamic actuator and a flexure table was used to excite vibration of the target assembly. The flexure table is intended to limit motion of the target base to translation in one direction. The target assembly was mounted on the shaker table with the beryllium C frame oriented at a 45° angle to the primary motion of the shaker so that both in-plane and out-of-plane modes of vibration could be excited simultaneously, as shown in Fig. 108.16. A random noise signal, capable of exciting vibration over the frequency range of interest up to 2 kHz, was used to drive the shaker at an amplitude of 25 μm, which is consistent with the excitation measured at TCC. Motion of the shaker (excitation) was measured using a piezoelectric accelerometer mounted at the base of the spindle, which connects the target assembly to the stalk (3 cm below the bottom of the pin shown in Fig. 108.15).
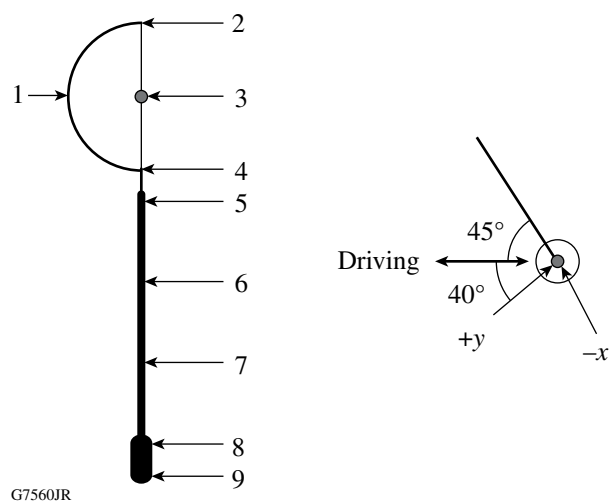

G7560JR

Figure 108.16
Measurement locations on target assembly.

The response of the target assembly to the applied base excitation was measured at the nine points shown in Fig. 108.16. A laser vibrometer was used to measure velocity of each point in two orthogonal directions corresponding approximately to in-plane (x) and out-of-plane (y) of the beryllium C frame. Use of an optical measurement method, as opposed to mounting accelerometers on the target assembly, is necessary to avoid adding mass that would change the natural frequencies of the target assembly.

Data from the test were processed using a multichannel dynamic signal analyzer to compute H1 frequency response function (FRF) estimates[9] that represent the amplitude and phase of the response as functions of frequency. In the FRF calculation, the amplitude at a given frequency is normalized by dividing the response (velocity) of each point on the structure by the excitation (acceleration) at a common reference location on the shaker table. To prevent errors in the fast Fourier transformation (FFT), which forms the basis for this calculation, a weighting window was applied. Discontinuities between the beginning and end values of nonperiodic signals were suppressed by a Hanning window, which reduces the signal amplitude at the beginning and end of the sampling interval. The FRF amplitudes were scaled to resolve the excitation force into the target x and y directions, which were oriented at approximately 45° angles to the excitation. Transmissibility functions were calculated for each measurement point by differentiating the FRF's to produce nondimensional amplitude ratios. Figure 108.17 shows composite transmissibility functions that were created by averaging the transmissibility amplitudes in each direction.
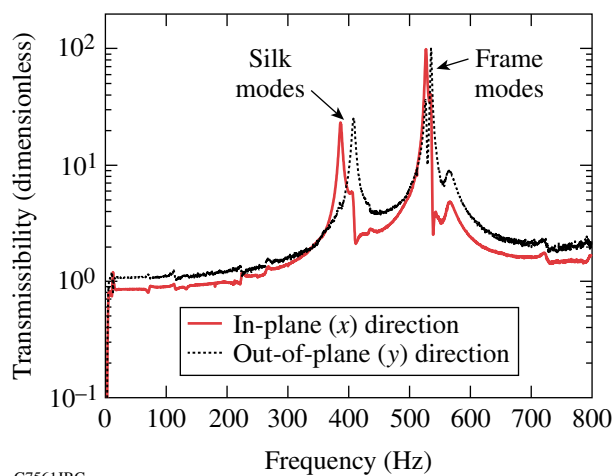
Figure 108.17
Target assembly transmissibility.

G7561JRC

The transmissibility functions from the target assembly were analyzed using Polymax[10] curve-fitting functions to extract natural frequencies, modal damping values, and associated mode shapes. Graphically, the peaks in the transmissibility function indicate natural frequencies, and the relative amplitudes correspond to the mode shapes. Highly damped modes have lower and broader peaks in the transmissibility function. Curve fitting the transmissibility data identified the four stable modes listed in Table 108.I, where damping is expressed both as a percentage of critical and as an exponential decay time constant. At these natural frequencies, the coherence of all the measurements is greater than or equal to 95%. The other peaks in the spectrum (most notable at 570 Hz) are artifacts of secondary axis motion by the shaker.

Table 108.I: Experimental modal analysis results.

Mode	Frequency (Hz)	Damping	Description
1	386	0.6% (0.07 s)	In-plane silk translation
2	408	0.6% (0.07 s)	Out-of-plane silk translation
3	526	0.5% (0.06 s)	In-plane frame bending
4	535	0.1% (0.30 s)	Out-of-plane frame bending

Figure 108.18 shows the mode shapes associated with the four natural frequencies. The relative amplitude and direction of vibration at each measurement location are indicated by arrows. Mode 1 (386 Hz) and mode 2 (408 Hz) are dominated by translation of the capsule in and out of the plane of the C frame under silk tension. In tests on 16 mass-equivalent targets, the natural frequency of the silk mode in the y direction is consistently greater than in the x direction (with an average separation of 24 Hz). In mode 3 (526 Hz) and mode 4 (535 Hz) the mode shapes are dominated by bending of the C frame in plane (x) and out of plane (y) with the capsule moving out of phase with the frame.

Analytical Modal Analysis

A finite-element model of the target assembly was created to predict its dynamic response characteristics. To validate the model, boundary conditions, damping, and room-temperature material properties were used to predict the natural frequencies and mode shapes measured experimentally. Once validated, uses for the model include studies of the sensitivity to variation in uncertain parameters (such as spider silk properties), evaluation of proposed design changes, and prediction of the response
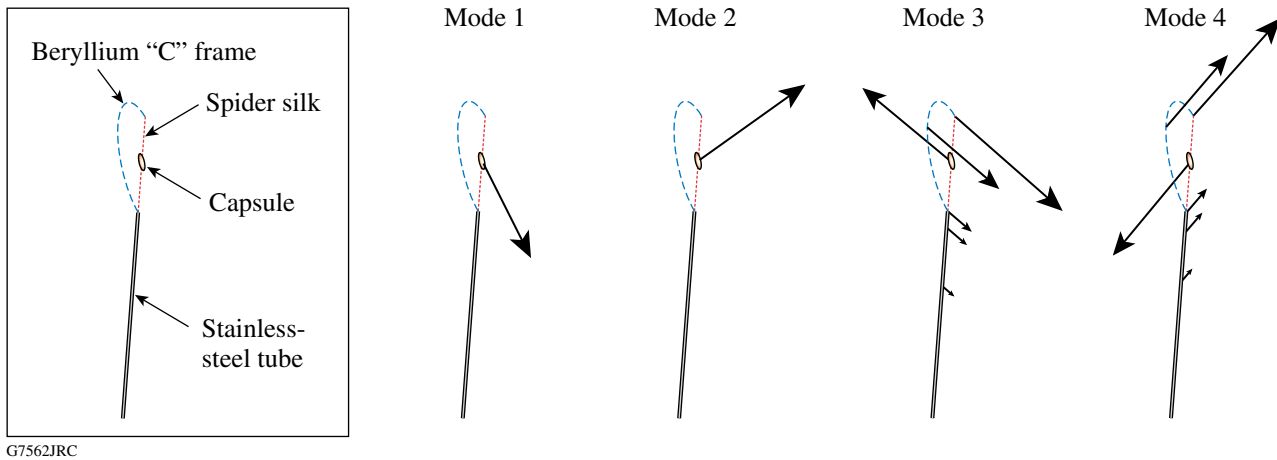
Figure 108.18
Experimental mode shapes.

characteristics under cryogenic conditions (if material properties such as Young's modulus, density, and coefficient of thermal expansion are determined or adequately approximated).

Construction of a Finite-Element Model

The target assembly consists of six relatively simple components (capsule, spider silk, beryllium C frame, stainless-steel tubing, the pin, and adhesives). Material properties for the components are listed in Table 108.II. Damping ratios from the experimental modal analysis results were applied to the model. In general, the system is assumed to respond in a linear manner or approximate a linear response for limited displacements. Specific modeling assumptions and methods for the components are described in the following sections.

Table 108.II: Material properties.

Material	Young's modulus (GPa)	Poisson's ratio	Density (kg/m^3)
Spider silk[6]	6.4	0.24	1200
Stainless steel[11]	193	0.29	7800
Aluminum[11]	70	0.33	2700
Beryllium[11]	300	0.10	1850
Epoxy[11]	5.0	0.35	1550

1. Target Capsule

The target capsule was modeled as a rigid body using a point mass element. Before assembling the target used for the experimental modal analysis (Cryo-ME-21), the capsule mass, outside diameter, and wall thickness were measured to be 56 μg, 878 μm, and 25 μm, respectively. It should be noted that the test article has the same outside diameter and a greater wall thickness than production targets to make its mass equivalent to a DT-filled production capsule. The capsule geometry and mass were used to calculate the rotational moment of inertia about an axis through its center of mass. The rotational inertia of the adhesive attaching the capsule to the four strands of spider silk was assumed to be negligible. While the mass of the test article is the same as that of a filled production target, the rotational inertia will differ because the density of GDP is over 3.5 times that of DT ice. While the rotational inertia of the mass-equivalent capsule is 14% greater than a typical production capsule filled with DT ice, the modes of interest, which consist primarily of translation, are not significantly affected.

The capsule was connected to four spider silks via a series of eight stiff, zero-mass beam elements. Each beam ran from the point mass to contact points on the outer surface of the capsule as measured under a microscope. The separation between the silk contact points in the horizontal (*xy*) plane may vary by up to 10 μm due to ambiguity in the assembly process. Figure 108.19 shows a magnified view of the target-point mass and how it is assembled to the spider silk in the finite-element model.

2. Spider Silk Modeling

The spider silk strands were modeled using link elements that act in tension only. During the assembly process, tension is applied to each strand of silk by stretching to a nominal strain of 5.6%. With the strain below the yield point, the modulus of elasticity was assumed to be constant. The four silk strands supporting the capsule were collected from a single "drop line," which has been shown to have consistent properties over its entire length.[8] Specimens from the same drop line were
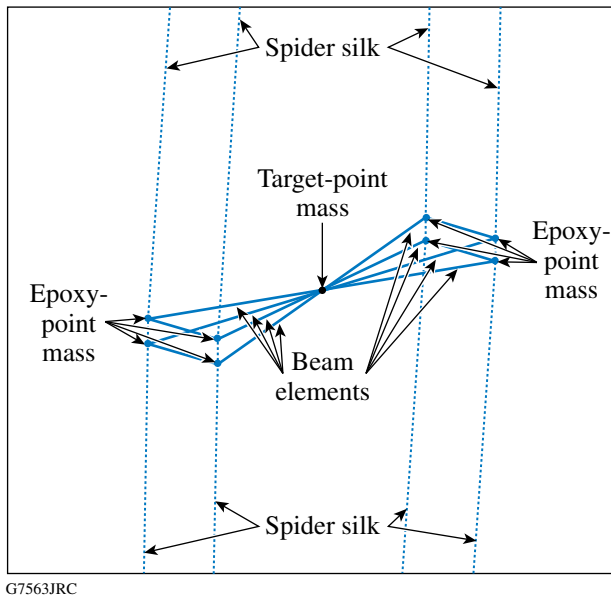
G7563JRC

Figure 108.19
The target-point-mass assembly in the finite-element model.

G7565JRC

Figure 108.21
Silk beryllium connection elements.

analyzed under a scanning electron microscope to determine the number of fibers and their cross-sectional area. Another specimen from the same drop line was tested to determine its modulus of elasticity.

The silk was attached to the target, as shown in Fig. 108.19. Small, stiff, zero-mass beams were used to create the attachment point between the silk and the beryllium C frame. The beams ran from the center of the beryllium wire to the theoretical tangential contact points between the outside diameter of the wire and the silk. Figure 108.20 shows how the model was created. Figure 108.21 is a geometric representation of element size and configuration.
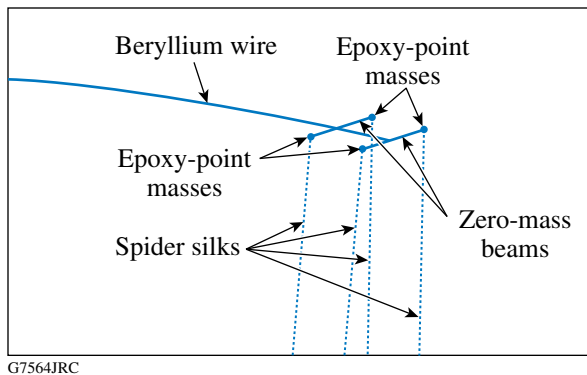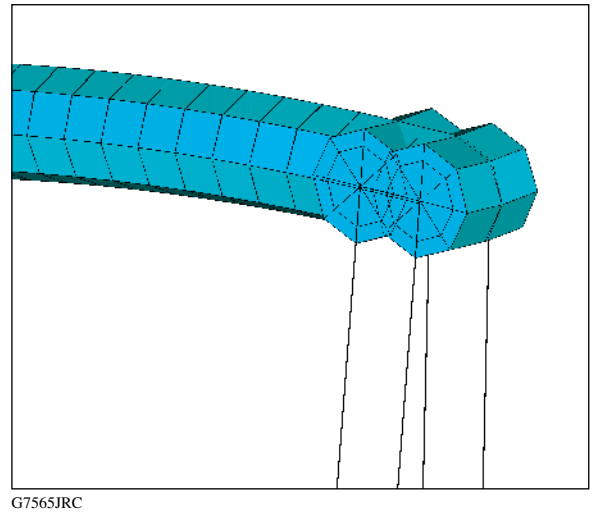

G7564JRC

Figure 108.20
Silk beryllium connection mass.

3. C Frame and Support Tube

Beam elements were used to model the wire frame that supports the spider silk and the tube that connects the frame to the pin. The beryllium-wire C frame was assumed to have a round cross section with a constant diameter determined by measuring the test article. The stainless-steel support tube was assumed to have a circular cross section with constant diameter and wall thickness based on nominal values from the manufacturer.

4. Support Pin and Collet

The support pin at the bottom of the target assembly was modeled using a six-degrees-of-freedom beam element. The magnetic collet joint that attaches the target assembly to the spindle was assumed to be very stiff and was modeled by constraining the pin to the spindle (excitation source) in all six degrees of freedom. If the assumption of an ideal collet joint is not valid, the predicted natural frequencies of the first bending mode will be higher than the measured values. Excitation from the shaker was simulated by applying a harmonic acceleration to the collet in the x and y directions.

5. Epoxy Joints

Epoxy joints connecting the beryllium C frame to the stainless-steel tube and the stainless-steel tube to the pick-and-place pin were modeled using six single-degree-of-freedom spring elements. The springs were created between two coincident nodes. Half of the mass of the epoxy joint was applied to each of the coincident nodes. Figure 108.22 shows a cross section of a representative pin joint. The C-frame joint was not analyzed due to hazards associated with machining beryllium. During assembly, the tube is pushed against one side of the hole in the pin as shown in Fig. 108.22.
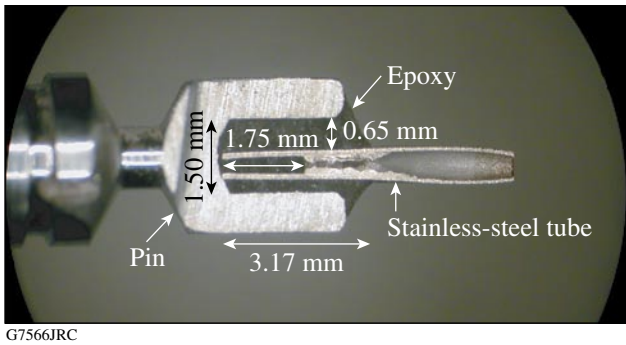
Figure 108.22
Cross section of pin and stainless steel tube.

Likewise, the beryllium wire is pushed against the side of the tube in the positive *x* direction as shown in Fig. 108.23. Detailed finite-element models of the epoxy joints were used to assess their stiffness in each direction. Forces and bending moments were applied individually in each direction, and solutions were obtained for the resulting displacements. The effective stiffness of the joint was calculated and applied to the corresponding spring elements in the target model; however, the mass and stiffness of epoxy in the joints may vary from target to target.
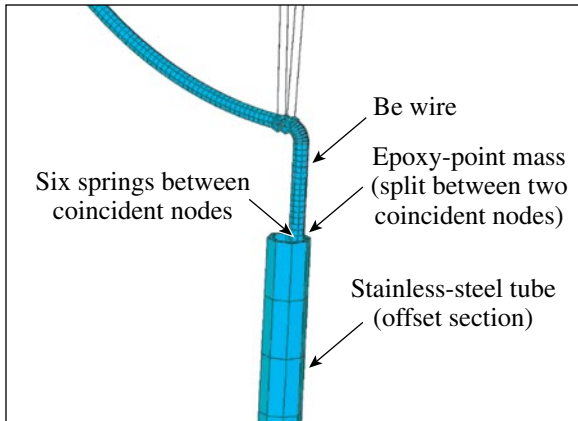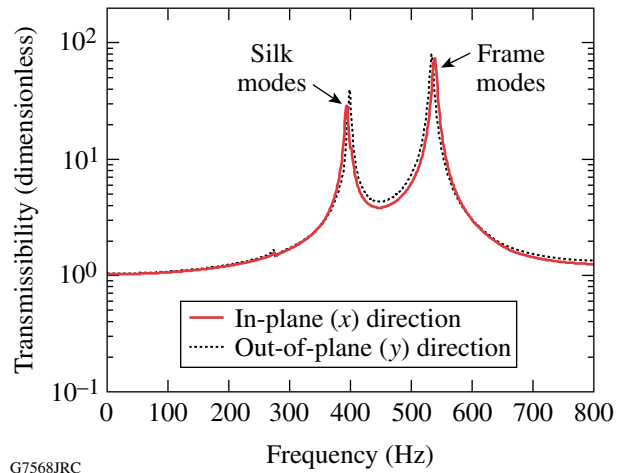

Figure 108.23
Beryllium wire connection to stainless-steel tube.

Analysis Results

The model was used to calculate the dynamic response characteristics of the target assembly at room temperature. Natural frequencies and associated mode shapes of the target assembly were calculated through modal analysis of the model. Damping values from the experimental modal analysis results, which represent both structural and aerodynamic affects, were applied to the model. A harmonic analysis based on supposition of the response to a sine sweep was used to calculate the frequency response function shown in Fig. 108.24.

Figure 108.24
Transmissibility functions.

Correlation of Analytical and Experimental Results

The model was validated by comparing the predicted frequencies and mode shapes with the experimental values. Table 108.III shows the correlation between the measured natural frequencies and the corresponding predicted values. Prediction of frequencies within 3% of the experimental values suggests that the model is valid for assessments of potential design changes and sensitivity studies.

Table 108.III: Natural frequency correlation.

Mode description	Experimental frequency (Hz)	Analytical frequency (Hz)	Difference
In-plane (*x*) silk translation	386	393	1.9%
Out-of-plane (*y*) silk translation	408	400	–1.9%
In-plane (*x*) frame bending	526	538	2.3%
Out-of-plane (*y*) frame bending	535	535	0.0%

The mode shapes associated with the largest peaks in the FRF's are similar to the experimental results presented in Fig. 108.18. At 278 Hz, the model predicts a mode dominated by the capsule spinning about the *z* axis with an orbital component that produces translation when the geometric center of the silk/capsule contact points is offset from the capsule's center of mass. The laser vibrometer used in the experiment measures only translation and is therefore not well suited to detect the first mode. While a small peak in the experimental FRF (268 Hz) corresponds closely with the predicted frequency of the first rotational mode, the peak

is attributed to a mode of the shaker. Modal assurance criteria (MAC)[12] are used to compare the predicted and experimental mode shapes dominated by translation of the measurement points. A scalar MAC value is calculated for each pair of analytical and experimental mode shapes to determine their consistency. Fundamentally, the MAC values are based on "R^2" correlation coefficients used in linear regression. A MAC value close to 100% indicates a high degree of correlation, and a value close to zero indicates uncorrelated modes. The MAC matrix shown in Table 108.IV indicates that the predicted mode shapes correlate closely with the experimental modes shapes at corresponding frequencies (diagonal terms in the matrix).

Table 108.IV: Modal assurance criteria.

		Experimental			
	Frequency (Hz)	386	408	526	535
Analytical	393	93	16	16	12
	400	6	84	11	18
	538	26	0	84	17
	535	0	26	16	82

The separation between the *x*- and *y*-direction silk modes near 400 Hz is affected by a variety of parameters including the silk attachment offset from the capsule center of mass, the distance between adjacent points, and uneven silk tension. However, the cumulative effect of improved model fidelity in these areas separates the silk modes by only 7 Hz and does not explain the measured 22-Hz separation. Furthermore, the fact that the out-of-plane silk mode consistently has a higher natural frequency (24±6 Hz on average for mass-equivalent targets) suggests that a systematic source of asymmetry remains unmodeled. However, none of the experimental data collected to date suggests a correlation between the gain (amplitude) and frequency separation of the silk modes.

The model predicts a natural frequency of the in-plane, frame-bending mode, which is higher than the out-of-plane mode. While the experimental results presented here contradict the model's prediction, data from eight similar mass-equivalent targets support the prediction. On average the in-plane mode has a natural frequency that is higher by 0.6±5.9 Hz. This variability is consistent with sensitivity studies performed on the quantity and distribution of adhesive and assembly tolerances in the epoxy joints.

Applications

Information gained from the study of target dynamics is being used to understand and reduce capsule vibration at TCC. During simulated shots (without firing the laser), the vibration of mass-equivalent target capsules has been measured with high-speed video (HSV) cameras. Analysis of the data from two cameras with roughly orthogonal views yields three-dimensional capsule displacements at frequencies up to 1 kHz. The broadband vibration amplitude varies from 5 to 100 μm at the time when the laser would fire (less than 100 ms after retraction of a thermal shroud that maintains the capsule at 20 K). Auto-power spectra functions calculated from the HSV data indicate that capsule displacement is typically dominated by vibration at a few discrete frequencies, as shown in the spectrum from a representative target in Fig. 108.25. The HSV measurements and modal test were performed on different targets. The *x*- and *y*-direction, silk-mode natural frequencies of the target from which the HSV data were collected were 254 and 275 Hz, respectively, and the frame-mode natural frequencies were 592 and 589 Hz, respectively. Two peaks in the HSV auto-power spectrum (270 and 291 Hz) correspond very closely with the silk-mode natural frequencies. A 10-Hz decrease in the frequencies of these two peaks during the first few seconds after shroud removal suggests that the governing stiffness decreases quickly (probably due to warming of the spider silk). Based on observation of similar sets of corresponding peaks from other targets (at different frequencies), these peaks in the HSV auto-power spectra are attributed to the silk modes. However, the frame modes, which do not typically appear in the HSV data, are either not excited or are more heavily damped. Consequently, efforts to control target vibration at TCC need to focus on the silk modes and the peaks around 50 Hz, which are not attributable to the target assembly. The modes around 50 Hz are not discussed in this work.
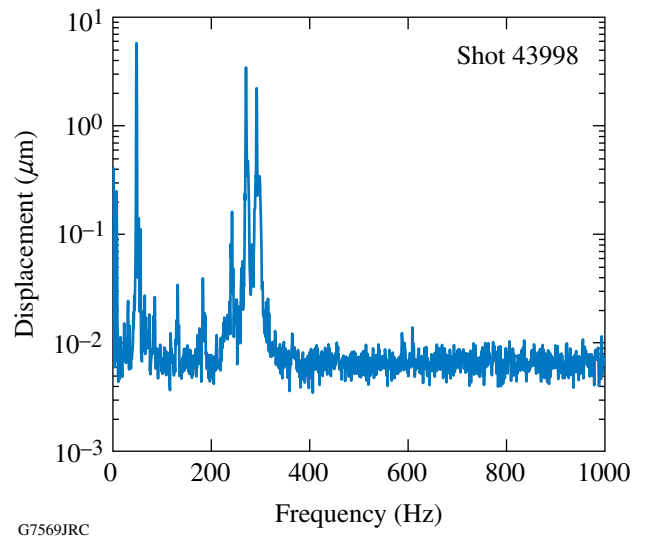

G7569JRC

Figure 108.25
High-speed video spectrum.

Frequency response functions of production targets are measured at one location (the capsule) for quality-assurance purposes before filling the capsule with fuel. The silk-translation natural frequencies of the 66 targets produced from May through September 2006 ranged from 650 Hz to over 1200 Hz. Note that the empty capsule has considerably less mass and therefore higher silk-translation natural frequencies than the mass-equivalent target. The silk-translation modes of empty production targets are also more heavily damped when tested on the shaker due to the reduced mass and increased velocity. The frame-mode natural frequencies of production targets are typically very close to those of mass-equivalent targets. Figure 108.26 shows an FRF from a representative production (target ID Cryo-2062-669) target with an empty capsule.
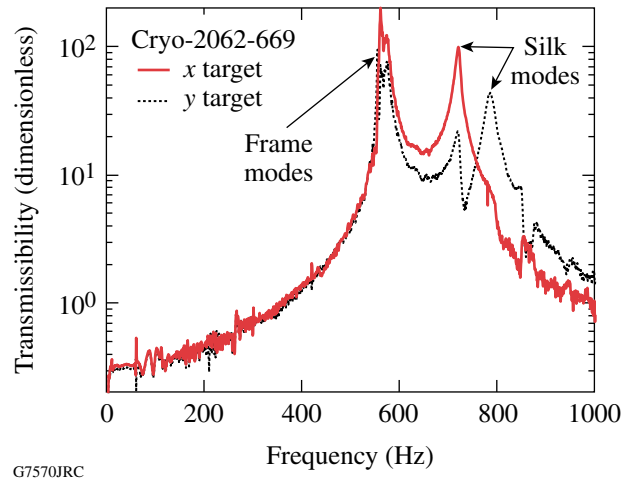
The finite-element model was used to predict the dynamic response characteristics of the production target (Cryo-2062-669) once the empty capsule was filled with either 33 μg of D_2 or 42 μg of DT fuel. The model, which does not account for thermal effects, predicts silk natural frequencies of 410 and 450 Hz when filled with D_2 and 380 and 415 Hz when filled with DT. The impact of cooling on target natural frequencies has not been studied in depth, but high-speed video of a few targets suggests that cooling the target increases the silk natural frequencies by 0% to 7%. Once cooled, the target is expected to have natural frequencies of 455 and 495 Hz if filled with D_2 and frequencies of 420 and 455 Hz if filled with DT.

G7570JRC

Figure 108.26
Experimental FRF of an empty production target capsule.

Variability in the spider silk dimensions and material properties is an unfortunate consequence of working with a naturally occurring material. Sensitivity of the target assembly dynamics to variations in the spider silk properties was investigated with the finite-element model. For an unfilled target, Fig. 108.27 shows the predicted variation in natural frequency of the first translational silk mode as a function of strain, silk modulus, silk diameter, and capsule mass. For an initial strain of 5.6% (the nominal value in the current production process),
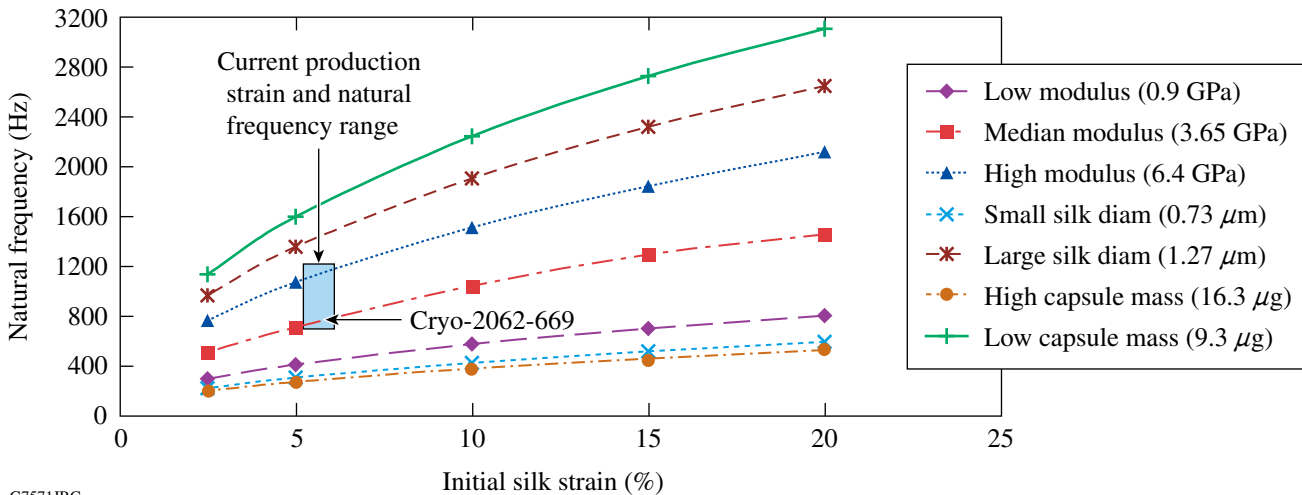

G7571JRC

Figure 108.27
Silk mode sensitivity to strain, modulus, diameter, and capsule mass.

the natural frequency of the first silk translation mode can vary by approximately 670 Hz due to a three-standard-deviation variation in the elastic modulus.[8] Variation in the diameter of the silk (three standard deviations) increases the range to 1050 Hz. Variations in capsule wall thickness from 3.6 μm to 6.3 μm affect the silk translation natural frequencies by changing the mass (9.5 to 16.5 μg) and increasing the range of natural frequencies to 1330 Hz.

The predicted mean and standard deviations of silk-mode natural frequency based on the sensitivity analysis (920±220 Hz) are greater than the values (865±160 Hz) obtained from measuring the natural frequencies of the 66 targets produced from May through September. However, the experimental bandwidth of the shaker was limited to 1200 Hz, and applying this constraint to the FEA data (under the assumption of a Gaussian distribution) reduces the range to 910±201 Hz. Future target-frequency-response tests will have a 2-kHz bandwidth that encompasses the three-standard-deviation range of silk-mode frequencies. The discrepancy between the predicted and measured frequency ranges indicates that the effective modulus of the tested targets is lower and more consistent than published values. Seasonal effects on silk properties may broaden the experimental uncertainty bounds; these will be studied in the future.

Filling the targets with D_2 or DT fuel changes the predicted (three-standard-deviation) range of silk-mode natural frequencies (assuming 5.6% initial strain) to 150 to 750 Hz, and 130 to 670 Hz, respectively. The variation in silk-mode natural frequencies could be reduced by adjusting the silk strain during target fabrication to compensate for variations in silk properties. However, the elastic modulus measurement process employed in this study would not be practical for routine use in target fabrication. For the purpose of tuning the silk-mode natural frequencies, a more expedient and less accurate measurement would suffice.

Overlap between the frequency ranges for the frame and silk translation modes presents the possibility of coupling between the modes. As a silk mode and a frame mode approach the same frequency, the associated mode shapes shown in Fig. 108.18 become increasingly similar. The effect of coupling was investigated as a potential cause for high vibration of some production targets. Interaction between the modes is measured in terms of the target capsule's transmissibility value (gain) at the natural frequencies. The FRF's in Fig. 108.28 illustrate the effect of increasing the silk-mode natural frequency. In addition to increasing the gain of both silk and frame modes, coupling

also shifts the frame-mode frequencies higher by roughly 75 Hz. Figure 108.29 shows the gain of the frame and silk modes plotted as functions of the silk-mode natural frequency. When the silk-mode natural frequency coincides with that of the frame modes (526 Hz and 538 Hz), coupling increases the frame-mode gain by a factor of 4 and the silk-mode gain by a factor of 2 with respect to the measured silk-mode natural frequency (400 Hz).
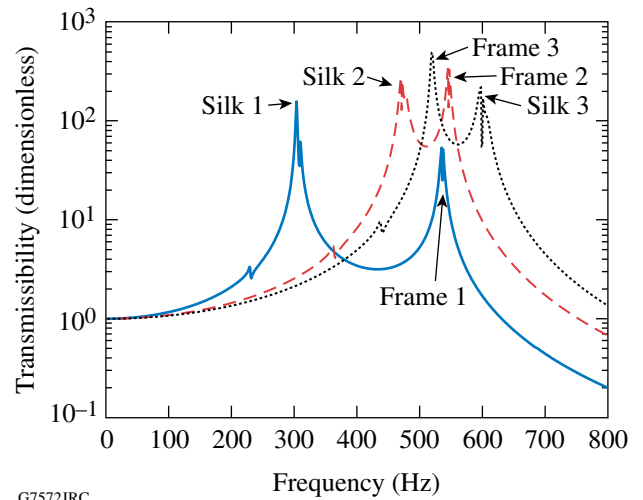
G7572JRC

Figure 108.28
FRF's showing coupling effect.
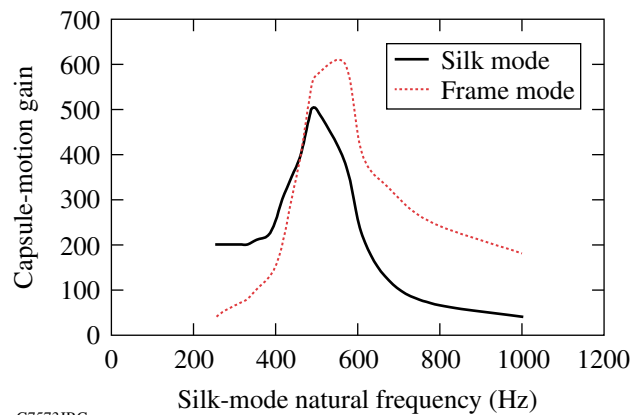
G7573JRC

Figure 108.29
Silk- and frame-mode coupling.

To prevent coupling, acceptance criteria will be established for an empty target's natural frequencies. The single-degree-of-freedom model shown on p. 180 provides simple and accurate (based on correlation with the finite-element model) predictions of the silk-mode natural frequencies of a fully fueled target (f_{full}) based on the measured natural frequency when

empty (f_{empty}). Targets with fully fueled silk natural frequencies between 85% and 125% of the frame natural frequencies will be rejected.

$$f_{full} = f_{empty} \times \sqrt{\frac{\text{capsule mass}}{\text{capsule mass} + \text{fuel mass}}}. \qquad (1)$$

Analysis of the HSV data reveals several clues regarding the excitation. First, excitation of silk translation modes in targets with silk natural frequencies ranging from 270 to 570 Hz indicates the presence of a broadband excitation source such as an impulse or random noise. Second, the absence of vibration at the frame-mode natural frequencies implies weak coupling between the excitation source and frame modes or high damping of the frame modes. Potential excitation sources including shroud separation forces and target clearance to the thermal shroud during retraction are currently being investigated.

Conclusion

The analytical model predicts natural frequencies of translation modes within 3% of those obtained experimentally. Correlation of target capsule vibration at TCC with the target dynamic response characteristics obtained from this study indicates that the silk modes are a primary cause of capsule displacement during shots. While increasing the silk-mode natural frequencies would typically reduce the displacement amplitude, coupling between the silk and frame modes is believed to counteract the benefits until the silk-mode frequencies are significantly greater than those of the frame modes. Increasing the silk natural frequencies would probably introduce significant mass asymmetry. Therefore, the authors are designing a new cryostat that will not excite the silk modes and are exploring stiffer capsule-support concepts.

REFERENCES

1. T. C. Sangster, J. A. Delettrez, R. Epstein, V. Yu. Glebov, V. N. Goncharov, D. R. Harding, J. P. Knauer, R. L. Keck, J. D. Kilkenny, S. J. Loucks, L. D. Lund, R. L. McCrory, P. W. McKenty, F. J. Marshall, D. D. Meyerhofer, S. F. B. Morse, S. P. Regan, P. B. Radha, S. Roberts, W. Seka, S. Skupsky, V. A. Smalyuk, C. Sorce, J. M. Soures, C. Stoeckl, K. Thorp, J. A. Frenje, C. K. Li, R. D. Petrasso, F. H. Séguin, K. A. Fletcher, S. Padalino, C. Freeman, N. Izumi, J. A. Koch, R. A. Lerche, M. J. Moran, T. W. Phillips, and G. J. Schmid, Phys. Plasmas **10**, 1937 (2003).

2. A. Nikroo *et al.*, General Atomics, San Diego, CA, GA–A23881 (2002).

3. D. T. Goodin *et al.*, in *Proceedings of the 17th IEEE/NPSS Symposium on Fusion Engineering* (IEEE, New York, 1997), Vol. 1, pp. 309–312.

4. J. D. Lindl, Phys. Plasmas **2**, 3933 (1995).

5. P. W. McKenty, V. N. Goncharov, R. P. J. Town, S. Skupsky, R. Betti, and R. L. McCrory, Phys. Plasmas **8**, 2315 (2001).

6. D. D. Meyerhofer, J. A. Delettrez, R. Epstein, V. Yu. Glebov, V. N. Goncharov, R. L. Keck, R. L. McCrory, P. W. McKenty, F. J. Marshall, P. B. Radha, S. P. Regan, S. Roberts, W. Seka, S. Skupsky, V. A. Smalyuk, C. Sorce, C. Stoeckl, J. M. Soures, R. P. J. Town, B. Yaakobi, J. D. Zuegel, J. Frenje, C. K. Li, R. D. Petrasso, D. G. Hicks, F. H. Séguin, K. Fletcher, S. Padalino, C. Freeman, N. Izumi, R. Lerche, T. W. Phillips, and T. C. Sangster, Phys. Plasmas **8**, 2251 (2001).

7. R. S. Craxton, ed. *OMEGA Upgrade Preliminary Design*, Laboratory for Laser Energetics, University of Rochester, Rochester, NY, LLE Document No. DOE/DP 40200-101 (1989).

8. M. J. Bonino, "Material Properties of Spider Silk," M.S. Thesis, University of Rochester, 2003.

9. J. S. Bendat and A. G. Piersol, *Engineering Applications of Correlation and Spectral Analysis* (Wiley, New York, 1980).

10. LMS International, Leuven, Belgium.

11. A material properties database, MatWeb is a division of Automation Creations, Inc., Blacksburg, VA 24060, December 2006, http://www.matweb.com (11 December 2006).

12. R. J. Allemang and D. L. Brown, in *Proceedings of the International Modal Analysis Conference & Exhibit* (Society for Experimental Mechanics, Schenectady, NY, 1982), pp. 110–116.

Measuring *E* and *B* Fields in Laser-Produced Plasmas with Monoenergetic Proton Radiography

The generation of electromagnetic fields (*E/B*) by interactions of laser light with matter is a process of fundamental interest in high-energy-density (HED) physics.[1] The primary mechanism behind field formation is the loss of energetic electrons from the heated region, resulting in the breakdown of neutrality. Many processes can then contribute to field generation and evolution, but their relative importance depends on interaction parameters.[1–5] For long-pulse, low-intensity laser light, the dominant source for *B*-field generation is noncollinear electron density and temperature gradients ($\nabla n_e \times \nabla T_e$); the dominant source for *E* fields is $\nabla P / n_e$, a consequence of nonuniform laser irradiation.[1–5] For circular laser spots, the *B* fields have a toroidal configuration with scale length comparable to the spot size. In a regime with low *Z* and high temperature, where resistivity is low, *B*-field growth is usually linear in time and is balanced primarily by convective losses (i.e., the *B* field is "frozen in").[1–3,5] Under these circumstances, *B*-field evolution can be described by the Faraday equation combined with a simplified version of the generalized Ohm's law:

$$\frac{\partial \mathbf{B}}{\partial t} \approx \nabla \times (\mathbf{v} \times \mathbf{B}) - \frac{1}{en_e}\nabla n_e \times \nabla T_e, \qquad (1)$$

where **v** is the plasma fluid velocity.

In addition to their importance to fundamental HED physics, these fields have important implications for several current problems. In inertial confinement fusion (ICF), magnetic fields (~MG) are generated inside a hohlraum by long-pulse (~1-ns) laser illumination.[6–8] Such fields can reduce heat flow since cross-field thermal conductivity is modified by a factor of $\left(1 + \omega_{ce}^2 \tau^2\right)^{-1}$, where ω_{ce} is the electron gyro frequency and τ is the collision time. The result is altered distributions of electron temperature and density, enhancing laser–plasma instabilities, and implosion asymmetries.[6–8] The experiments described here are the first to directly measure fields generated by the types of laser beams used in direct- and indirect-drive ICF.

Previous work focused largely on short-pulse, high-intensity lasers,[9–11] and field measurements were based on Faraday rotation,[10] probes,[4] or high-order laser harmonics.[11] It has also been proposed that proton radiography could provide a method for measuring fields through the deflections they induce in proton trajectories; recent work by Mackinnon *et al.*[12] demonstrated that high-resolution images containing deflection information could be obtained, although no direct connections were made between images and fields. In their experiment, backlighter protons were generated by irradiating a solid tungsten target with a high-intensity petawatt laser beam (300-fs duration with an intensity of 1×10^{19} W/cm²); the result was a large proton flux and a continuous energy spectrum up to ~50 MeV. These protons were passed through a mesh and used to image a plasma generated by a single laser beam (300 ps) on a 120-μm Cu wire. More recently, work by Romagnani *et al.*[13] utilized side-on proton radiography to study the *E* field generated by a high-intensity (~10^{18} W/cm²), short-pulse (~1.5-ps) laser driving an Au foil; the probing proton flux had a continuous energy spectrum and was generated from a 10-μm Au foil irradiated by an ~300-fs-long, 2×10^{19} W/cm² laser pulse.

A novel imaging technology has been developed that combines a monoenergetic proton backlighter with a matched detection system.[14,15] Protons are generated as nuclear fusion products from the reaction $D + {}^3He \longrightarrow \alpha + p$ in exploding-pusher implosions of D³He-filled, glass-shell capsules;[16] the proton birth energy is $E_p = 14.7$ MeV with a small amount of thermal broadening. For the experiments described here, backlighter implosions were driven by 20 OMEGA laser beams; a typical measured proton spectrum is shown in Fig. 108.30, indicating a proton yield of ~3×10^8. The spatial size of the proton source was measured with a proton-emission imaging system,[17] which determined that the source was nearly spherical and had approximately a Gaussian radial emission profile with a full width at half maximum (FWHM) of ~45 μm. The timing of the proton production was measured by a proton temporal diagnostic (PTD);[18] protons were produced during an interval of ~150 ps, and the time of onset of the burn was adjustable. The protons were detected by a CR-39 track detector configured for imaging.[15] This approach has distinct advantages over radiography with broadband proton sources (such as intense-laser–induced sources); it allows us to optimize

a special detector design and to make precise connections between particle deflections and field magnitudes.
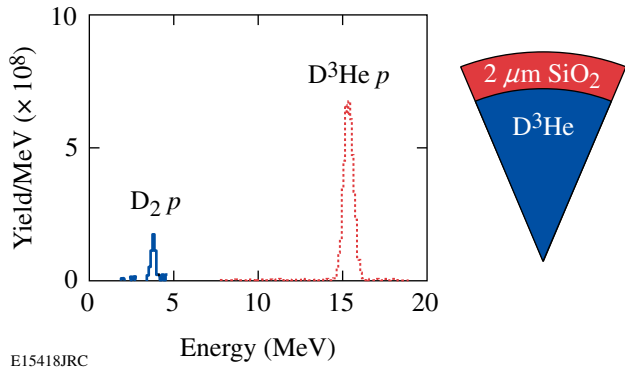

E15418JRC

Figure 108.30
Measured energy spectra of monoenergetic D³He and D_2 protons generated in an implosion of a thin-glass shell filled with D³He gas (OMEGA shot 42767). The data described in this article correspond to the D³He protons; use of the 3-MeV D_2 protons will be explored in future work.

Our experimental setup, illustrated schematically in Fig. 108.31, was designed for quantitative imaging of fields generated by the interaction of a laser with a plastic (CH) foil. In each experiment, 14.7-MeV backlighter protons were passed through meshes with 150-μm periods (to form discrete, 75-μm beamlets with ~2000 protons each) and used to simultaneously image two separate laser–plasma interactions: one imaged face on and the other imaged from the side. The laser–plasma interactions on each CH foil were induced by a single laser *interaction* beam with a 0.351-μm wavelength, incident 23° from the
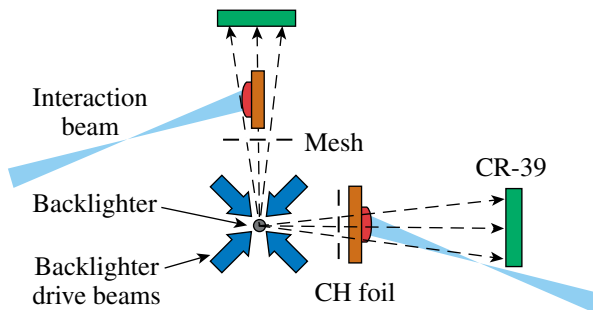

E15419JRC

Figure 108.31
Schematic illustration of our experimental setup and the physical relationship among the proton backlighter (imploded D³He-filled capsule), mesh, CH foils, CR-39 imaging detectors, and OMEGA laser beams, as used for simultaneous radiography of two separate laser–foil interactions (face-on and side-on). The distances of components from the backlighter were 0.8 cm for mesh, 1 cm for foil, and 36 cm for the detector.

normal direction. The laser had a square pulse either 1 ns or 0.6 ns long, with an energy of 500 J or 250 J. The diameter of the laser beam on the foil (containing 95% of the energy deposition) was determined by the phase plate,[19] which was either SG2 (500 μm) or SG4 (800 μm); the resulting laser intensity was of the order of 10^{14} W/cm². X-ray emission indicates that the plasmas have $n_e \sim 10^{20}$ to 10^{22}/cm³ and $T_e \sim 1$ keV.

The interaction of the laser with the CH foil was modeled with the 2-D *LASNEX* hydrocode.[20] The magnetic-field package[21] in *LASNEX* includes the full Braginskii cross-field transport model and spontaneously generates fields in the presence of nonparallel temperature and density gradients. The proton transport through these fields and plasmas was modeled with the *LSP* hybrid PIC (particle-in-cell) code.[22] Because only a single energy (14.7 MeV) was used, directly comparing simulations and experimental data provides unambiguous quantitative information about fields. Simulations[8] indicate that face-on radiography is largely sensitive only to the *B* field,[23] while side-on radiography is primarily sensitive only to the *E* field. This allows *E* and *B* fields to be measured separately.

Figure 108.32(a) shows face-on images acquired from three different shots. Laser timing was adjusted so the 14.7-MeV protons arrived at the foil at 0.0, 0.33, and 0.64 ns, respectively, after the laser interaction beam was turned on. The laser beam had an SG4 phase plate (800-μm diameter), with a 1-ns pulse and 500 J of energy. The measured images are very similar to the *LASNEX + LSP* simulations shown in Fig. 108.32(b), in terms of both the time dependence of the apparent diameter of the plasma bubble and the amount of distortion of the mesh pattern inside the plasma bubble region due to the magnetic lens effect. Significant distortions occurred near the border of the bubble, where the proton beamlets were deflected by a strong *B* field and piled up to form a sharp circular ring; smaller distortion at the center indicates a smaller, but measurable *B* field there. These features are largely reproduced by simulations illustrated in Fig. 108.33, showing that toroidal *B* fields are concentrated on a hemispherical shell surrounding the ablative plasma bubble; they have maximum amplitude near the edge but fall to zero at the center. The *B* fields can be estimated from the data by using the linear displacement ξ of the beamlets in an image from where they would be without the distortion, together with the geometry of the imaging system and the scale length ($L_B \equiv B/\nabla B$) in the direction perpendicular to the image $\left(B \propto E_p^{0.5} L_B^{-1}\right)$. L_B was estimated to be $L_B \sim L_\parallel \equiv n_e/\nabla n_e$, which is about the radius of the plasma bubble. This estimated L_B is within a factor of 2 of what one would infer from the simulations near the edge of the bubble. The inferred peak *B* values of about 0.5 MG agree

(a)

0.00 ns   0.33 ns   0.64 ns

2.3 mm

(b)

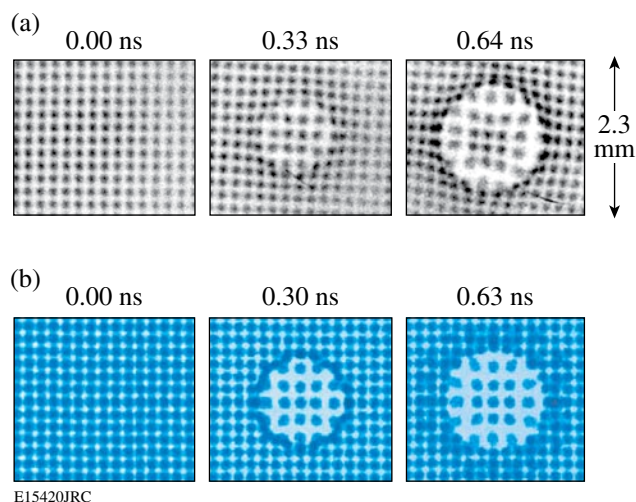0.00 ns   0.30 ns   0.63 ns

E15420JRC

Figure 108.32

(a) Measured face-on, 14.7-MeV proton images showing the effects of the magnetic field generated by laser–plasma interactions. Each image is labeled by the time interval between the arrival at the foil of the interaction beam and the arrival of the imaging protons. The interaction beam had a 1-ns pulse length. The labeled dimensions of the image are scaled to the location of the foil. Note that the apparent 188-μm separation of beamlets in the unperturbed sections of the images corresponds to the separation at the mesh (150 μm) magnified by the ratio (source-to-foil distance)/(source-to-mesh distance). (b) Images simulated by *LASNEX + LSP* for the conditions that produced the experimental images shown in (a).

0.05   0.35   0.65   0.95   MG

0.06 — 0.30 ns   — 0.63 ns

0.03

R (cm) 0.00

−0.03

−0.06

0.08   0.04   0.00   0.08   0.04   0.00

Z (cm)   *Z* (cm)

E15421JRC

Figure 108.33

Time evolution of *B*-field strength on a cross section of the plasma bubble, simulated by *LASNEX* for the experimental conditions of Fig. 108.32. In each case, the horizontal coordinate *z* is the distance from the foil (assuming the laser is incident from the left), and the vertical coordinate *R* is the distance from the central axis of the plasma bubble. The largest field occurs near the surface of the plasma bubble, and the largest line integral parallel to the *z* direction occurs near the bubble edge.

well with simulations. In contrast to previous experiments and simulations, where the plasmas were usually generated by a short-pulse laser (~1 to 100 ps), we used long pulses that result in time evolution on a scale longer than our 150-ps sampling time; this allows us to clearly measure the time evolution of the field structure as shown in Fig. 108.32.

We can be more quantitative about data-simulation comparisons. The displacements ξ of individual beamlet positions in the images represents not lateral displacements at the foil but angular deflections from interactions with fields near the foil that result in lateral displacement at the detector. Angles of deflection can be inferred directly from displacements ξ by using the experiment dimensions, but quantitative comparisons between measured and simulated images are most easily made in terms of image dimensions and values of ξ. In Fig. 108.32, for example, we can look at the apparent diameter of the plasma bubbles (where beamlet "pileup" occurs). At ~0.3 ns it is about 1.5 mm for both simulation and data, although the value for the real image is harder to measure exactly because the pileup position is not as well defined. At ~0.6 ns, both data and simulation show diameters of about 1.6 mm. Next we can look at the displacements ξ in the centers of the images, which are proportional to the magnetic field in the centers of the bubbles. At ~0.3 ns, ξ is about 40 μm for both data and simulation, showing good agreement at that time. At 0.64 ns, the agreement is not so good since ξ is about 50 μm for the simulation but approximately zero for the data. Finally, we look outside the bubbles and see that the data show a slight mesh distortion that is not apparent in the simulations; this could suggest that the simulations underestimated the plasma resistivity, or that the interaction laser had more energy in its wings than assumed in the simulations. The simulations have done a good job of modeling the overall behavior of the plasma bubble, indicating that basic physics issues were properly addressed, but some differences merit further investigation.
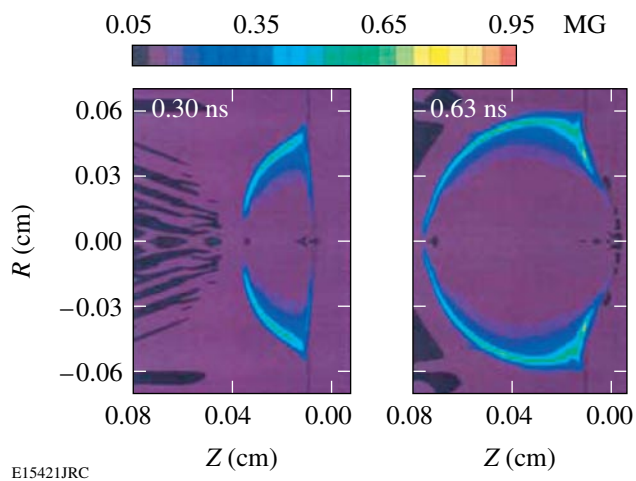
Images acquired with different distributed phase plates used to condition the laser focal spots are contrasted in Fig. 108.34: SG4 for the first row (800 μm) and SG2 for the second row (500 μm). In all cases the laser pulses had similar energy and pulse shape (~250 J, 0.6 ns square), so the laser intensity for the second row was ~2.6 times higher. This resulted in deflection of the central beamlets by nearly a factor of 10 more in the central region for SG2 than for SG4 at ~0.4 ns, but not at ~0.7 ns. This is consistent with our *LASNEX* simulations, which show that a significant *B* field is generated in the central region at earlier times, but moves to the edge of the plasma because of plasma expansion.

(a) 0.00 ns   0.41 ns   0.77 ns
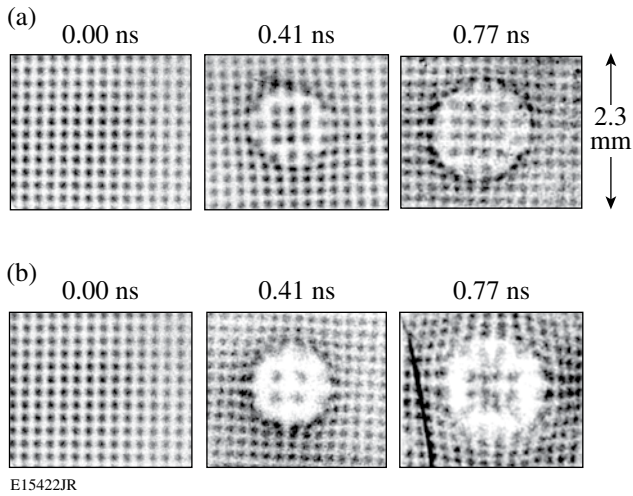
2.3 mm

(b) 0.00 ns   0.41 ns   0.77 ns

E15422JR

Figure 108.34

14.7-MeV-proton radiographs recorded for experiments with a similar interaction laser pulse (~0.6 ns square, ~250 J) but different phase plates: (a) SG4 and (b) SG2. The smaller diameter of the SG2 beam resulted in an intensity ~2.6 times higher than SG4, causing greatly increased image distortion.

The images shown in Fig. 108.35 show a consequence of using no phase plate for the interaction beam. Both images were recorded around 0.3 ns and utilized similar interaction beam diameters, pulse shapes, and laser energy. Compared to the image recorded with phase plate (a), the image recorded without (b) shows a more-chaotic pattern, implying a B field with medium-scale structure (at ~20% to 30% of the bubble size). This observation is consistent with theoretical expectations. An unconditioned OMEGA laser beam has nonuniformities at scales of ~40 μm. This can lead to medium-scale, random
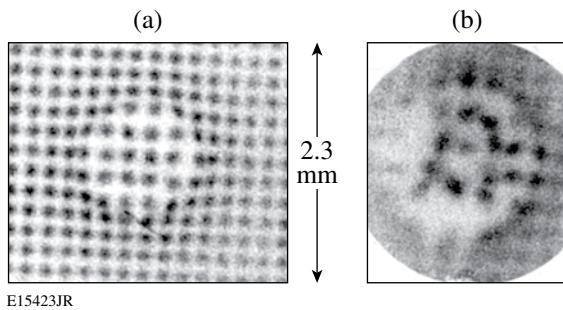

(a)   (b)

2.3 mm

E15423JR

Figure 108.35

Effects of phase plates on the B-field structure are demonstrated by 14.7-MeV proton radiographs made by using interaction beams (a) with and (b) without phase plates under conditions otherwise similar. [Image (b) is from an earlier experiment in which the field of view was smaller and the outer (gray) part of the imaged area was covered by a 70-μm mylar washer.] Chaotic structure is clearly seen in image (b).

plasma structures, in particular those associated with very localized regions of strong $\nabla n_e \times \nabla T_e$, including the resonance absorptions at local oblique incidence, filaments, laser hot spots, and instabilities.[1–5] When phase plates are used, they convert the medium-scale laser nonuniformities to a smaller scale of ~2 μm (the speckle size). Short-wavelength plasma structures are more easily smoothed by thermal transport than medium-wavelength structures, so plasmas are more uniform when phase plates are deployed.

Side-on measured (a) and simulated (b) images are shown in Fig. 108.36 for the same shot that generated the center image shown in Fig. 108.34(b). The displacements of the beamlets away from the foil represent the effect of the electric field generated by $\nabla P/n_e$. The size of the apparent beamlet displacement ($\xi \approx 60$ μm) is used to estimate the E-field strength $\left(E \propto \xi E_p L_\perp^{-1} \right)$; by assuming that the field operates over a scale length $L_\perp$ comparable to the radius of the plasma bubble, $E \approx 1.5 \times 10^8$ V/m was deduced. The magnitude of the beamlet displacement in the experiment is very similar to what is seen in the simulation.
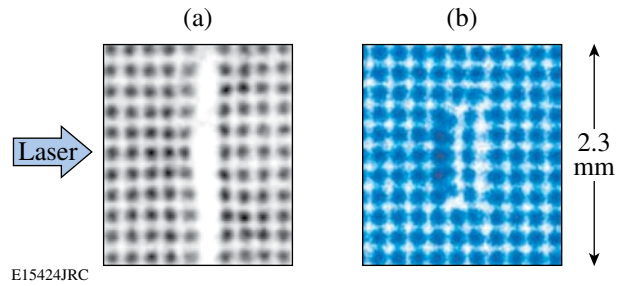

(a)   (b)

Laser

2.3 mm

E15424JRC

Figure 108.36

(a) Data and (b) simulation for the side-on images. The distortion in the center column of (a) resulted from the E field. The large separation between the two center columns of beamlets in (a) is due to attenuation by the CH foil, which is 50 μm thick but 3 mm long in the direction parallel to the proton trajectories. This effect is not seen in (b) because proton–foil interactions were not modeled in the *LSP* simulation. The magnitude of the beamlet displacement in the experiment is very similar to what is seen in the simulation.

In summary, we studied electromagnetic fields generated by the interaction with plasmas of long-pulse, low-intensity laser beams that are particularly relevant to inertial confinement fusion experiments. The field strengths have been measured using novel monoenergetic proton radiography methods. High-resolution, time-gated radiography images of a plastic foil driven by a 10^{14}-W/cm^2 laser implied B fields of ~0.5 MG and E fields of ~1.5×10^8 V/m. The experiments also demonstrated the smoothing effects of laser phase plates by showing that they substantially reduce medium-scale chaotic field structure.

Overall, there was good agreement between experiment and *LASNEX + LSP* simulations, as demonstrated here for the first time, although there exist intriguing differences that merit further investigation. In addition, experiments and simulations, soon to be conducted, will carefully study late times in the evolution of the field structure and probe structures for which the 2-D symmetry implicit in the *LASNEX + LSP* simulations will be broken.

ACKNOWLEDGMENT

REFERENCES

1. S. Eliezer, *The Interaction of High-Power Lasers with Plasmas* (Institute of Physics Publishing, Bristol, England, 2002).

2. L. Spitzer, *Physics of Fully Ionized Gases*, 2nd rev. ed., Interscience Tracts on Physics and Astronomy (Interscience, New York, 1962).

3. S. I. Braginskii, in *Reviews of Plasma Physics*, edited by Acad. M. A. Leontovich (Consultants Bureau, New York, 1965), Vol. 1, p. 205.

4. J. A. Stamper *et al.*, Phys. Rev. Lett. **26**, 1012 (1971); D. G. Colombant and N. K. Winsor, Phys. Rev. Lett. **38**, 697 (1977).

5. M. G. Haines, Phys. Rev. Lett. **78**, 254 (1997).

6. S. H. Glenzer *et al.*, Phys. Rev. Lett. **87**, 045002 (2001).

7. P. Amendt *et al.*, Bull. Am. Phys. Soc. **49**, 26 (2004).

8. R. P. J. Town *et al.*, Bull. Am. Phys. Soc. **50**, 123 (2005).

9. M. A. Yates *et al.*, Phys. Rev. Lett. **49**, 1702 (1982).

10. M. Borghesi *et al.*, Phys. Rev. Lett. **81**, 112 (1998).

11. U. Wagner *et al.*, Phys. Rev. E **70**, 026401 (2004).

12. A. J. Mackinnon, P. K. Patel, R. P. Town, M. J. Edwards, T. Phillips, S. C. Lerner, D. W. Price, D. Hicks, M. H. Key, S. Hatchett, S. C. Wilks, M. Borghesi, L. Romagnani, S. Kar, T. Toncian, G. Pretzler, O. Willi, M. Koenig, E. Martinolli, S. Lepape, A. Benuzzi-Mounaix, P. Audebert, J. C. Gauthier, J. King, R. Snavely, R. R. Freeman, and T. Boehly, Rev. Sci. Instrum. **75**, 3531 (2004).

13. L. Romagnani *et al.*, Phys. Rev. Lett. **95**, 195001 (2005).

14. C. K. Li, F. H. Séguin, J. A. Frenje, J. R. Rygg, R. D. Petrasso, R. P. J. Town, P. A. Amendt, S. P. Hatchett, O. L. Landen, A. J. Mackinnon, P. K. Patel, V. Smalyuk, J. P. Knauer, T. C. Sangster, and C. Stoeckl, Rev. Sci. Instrum. **77**, 10E725 (2006).

15. F. H. Séguin, J. A. Frenje, C. K. Li, D. G. Hicks, S. Kurebayashi, J. R. Rygg, B.-E. Schwartz, R. D. Petrasso, S. Roberts, J. M. Soures, D. D. Meyerhofer, T. C. Sangster, J. P. Knauer, C. Sorce, V. Yu. Glebov, C. Stoeckl, T. W. Phillips, R. J. Leeper, K. Fletcher, and S. Padalino, Rev. Sci. Instrum. **74**, 975 (2003).

16. C. K. Li, D. G. Hicks, F. H. Séguin, J. A. Frenje, R. D. Petrasso, J. M. Soures, P. B. Radha, V. Yu. Glebov, C. Stoeckl, D. R. Harding, J. P. Knauer, R. L. Kremens, F. J. Marshall, D. D. Meyerhofer, S. Skupsky, S. Roberts, C. Sorce, T. C. Sangster, T. W. Phillips, M. D. Cable, and R. J. Leeper, Phys. Plasmas **7**, 2578 (2000).

17. F. H. Séguin, J. L. DeCiantis, J. A. Frenje, S. Kurebayashi, C. K. Li, J. R. Rygg, C. Chen, V. Berube, B. E. Schwartz, R. D. Petrasso, V. A. Smalyuk, F. J. Marshall, J. P. Knauer, J. A. Delettrez, P. W. McKenty, D. D. Meyerhofer, S. Roberts, T. C. Sangster, K. Mikaelian, and H. S. Park, Rev. Sci. Instrum. **75**, 3520 (2004).

18. J. A. Frenje, C. K. Li, F. H. Séguin, J. Deciantis, S. Kurebayashi, J. R. Rygg, R. D. Petrasso, J. Delettrez, V. Yu. Glebov, C. Stoeckl, F. J. Marshall, D. D. Meyerhofer, T. C. Sangster, V. A. Smalyuk, and J. M. Soures, Phys. Plasmas **11**, 2798 (2004).

19. Y. Lin, T. J. Kessler, and G. N. Lawrence, Opt. Lett. **20**, 764 (1995).

20. G. B. Zimmerman and W. L. Kruer, Comments Plasma Phys. Control. Fusion **2**, 51 (1975).

21. P. D. Nielsen and G. B. Zimmerman, Lawrence Livermore National Laboratory, Livermore, CA, UCRL-53123 (1981).

22. D. R. Welch *et al.*, Nucl. Instrum. Methods Phys. Res. A **464**, 134 (2001).

23. In addition, *E* fields can be eliminated as a cause of deflections in face-on images by utilizing, in part, the monoenergetic character of the protons to show that, on the picosecond timescale, electrons would short out the *E* fields that would be required to create the circular patterns.

Evaluation of Cleaning Methods for Multilayer Diffraction Gratings

Introduction

Multilayer dielectric (MLD) diffraction gratings are essential components for the OMEGA EP short-pulse, high-energy laser system, so they must have both high optical-diffraction efficiency and high laser-damage threshold. The cleanliness of optical surfaces intended to be deployed in high-peak-power laser systems is of paramount importance, and the fabrication of these MLD gratings involves processes that utilize a wide variety of both organic materials (photoresists, photoresist solvents, and photoresist developers) and inorganic materials (metals and oxides of various cationic elements) that may remain behind either on the surfaces or in the grooves of the MLD structure after processing. Because a substantial number of these materials can have significant optical absorbance, the incomplete removal of these residues puts the MLD gratings at an increased risk of experiencing catastrophic laser-induced damage. Although there exists a certain amount of anecdotal and empirical evidence as to the effectiveness of certain wet-chemical cleaning processes, which appear to be effective in removing trace residues from grating manufacturing, there does not exist to date a truly systematic study that strives to relate the chemical composition of contaminants introduced during the fabrication process of "structured" optical components (such as MLD gratings) with laser-induced damage. To this end, we have investigated the effectiveness of a number of wet-chemical cleaning processes currently used by the semiconductor industry for cleaning LLE-fabricated MLD gratings. The goal of this investigation was to identify a process or processes that were sufficiently aggressive in the removal of residual processing contaminants but not so aggressive as to produce physical/chemical damage to the MLD grating structure that would reduce its high diffraction efficiency.

The following chemical processes were evaluated for MLD cleaning:

Piranha Process: Piranha solution is a mixture of a strong acid (sulphuric acid, H_2SO_4) and a strong oxidizing agent (hydrogen peroxide, H_2O_2), which produces an extremely energetic solution. This composition is one of the most commonly used cleaning processes for the removal of organics (i.e., residual resist) from a surface and is usually used at a high temperature.[1,2] Although Piranha solution is highly effective in removing organic contamination, it does not remove all inorganic contaminants. Piranha solution must be prepared immediately before use, has a very limited shelf life, and cannot be stored in normal closed containers due to an explosive pressure buildup caused by the gradual loss of hydrogen peroxide gas.

Piranha + SC-1 Process: The cleaning method that is commonly used to remove inorganic contamination after Piranha clean (described above) is SC-1 (Standard Clean 1) coupled with megasonics (high-frequency ultrasonic energy).[1,3] The SC-1 solution of ammonia hydroxide, hydrogen peroxide, and DI water is also cable of removing additional organic contaminants. The megasonics aid in removing the inorganic contamination. The cavitation force generated by the megasonic frequency lifts off the contamination and also keeps these particles from re-adhering to the surface.

Hydrozone Process: Hydrozone+,[4] developed as a replacement for Piranha clean, uses ozone gas dissolved in DI water. An aqueous solution at elevated temperatures is sprayed across a surface while dry ozone gas is admitted into the cleaning chamber. The ozone diffuses through the thin boundary layer of water, in which the water hydrolyzes the organic bonds, making them susceptible to attack by O_3. The elevated water temperature maximizes the reaction rate. The reaction by-products (CO_2 and H_2O) and resist fragments are carried away in the boundary layer of water.

EKC-265[5] and Rezi-28[6] Process: These two semi-aqueous organic mixtures have been formulated as ready-to-use solutions. They contain chemistries that are effective in removing residual photoresist and post-etch and ash residues. These residue removers are formulated to be used at lower operating temperatures than standard Piranha cleans.

Nanostrip Process: Nanostrip[7] is a ready-to-use stabilized formulation of sulphuric acid (H_2SO_4) and hydrogen peroxide

(H_2O_2) compounds. This formulation was designed to remove photoresist and other organic materials at ambient temperatures and can be stored at room temperature indefinitely in closed containers without the risk of an explosive pressure buildup.

Experimental Setup

Table 108.V lists the various cleaning-process parameters evaluated for this study. Each of the processes in Table 108.V was evaluated using 100-mm-diam MLD gratings fabricated at LLE.

The grating-fabrication-process steps include (1) photoresist coated using a positive-tone resist; (2) exposure of the photoresist at 365 nm using a holographic process; (3) photoresist development; (4) reactive ion-beam etching (RIBE) of the grating pattern; (5) O_2 ion-etch clean utilizing LLE-standard-process parameters; and (6) a final wet-cleaning step. Each grating was evaluated for diffraction efficiency and laser-damage threshold both before and after the final cleaning step. All cleaned gratings were further evaluated by scanning electron microscopy (SEM), with time-of-flight secondary ion-mass spectrometry (ToF-SIMS) analysis performed on a select group of four samples.

Results

1. Diffraction Efficiency

Each cleaned MLD grating was tested for diffraction efficiency and laser-damage threshold. Pre- and post-clean diffraction efficiencies were measured across the grating using s-polarized light at 1054 nm with an incident beam angle of 61°

(diffracted beam angle of 72°). Since there is a large variation in pre-clean diffraction efficiency, the cleaning process should increase the efficiency to our specification, but it should not decrease it to a level below our specification. Figure 108.37 shows the pre- and post-clean diffraction efficiencies for the various chemistries used. As can be observed, all of the cleaning processes meet our specification of >97% except the Piranha + SC-1. Based on SEM evidence shown later, we believe that the base SC-1 chemistry had a negative effect on the grating. The ECK-265 and Piranha-cleaned samples had the highest post-clean diffraction efficiency.
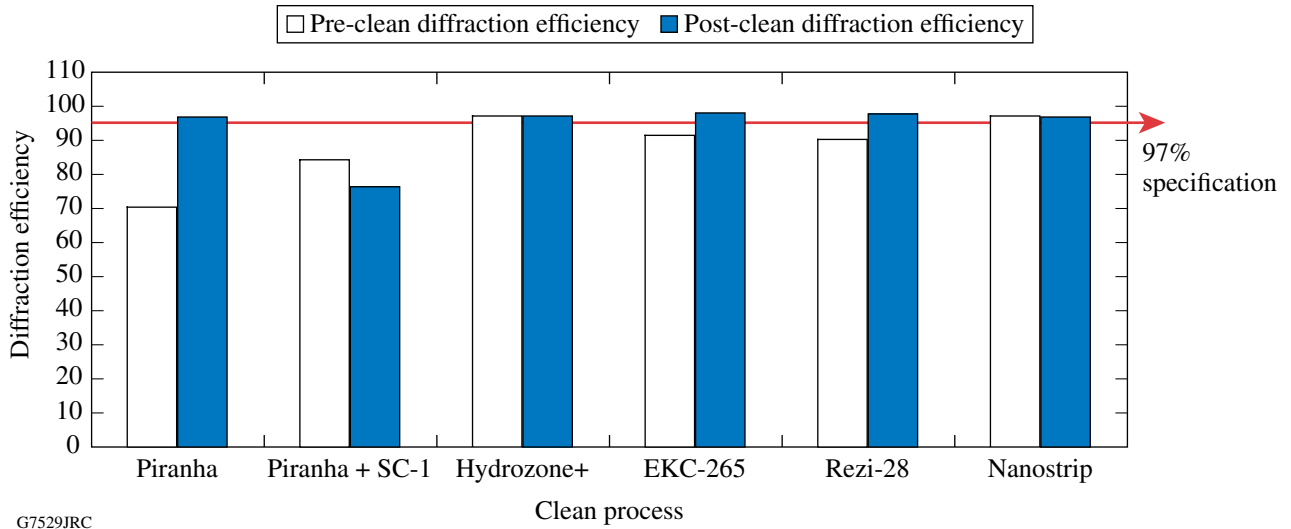
2. Laser-Damage Threshold

Laser-damage testing was conducted using 10-ps-pulsed, s-polarized light at 1053 nm with an incident beam angle of 61° (diffracted beam of 72°). The LLE specification for the damage threshold of our MLD gratings is 2.7 J/cm^2 at 10-ps pulse length. Figure 108.38 shows the damage-threshold values that were measured for the different cleaning processes.

The damage-threshold results indicate that only the Piranha, Nanostrip, and EKC-265 cleaning processes are capable of producing clean gratings that achieve the LLE specification.

The Nanostrip process was evaluated at different immersion times to see how this affected the laser-damage threshold. The laser-damage threshold was found to decrease with increased immersion time. This decrease in damage threshold could be due to re-deposition of organics on the surface since this work was performed in a static (un-agitated) lab-scale bath. Similarly,

Table 108.V: Process chemistries and conditions.

Process	Chemistry	Time	Temperature	Methods
Piranha	$H_2SO_4 + H_2O_2$ (various ratios)	30 min 60 min 4 h 8 h	– 60°C 90°C 110°C	Overflow bath, lab-scale beakers
Piranha + SC-1	{$H_2SO_4 + H_2O_2$ (4:1)} + {$NH_4OH + H_2O_2 + DI$ (1:1:10)}	30-min Piranha + 10-min SC-1	90°C Piranha + 70°C SC-1	Overflow bath with 3-MHz megasonics
Hydrozone + (Semitool)	$Di + O_3 + NH_4OH$	10 min 25 min	90°C –	Single plate spray
EKC-265 (EKC Tech)	Semi-aqueous organic mixture	30 min	70°C	Overflow bath with 3-MHz megasonics
Rezi-28 (J. T. Baker)	80% aqueous base	10 min	40°C	Overflow bath
Nanostrip (Cyantek)	Stabilized formulation of $H_2SO_4 + H_2O_2$	4 h 8 h 24 h	60°C – –	Lab-scale beakers

Figure 108.37
Pre- and post-clean diffraction efficiency.
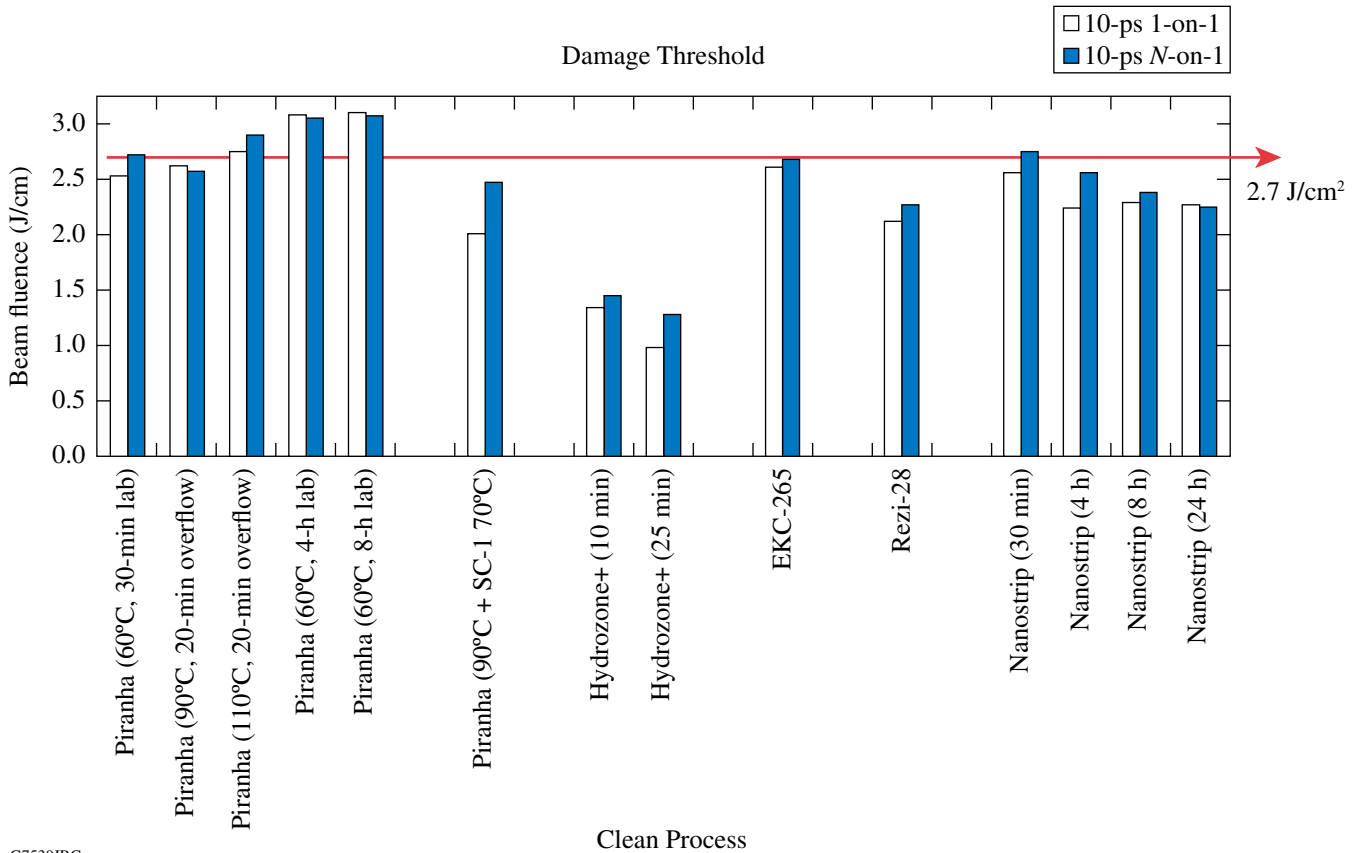
Figure 108.38
Post-clean damage threshold.

the Piranha process was evaluated at different times and temperatures. For this cleaning process, the laser-damage threshold increased as the temperature increased from 90°C and 110°C when processed in a recirculating overflow bath. Increasing the immersion time (in a static lab-scale bath) at the lower 60°C temperature also resulted in an increase in the laser-damage threshold. Additional Designs of Experiment studies are being run to fully understand reaction-rate issues of Piranha clean.

3. SEM Analysis

Scanning electron microscopy (SEM) images were collected and analyzed for each of the MLD gratings that were cleaned in this study. The SEM images of the EKC-265–cleaned and Piranha-cleaned gratings indicate there was no visual residual contamination within the grating trenches. The SEM images, along with the associated diffraction efficiency and laser-damage threshold data for these gratings, are shown in Fig. 108.39.

The SEM images along with the associated diffraction efficiency and laser-damage threshold data for the Hydrozone+, Rezi-28, and Piranha + SC-1–cleaned gratings are shown in Fig. 108.40. The Hydrozone+, Rezi-28, and Piranha + SC-1–cleaned gratings had lower laser-damage threshold values than the EKC-275– and Piranha-cleaned gratings. The Piranha + SC-1 cleaning process damaged the diffraction grating. We believe the SC-1 portion of this cleaning process, which uses a concentrated basic ammonium hydroxide solution, attacked the top amorphous SiO_2 grating layer, which caused it to decompose. Additional work is required to fully understand the failure mechanism. The Rezi-28 clean was not effective in removing the bulk photoresist from the gratings, while the Hydrozone+ clean left visual contamination within the grating trenches.

ToF-SIMS Analysis

Time-of-flight secondary ion mass spectrometry (ToF-SIMS) was performed on four different LLE diffraction-grating samples. The four samples analyzed were (1) photoresist-coated MLD (pre-clean process), (2) MLD-etched and O_2 ion-etch clean (pre-clean process), (3) Piranha-cleaned MLD, and (4) Hydrozone+-cleaned MLD.

The ToF-SIMS analysis was performed at Surface Science Western, University of Western Ontario (London, Ontario, Canada). The instrument used was an ION-TOF (GmbH), ToF-SIMS IV. A 25-keV, pulsed Bi_3^+ cluster, primary ion beam with a target current of 0.6 pA and a beam diameter of ~1.5 μm was rastered over a 500×500-μm^2 area on each sample. The mass range used was 10 to 1000 amu. Due to the insulating nature of the samples, a pulsed-electron flood gun was employed to neutralize charging. The analysis is sensitive to the outer one to three monolayers of the sample surface under static conditions (total primary ion dose $<10^{13}$ ions/cm^2). This technique is
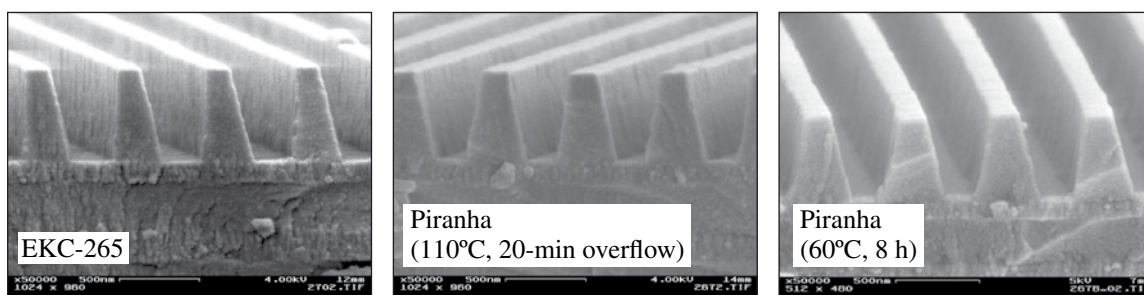
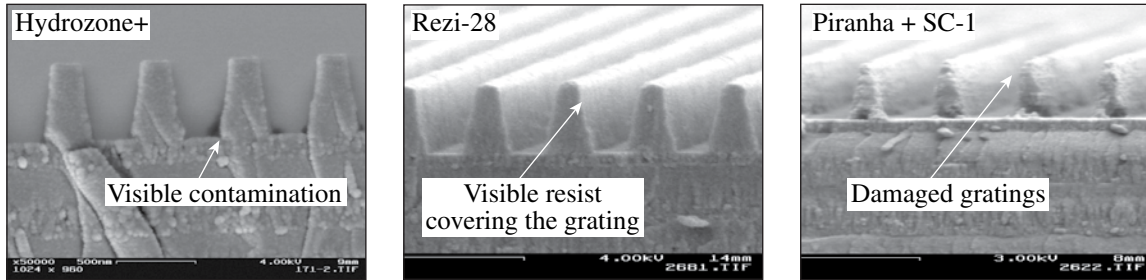| Process	Pre-clean diffraction efficiency	Post-clean diffraction efficiency	10-ps 1-on-1 (J/cm^2)	10-ps N-on-1 (J/cm^2)
EKC-265	91.5	98.1	2.61	2.68
Piranha (110°C, 20-min overflow)	70.5	96.9	2.75	2.9
Piranha (60°C, 8 h)	Not measured	Not measured	3.1	3.07

G7436JR

Figure 108.39
EKC-265 and Piranha SEM analysis with associated efficiency and damage threshold.

not absolutely quantitative; however, using peak area ratios and related normalization methods for similar substrates, meaningful and sensitive relative comparisons can be made.[8]

In order to have a numerical comparison between the samples, selected positive- and negative-ion species were chosen.

Corresponding peaks were extracted and normalized to 100% (total peak areas). The normalized species are summarized in Figs. 108.41–108.43. Figure 108.41 lists species that are related to the photoresist (residual organics). This graph indicates that resist-related species remained on the surface after cleaning. The Piranha-cleaned sample had the lowest levels of resist-

Process	Pre-clean diffraction efficiency	Post-clean diffraction efficiency	10-ps 1-on-1 (J/cm^2)	10-ps N-on-1 (J/cm^2)
Hydrozone+ (10 min)	97.1	97.2	1.34	1.45
Rezi-28	90.2	97.8	2.12	2.27
Piranha 110°C + SC-1	84.2	76.4	2.01	2.47

G7435JR

Figure 108.40
Hydrozone+, Rezi-28, and Piranha + SC-1 SEM images.
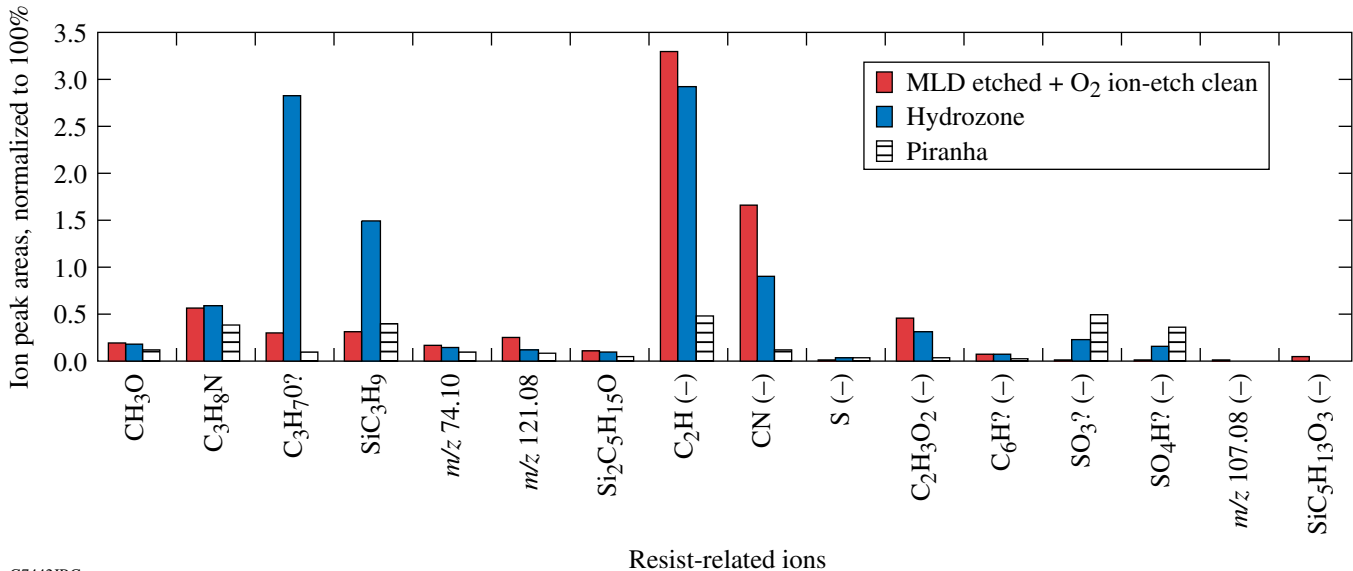
G7442JRC

Figure 108.41
Resist-related species. Note: Not all mass-to-charge (*m/z*) ions are able to be fully characterized. The resist sample is not shown since the level of resist-related ions approaches 100%.

related species remaining after cleaning, but there are still residual resist species that need to be removed.

The species predominantly associated with the SiO_2 grating are indicated in Fig. 108.42. Samples that have high Si-related ion peaks indicate that the surface is relatively clean since the top grating surface is SiO_2. The lack of Si-related ion peaks indicates that there were other contaminants on the surface. As shown, the Piranha and Hydrozone+ clean samples had a high signal for Si and Si_xO_y species, indicating that there is less contamination. The MLD O_2 ion-etch clean sample does not show any signal for Si or Si_xO_y species. This indicates that there was a layer of other contamination on the SiO_2 surface. The species associated with the MLD O_2 ion-etch clean sample are mainly metals, which

could be originating from contamination within the etch and ash chambers (shown in Fig. 108.43). Most of these metals, however, were removed during the cleaning process.

Time-of-flight secondary ion mass spectrometry (ToF-SIMS), "shallow"-depth-profile (few tens of nanometers into the surface) scans were taken to understand the contamination of the Piranha sample. To acquire positive and negative shallow-depth profiles, a second 3-keV Cs^+ sputter ion beam was used, with a raster area of $500 \times 500~\mu m^2$ and a target current of 12 nAS. The Bi_3^+ analysis area is centered within the sputter crater, with a raster size of $200 \times 200~\mu m^2$. Using a raster size smaller than the sputter-crater size allows one to avoid edge effects during the depth profiling. By alternating the Bi_3^+ analysis and the Cs^+ sputter beams and
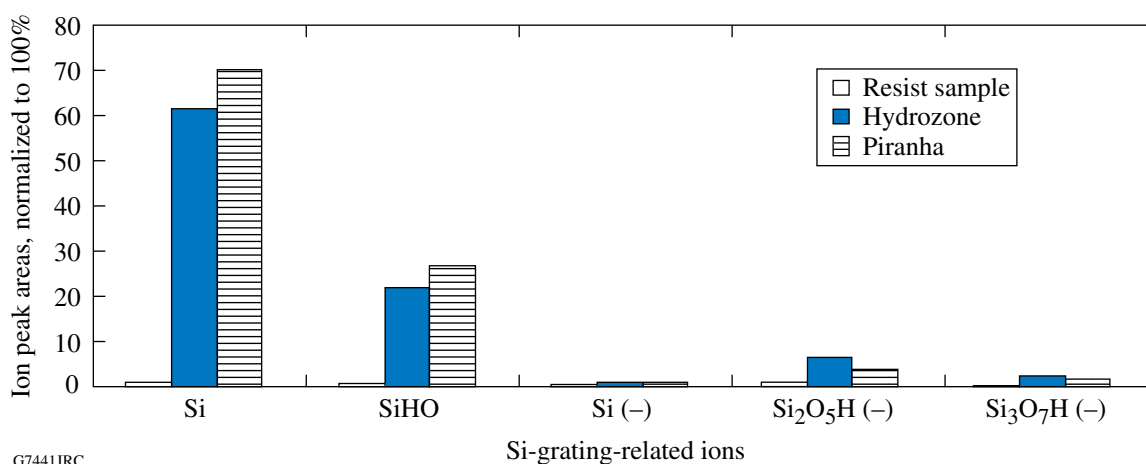

G7441JRC

Figure 108.42
Si-related species. MLD etched + O_2 ion-etch sample does not have a Si-related signal due to other contamination covering the surface.
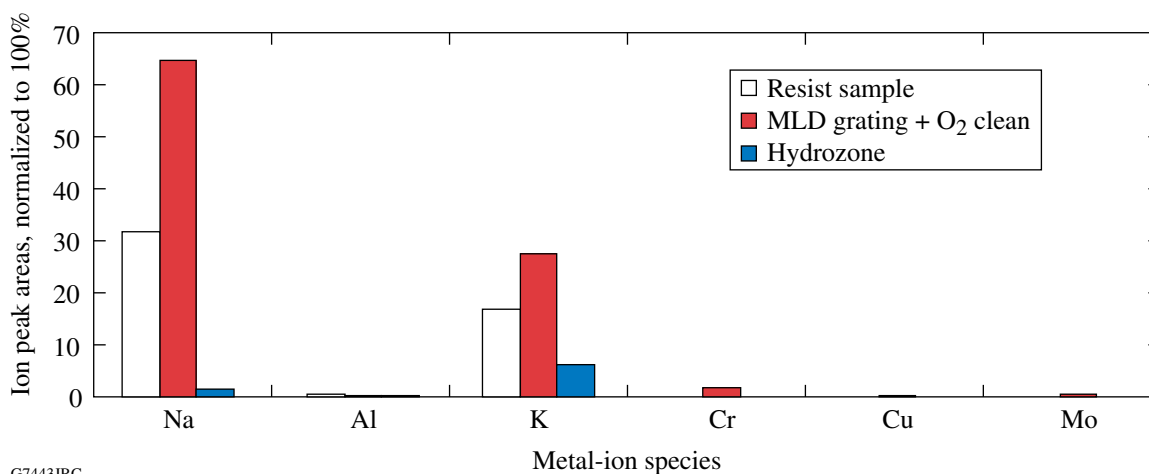

G7443JRC

Figure 108.43
Metal-related species. Piranha-clean (not shown) process removes most metals.

inserting an electron-flood-gun pulse between for charge neutralization, a depth profile into the surface is acquired.[9]

Figure 108.44 plots the raw intensity of the positive ions detected versus the sputter time for the Piranha-cleaned sample. This sample yields various ions with Si^+ being the dominant one. Directly at the grating surface there was an abundance of Si^+ (silicon ion), $SiOH^+$ (silicon hydroxide ion), K^+ (potassium ion), O^+ (oxygen ion), Na^+ (sodium ion), Cr^+ (chromium ion), Fe^+ (iron ion), and Al^+ (aluminum ion). As the analysis probed deeper into the SiO_2 surface, additional major ions detected were Si^+, K^+, $SiOH^+$, O^+, Na^+, Fe^+, and Al^+. The Si^+ and $SiOH^+$ ions were from the SiO_2 grating, as one would expect. The oxygen originated from the etch process and was being "implanted" into the SiO_2 grating surface during the reactive ion-beam etch (RIBE). The metals Cr^+, Fe^+, and Al^+ originated from the etch chamber and became implanted into the SiO_2 grating surface. The potassium and sodium ions were surmised to come from multiple contamination sources. Some of the possible sources of this contamination could have been the rinse water, developer, materials used during cleaning (beakers), and general handling. Additional tests need to be done to better understand this contamination.

The concentration of negative-ion species detected versus sputter time is plotted in Fig. 108.45. The major ions detected were O^- (oxygen ion), SiO_2^- (silicon oxide), F^- (fluorine ion), Si^- (silicon ion), SO_3^- (sulfate ion), Cl^- (chlorine ion), CN^- (cyanide ion), C_2H^- (carbon ion), and C^- (carbon ion). The oxygen, fluorine, chorine, and carbon ions were implanted from the etch process and chamber. The silicon-related ions originated from the silicon oxide grating, while the sulfate ion originated from the sulfuric acid–cleaning process.

Conclusions

Using 100-mm-diam MLD gratings fabricated at LLE, we evaluated different cleaning methods designed to optimize both optical diffraction efficiency and laser-damage threshold of these gratings for the OMEGA EP Laser System. Pre- and post-clean diffraction efficiency and laser-damage threshold were measured for each of the samples. Scanning electron microscopy (SEM) images were collected and analyzed to understand if any visual surface contamination existed after cleaning. Additionally, a baseline time-of-flight secondary ion-mass spectrometry (ToF-SIMS) and shallow-depth profile analysis was performed to understand the type of contamination remaining after the different process steps.

The diffraction efficiency, laser-damage threshold, and SEM images all show that the Piranha clean merits further exploration. The MLD gratings cleaned by the Piranha processes had the highest diffraction efficiency and laser-damage-threshold
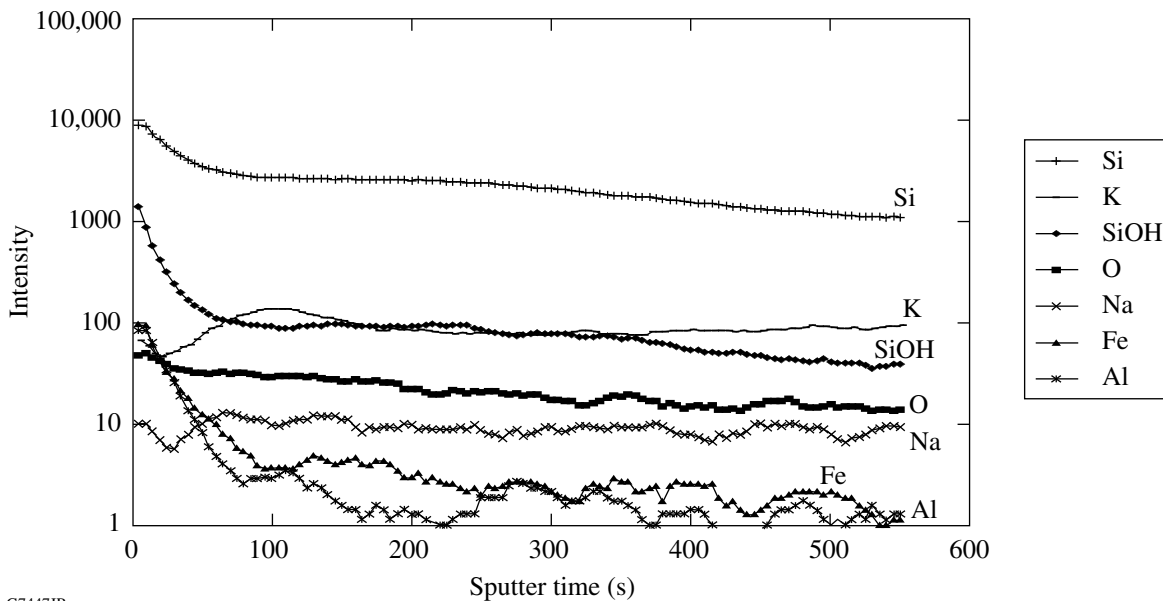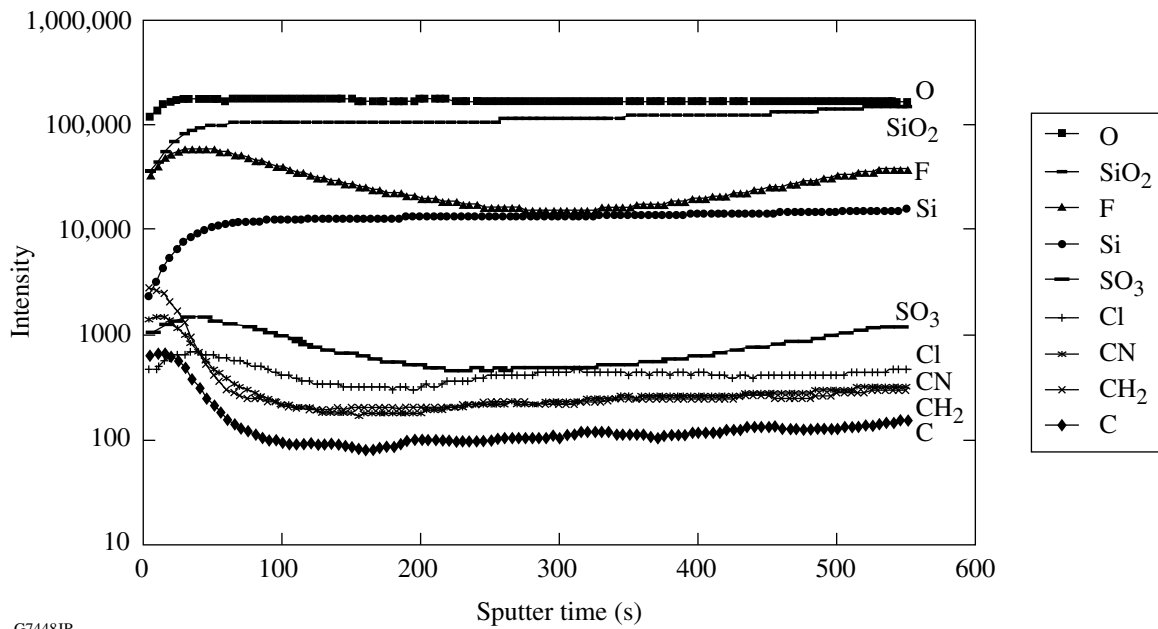

G7447JR

Figure 108.44
Piranha-clean positive-ion depth profile.

Figure 108.45
Piranha-clean negative-ion depth profile.

values. The SEM images also validated these results by showing no visual contamination after cleaning.

ToF-SIMS analysis was performed on four types of samples from the LLE grating project to acquire a baseline for surface residual contamination. The encouraging results show that the cleaning process can remove a large portion of the photoresist (organic) contamination even without optimization of cleaning-process variables. It was further found that there is a monolayer of contamination (mostly metal ions) after etch and O_2 ion-etch clean processing. The shallow-depth profile analysis provides an understanding of the contaminants implanted in the grating surface, which in turn allows identification of the source of most of the ions detected. Understanding the sources and depth of "implantation" of these ions will assist LLE in developing an optimized grating-cleaning process. Further Design of Experiment studies will be evaluated to understand the interaction of the variables within the cleaning process. LLE will continue to use SEM and ToF-SIMS analysis to characterize the surface after each cleaning test.

ACKNOWLEDGMENT

REFERENCES

1. W. Kern, *Handbook of Semiconductor Wafer Cleaning Technology: Science, Technology, and Applications*, Materials Science and Process Technology Series (Noyes Publications, Park Ridge, NJ, 1993), pp. 3–56.

2. S. Clark, Bold Technologies, Inc., West Jordan, UT 84088, http://www.bold-tech.com/technical/piranha_etch.html (2000).

3. R. S. Ridley, Sr. et al., in *1998 IEEE/SEMI Advanced Semiconductor Manufacturing Conference* (IEEE, Boston, 1998), pp. 235–242.

4. Semitool, Kalispell, MT 59901.

5. EKC265 product sheet, EKC Technology, Inc., Hayward, CA 94545, November 2006, http://www2.dupont.com (6 November 2006).

6. Rezi-28 product sheet, Mallinckrodt Baker, Inc., Phillipsburg, NJ 08865, November 2006, http://www.mallbaker.com (11 November 2006).

7. NANO-STRIP™ product sheet, Cyantek Corporation, Fremont, CA 94539-5652, http://www.cyantek.com (2006).

8. Dr. James Francis, ToF-SIMS Results, Surface Science Western, email reports and private communication (6 April 2006).

9. Dr. James Francis, ToF-SIMS Report, Surface Science Western, email reports and private communication (9 August 2006).

# Design and Analysis of Binary Beam Shapers Using Error Diffusion

Introduction

Controlling the amplitude and phase of light is crucial in many technological applications, such as imaging, lithography, astronomy, and laser physics. In high-power laser systems, there is a need for precise beam shaping. Square beams with super-Gaussian profiles are used to optimize the fill factor of amplifiers. The spatially dependent gain of amplifiers can be, to a large extent, precompensated, i.e., the spatial intensity of the beam to be amplified is shaped before amplification so that regions of higher gain in the amplifier correspond to regions of lower intensities in the input beam. To avoid damage or small-scale self-focusing, local intensity variations should be minimized and intensities kept below damaging intensities; therefore, there is a need for accurate beam-shaping systems with fine controls. While spatial light modulator (SLM) technology[1] is well developed, it is not a perfect fit for these applications, since the damage threshold of most SLM's is lower than the required operating fluences for some applications. Because of saturation in laser amplifiers and nonlinear effects such as those encountered in optical parametric chirped-pulse amplification,[2] precompensation may need to be performed at locations in the system where the fluence is already significant (for example, after a first stage of amplification). Beam shaping has been demonstrated using the modal discrimination of a laser cavity or regenerative amplifier cavity (for example, using intracavity phase masks[3,4]), but no elaborate beam-shaping function has been performed beyond the realization of flat-top beams. Additionally, some degree of complexity is added by the realization of a laser cavity combining amplification and shaping, compared to an architecture where these functions are performed by independent elements that can be optimized separately. A large variety of techniques have been demonstrated to generate a spatially varying transmission, such as photographic plates,[5] mirrors with variable reflectivity,[6] elements with spatially varying birefringence,[7] and elements with spatially varying transmission based on total internal reflection.[8] It is unclear, however, if any of these techniques has the required versatility and reliability.

Historically, the solution for shaping high-energy laser beams has been to propagate the beam in a glass substrate with metal patterns on the input surface, where regions coated with metal block the light while clear regions have a 100% transmission. Super-Gaussian beams can, for example, be generated by serrated tooth apodizers,[9] i.e., apodizers with a high-frequency periodic structure where the duty cycle varies as a function of the distance to the center of the plate, which provides a smooth apodization function after Fourier filtering. These apodizers are appropriate for edge-only shaping, i.e., realizing a smooth transition from the high transmission at the center of the beam to the absence of transmission on the edges. However, they cannot generate more-complex shaping functions. Smooth shaping functions can be generated using a vacuum-deposited layer of a metal such as aluminum.[10] More control can be obtained via binary pixelated arrays of metal pixels, as used on the National Ignition Facility[11] to precompensate for the spatial gain variation of large glass amplifiers.[12]

Figure 108.46 displays two examples of target transmission. In Fig. 108.46(a), the target transmission is a 40th-order super-Gaussian that is used in high-power lasers to optimize the fill factor in large-scale slab amplifiers, while decreasing the detrimental effects of diffraction that would occur with a sharp-edge square beam. The corresponding lineout is plotted in Fig. 108.46(c). In Fig. 108.46(b), the target transmission corresponds to the precompensation of the spatially dependent gain of 58 passes in 40-cm-diam Nd:glass disks, as required for OMEGA EP.[13] The corresponding lineout, plotted in Fig. 108.46(d), demonstrates the required nonsymmetric shape due to the uneven distribution of the orientations of the disks. While the apodizing function of Fig. 108.46(a) can be synthesized with serrated tooth apodizers, this approach does not work for the more-complex function of Fig. 108.46(b). Such precompensation is mandatory for large-scale laser systems.[10]

Gray-scale rendering with black or white features is crucial in printing applications, where it is usually referred to as digital half-toning or spatial dithering.[14] Among many other algorithms,[14] the error diffusion algorithm has been identified as particularly efficient at providing gray-scale images with visually pleasing results.[15] Because of the analogy between image
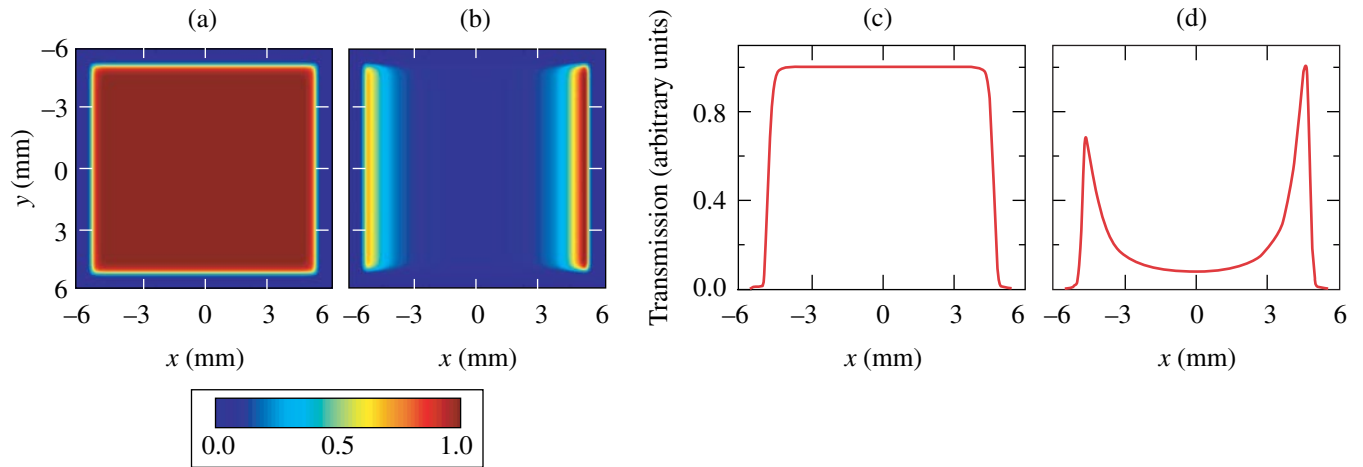
E14561JRC

Figure 108.46
(a) Example of 40th-order super-Gaussian intensity; (b) example of intensity distribution required to precompensate for the spatial gain variation in OMEGA EP; (c) lineout of the intensity of (a) at the center of the beam along the *x* direction; (d) lineout of the intensity of (b) at the center of the beam along the *x* direction.

rendering and transmission shaping, it is of interest to study the performance of error diffusion when designing binary masks leading to continuous beam-shaping functions. The purpose of this article is to provide insight into the potential and limitations of this technique. The principle of error diffusion and its application to the design of pixelated binary masks are presented first. The performance of the obtained masks in terms of beam shaping is then studied in the context of high-power laser systems. Finally, the influence of feature size on the shaping performance is studied analytically and via simulations.

Error Diffusion Principle
1. Shaping of a Coherent Light Source
    It is assumed that a coherent source with constant intensity $I_0 = |E_0|^2$ is incident on a transmission mask, which is relay imaged to the image plane, following Fig. 108.47. A Fourier plane in the imaging system can be used for Fourier filtering. An example of such a system is a two-lens system, with lenses of identical focal length, for which Fourier filtering can be performed with a pinhole at the Fourier plane of the first lens. For the sake of simplicity, we assume an imaging system with magnification equal to 1. The electric field after the binary mask with transmission $s(x,y)$ is $E(x,y) = E_0 \times s(x,y)$, where $s(x,y)$ is either 0 (presence of light-blocking metal) or 1 (no metal) and is pixelated. The electric field at a Fourier plane of the first lens is written as $E_0 \times \tilde{s}(u,v)$, where $\tilde{s}$ is the Fourier transform of s. This field is filtered by a transmission filter p, leading to the field $E_0 \times \tilde{s}(u,v) \times p(u,v)$. The resulting field at an image plane can be written as a convolution $E' = E_0 \times s \otimes \tilde{p}$. Because the

convolution with the Fourier transform of the filter $\tilde{p}$ acts as a local averaging operation on the electric field of light after the shaper, the intensity of the output field at a given point (x,y) is proportional to the square of the average value of s around this point. This is important when designing a beam shaper for a spatially coherent light source because the average transmission of the beam shaper before filtering must be designed to be equal to the square root of the target intensity transmission after filtering. The averaging operation provided by the filter in the far field is the key point in obtaining a smooth continuous intensity from a binary pixelated mask.

2. Design of a Binary Beam Shaper Using Error Diffusion
    Error diffusion[14,16,17] is based on the lexicographical processing of the pixels of the mask, typically from top to bottom and left to right, following the diagrams in Fig. 108.48.
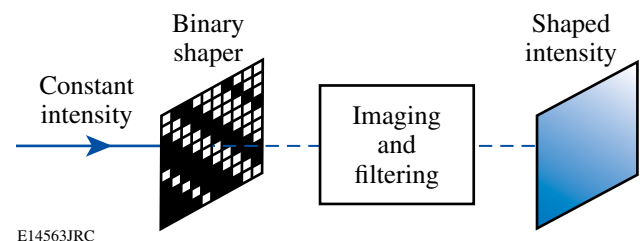
E14563JRC

Figure 108.47
Principle of the generation of a continuous shaped intensity using a binary shaper and Fourier filtering.

(a) Shaper target transmission $t(m,n)$ (b) Shaper binary transmission $s(m,n)$
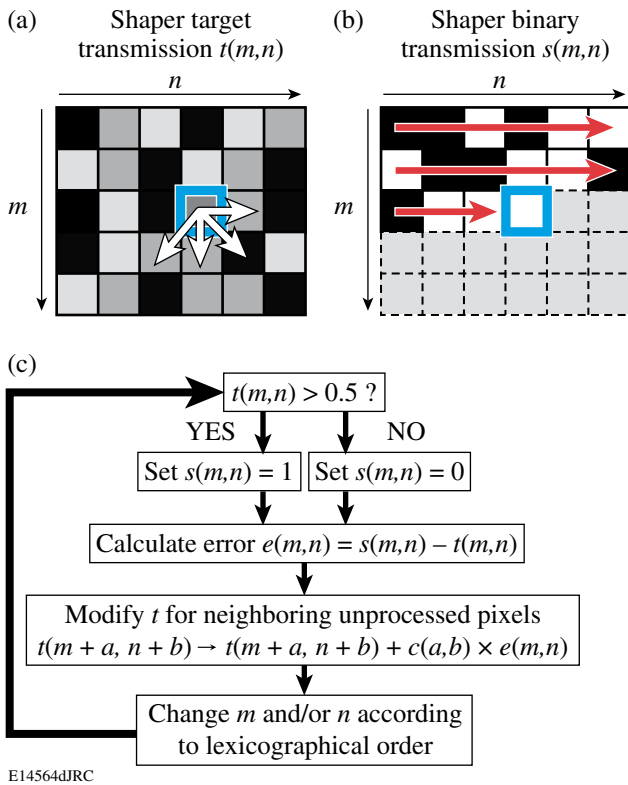
(c)

E14564dJRC

Figure 108.48

Principle of the error diffusion algorithm. (a) Representation of the target shaper transmission $t(m,n)$; (b) representation of the binary shaper transmission $s(m,n)$ being designed; (c) chart describing the design process. The thick squares on (a) and (b) represent the pixel being processed. The horizontal arrows on (b) schematize the lexicographical process over the already processed pixels. The white arrows on (a) represent the error diffusion to adjacent nonprocessed pixels.

A pixelated representation of the target transmission of the shaper, $t(m,n)$, is shown in Fig. 108.48(a), while the binary shaper being designed is shown in Fig. 108.48(b). On the latter, previously processed pixels have a transmission $s(m,n)$ equal to either 0 or 1 and are plotted in black or white, while nonprocessed pixels have been arbitrarily plotted in gray. Since the target transmission takes values in the interval [0,1] while the shaper transmission is either 0 or 1, the choice of the value of each pixel in the binary mask induces a transmission error. In error diffusion, the binary value of the pixel (m,n) is set by the information contained in the target shaper transmission $t(m,n)$, which can be modified by the choices that have been made for the mask binary value $s(m,n)$ for the pixels that have already been processed. Initially, one sets $t(m,n) = \sqrt{I(m,n)}$, where I is the sampled representation of the target intensity of the coherent source. Following the chart in Fig. 108.48(c), the choice of transmission $s(m,n)$ is made by comparing the target shaper

transmission to 0.5. If the target transmission is smaller than 0.5, $s(m,n)$ is set to 0, while, if the transmission is larger than 0.5, $s(m,n)$ is set to 1. The resulting error is "diffused" to pixels that have not yet been processed, usually neighboring pixels, to bias the binary choice for these pixels and locally compensate the transmission error. This is done by adding a fraction of the error $e(m,n) = s(m,n) - t(m,n)$ to the target transmission for these pixels, which is symbolized in Fig. 108.48(a) by white arrows pointing to these pixels. The target transmission $t(m + a, n + b)$ is then replaced by $t(m + a, n + b) + c(a,b) \times e(m,n)$ for the chosen set of integers a and b. In the initial developments of error diffusion by Floyd and Steinberg,[16] only the four neighboring pixels at coordinates $(m + 1, n - 1)$, $(m + 1, n)$, $(m + 1, n + 1)$, and $(m, n + 1)$ are used in the diffusion process (four-weights error diffusion). The results presented in this article have been obtained with such implementation, as the gain of performance when diffusing the error to a large number of neighboring pixels does not seem significant. The function c takes for value $c(1,-1) = -3/16$, $c(1,0) = -5/16$, $c(1,1) = -1/16$, and $c(0,1) = -7/16$. The algorithm then proceeds with the next pixel, following the lexicographical order.

Properties of Binary Shapers Generated with Error Diffusion

1. Error Functions for Beam-Shaping Performance

Two functions have been used to quantify beam-shaping performance. A normalized version of the rms error between the target shaped intensity and the obtained shaped intensity after filtering is

$$\varepsilon_{\text{rms}} = \sqrt{\iint_{S} \left[T_{\text{obtained}}(x,y) \big/ T_{\text{target}}(x,y) - 1 \right]^2 dx\,dy}, \quad (1)$$

where the double integral is calculated over the region S, where the target intensity is higher than a given threshold to ensure that only relevant values are kept. The normalization ensures that the calculated error remains the same after multiplication of the target and obtained intensities by a spatially varying function. This ensures that this rms error is also a proper description of the shaping performance after amplification of the shaped beam.

Another error function of interest when dealing with shaping elements for laser applications describes the presence of local high values of the intensity because of the potential damage to optics and self-focusing,

$$\varepsilon_{\text{peak}} = \max_{S} \left| \frac{T_{\text{obtained}}(x,y)}{T_{\text{target}}(x,y)} - 1 \right|, \quad (2)$$

where the maximum is calculated over a region of interest (typically, the region where the beam is amplified to signifi-

cant values). This error function quantifies the magnitude of hot spots in the beam. While these two error functions are, in general, not correlated, it was found that they had similar behaviors when varying the pixel size or the parameters of the far-field filtering operation, and we therefore plot only the rms error, but quote the peak error in relevant cases.

2. Comparison of the Error Diffusion Algorithm
   with the Random Dither Algorithm

A simple random dither algorithm is used to emphasize the properties of the error diffusion algorithm. The random dither algorithm is one of the simplest algorithms that can be used to design binary shaping elements. It is also known as white-noise dithering because of the spectral content of the generated images.[14] While this technique has shortcomings, its simplicity makes it an ideal choice to highlight the properties and performance of the error diffusion algorithm. For the random dither algorithm, the binary transmission of each pixel is chosen by a random draw between 0 and 1. If the drawn number is smaller than the target transmission, the transmission of the pixel is set to 1, while if the drawn number is higher than the target transmission, the transmission of the pixel is set to 0. Properties of random draws ensure that this algorithm properly reproduces gray levels on average. One should note that there is no error feedback in such an algorithm.

3. Properties of the Error Diffusion Algorithm

Pixelated binary masks generated with error diffusion are highly ordered structures. Figure 108.49 displays pixelated binary distributions generated by error diffusion for target transmissions equal to 5%, 25%, and 75%. It was found that the error diffusion algorithm can reproduce gray levels very accurately. These close-ups are compared to close-ups of masks generated by the random dither algorithm to generate the same target transmission. The latter show no correlation between the presence of pixels at various locations in the mask.

To understand the binarization noise, the error diffusion and random dither algorithm were used to generate a shaping function corresponding to Fig. 108.46(b), using 10-μm pixels. The corresponding binary shaper generated by error diffusion is plotted in Fig. 108.50(a), and close-ups of the binary pixel distributions at the center and at the upper right corner are displayed in Figs. 108.50(b) and 108.50(c). A lineout of the shaped intensity plotted in Fig. 108.50(d) demonstrates the proper realization of the transmission of the shaper, including the proper transmission at the center of the beam and the high-frequency content on the edges of the beam, owing to the high resolution and proper rendition of gray levels when using error diffusion.
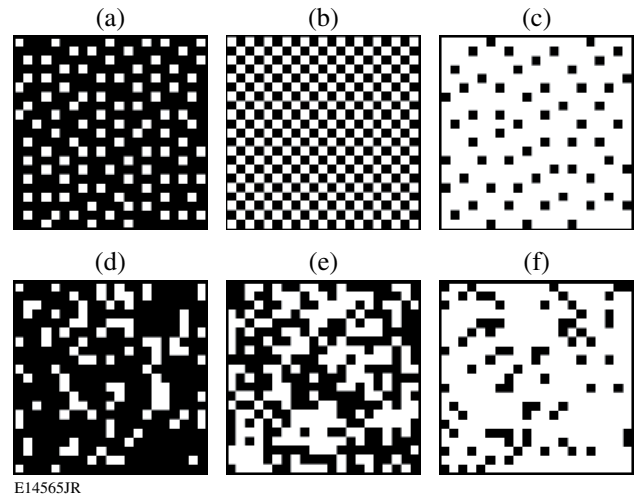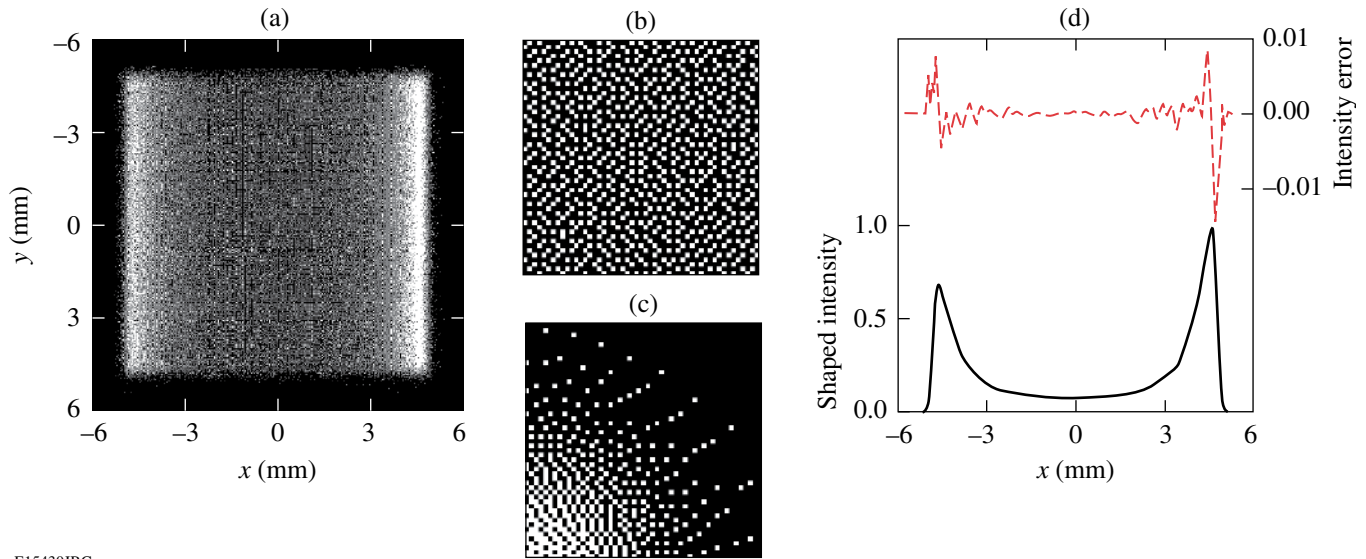

Figure 108.49
(a)–(c) Close-ups of shapers designed with error diffusion for a target-intensity transmission equal to 5%, 25%, and 75%, respectively; (d)–(f) close-ups of shapers designed with the random dither algorithm for a target-intensity transmission equal to 5%, 25%, and 75%, respectively.

This lineout corresponds to the optimal filtering in the Fourier plane, as discussed below. As can be seen, the shaped intensity varies by less than 1% around the target intensity. Intensities of the far field of the shapers generated by error diffusion and random dither are compared in Fig. 108.51, where the average of the far-field intensity in a 4-mrad interval along the y direction has been plotted on a logarithmic scale as a function of the angle in the x direction. The noise due to the binarization is pushed to high frequencies in the case of the error diffusion algorithm but is present at all frequencies in the case of the random dither algorithm—an example of the general behavior of spatially dithered masks generated with error diffusion.[17] The spectrum of the noise introduced by the binarization has no zero-frequency component and has only significant density at high frequencies, therefore the name "blue-noise dithering."[18] By comparison, the randomness of the random draw design algorithm generates a constant noise background in the far field (i.e., "white noise"). This point is particularly important for Fourier filtering because the amplitude filter in the far field (e.g., the pinhole) can effectively block the binarization noise while preserving the frequency content of the target transmission.

To demonstrate the influence of the filtering operation, the rms error is calculated as a function of the angular diameter of a circular pinhole set in the far field for a shaping element designed with error diffusion and random dither to approximate the target-shaped intensity of Fig. 108.46(b). The rms error is also calculated when propagating a field having the

target-shaped intensity. Figure 108.52(a) shows that the rms error is limited at low pinhole sizes by the propagation of the target-shaped intensity through the filtering system (i.e., the high frequencies of this intensity are blocked by the pinhole) that also constrains the rms error in the case of the binary distributions. The error increases quickly for the random dither algorithm as the pinhole size is increased, but decreases in case of error diffusion. The rms error reaches a minimum for

a given pinhole diameter for each design algorithm. The rms error is minimal for a 7-mrad pinhole in the case of error diffusion ($\varepsilon_{rms} = 0.7\%$, $\varepsilon_{peak} = 2.4\%$) and for a 3-mrad pinhole in the case of the random dither algorithm ($\varepsilon_{rms} = 7.5\%$, $\varepsilon_{peak} = 27.4\%$). The corresponding shaped intensities were used to calculate the intensity after amplification, which is expected to be functionally similar to that of Fig. 108.46(a). The three lineouts of the amplified intensity plotted in Figs. 108.53(a)

E15430JRC

Figure 108.50
(a) Binary shaper corresponding to the transmission of Fig. 108.46(b); (b) and (c): close-ups of the binary pixel distribution at the center and at the upper right corner of the beam, respectively; (d) lineout of the filtered intensity along the x direction (solid line) and lineout of the difference between the filtered intensity and the target intensity (dashed line).
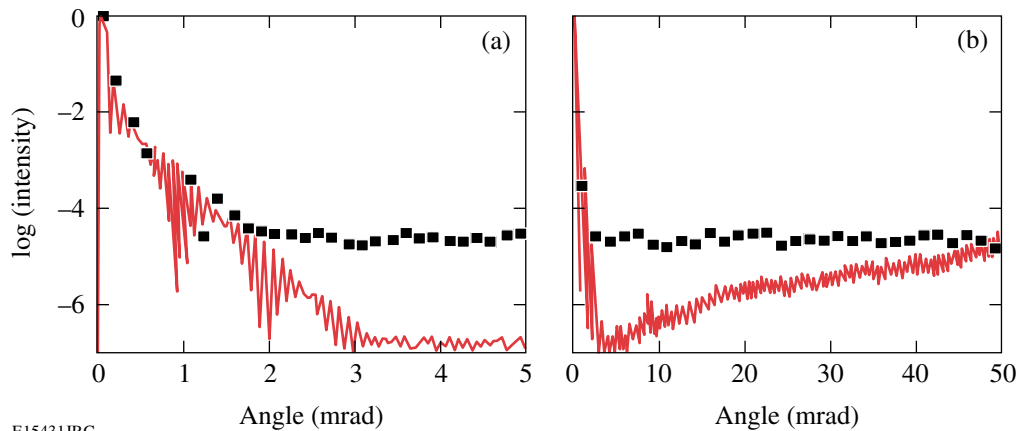
E15431JRC

Figure 108.51
Intensity of the far field of the binary beam shaper designed with the error diffusion algorithm (solid line) and the random dither algorithm (squares) for the generation of a shaped intensity of Fig. 108.46(c). The intensity is averaged over a 4-mrad angle in the y direction and plotted versus the angle in the x direction. Plots (a) and (b) cover different ranges of angles.

and 108.53(b) show that the modulations due to the shaping process are not detectable for error diffusion, but are significant for random dither.

We have also studied the effect of pixel size in the design of shapers. It is intuitive that smaller pixels lead to better resolution in the reproduction of the shaping function. This is demonstrated by plotting the rms error as a function of the pinhole diameter for the shaping function of Fig. 108.46(b) designed with error diffusion and binary shapers with 10-, 20-,

and 40-μm pixels [Fig. 108.52(b)]. Larger pixels increase the rms error, and influence the shaping performance in two ways: they generally decrease the ability to generate quickly varying functions and, in the case of a binary distribution, they imply a reduction in the number of parameters available to locally specify a gray level (for example, an area of 10-μm binary pixels has 16 times more bits of information than the same area covered with 40-μm pixels). The minimal rms error for a given pixel size is obtained for a pinhole size that decreases when the pixel size is increased. A shaper with 10-μm pixels

E15432JRC
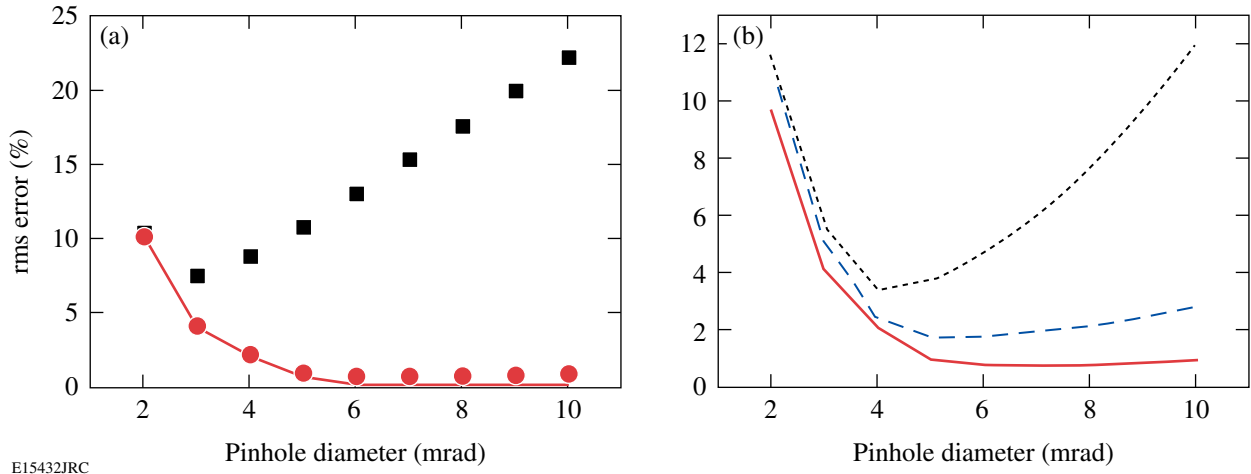
Figure 108.52
(a) rms error for the realization of the shaped intensity of Fig. 108.46(b) as a function of the pinhole angular diameter in the case of the error diffusion algorithm (circles) and the random draw algorithm (squares). The solid line corresponds to the propagation of a field having the target-shaped intensity through the same filtering system. (b) rms error for the realization of the shaped intensity of Fig. 108.46(b) as a function of the pinhole angular diameter for a pixel size of 10 μm (solid line), 20 μm (dashed line), and 40 μm (dotted line) in the case of error diffusion.
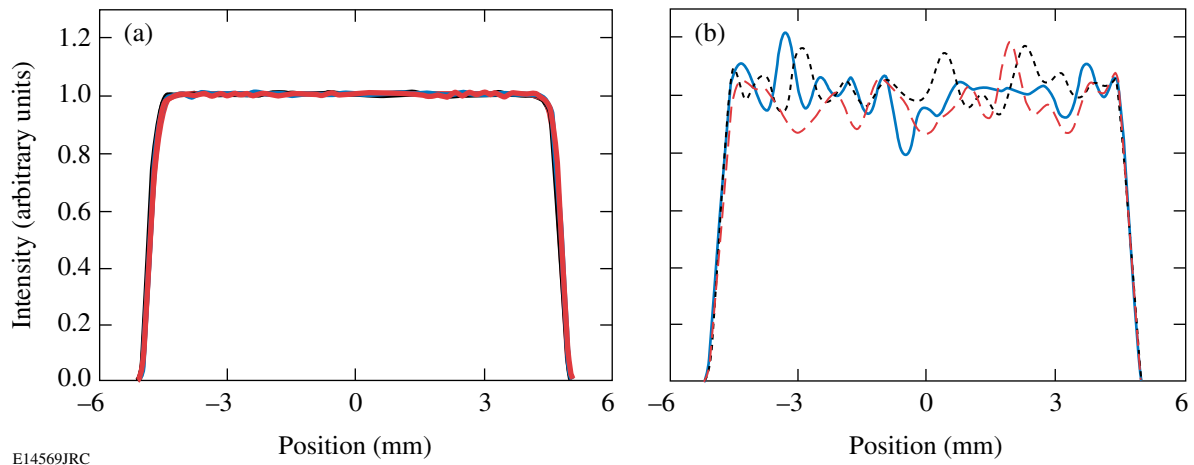

E14569JRC

Figure 108.53
Three lineouts of the simulated intensity of the shaped beam after amplification for shaping with (a) error diffusion and (b) random dither. In each case, the pixel size is 10 μm, and the pinhole size leading to the smallest rms error is used.

leads to $\varepsilon_{\text{rms}} = 0.7\%$ and $\varepsilon_{\text{peak}} = 2.4\%$ with a 7-mrad pinhole; with 20-μm pixels leads to $\varepsilon_{\text{rms}} = 1.7\%$ and $\varepsilon_{\text{peak}} = 4.3\%$ with a 5-mrad pinhole; and with 40-μm pixels leads to $\varepsilon_{\text{rms}} = 3.4\%$ and $\varepsilon_{\text{peak}} = 9\%$ with a 4-mrad pinhole.

Effect of Feature-Size Variation
on the Shaping Performance

Practical applications of shapers are constrained by the ability to faithfully reproduce small-scale features. A typical process for generating metal masks is based on lithography.[19] In the case of wet-etch lithography, etching can lead to a reduction in feature size, i.e., the light-blocking metal pixels are smaller than specified in the design, which leads to an increased transmission. It is important to understand the scaling of this effect, quantify it, and potentially come up with precompensation schemes.

1. Analytical Derivation

The design of shapers using error diffusion leads to highly ordered distributions of pixels, as shown in the previous section. It has been observed that shapers with isolated 100% transmission blanks [example in Fig. 108.49(a)] were obtained for target transmission smaller than 10%. Shapers with isolated 0% transmission pixels were obtained for target transmissions higher than 45% [example in Fig. 108.49(c)]. In these cases, the transmission can be predicted uniquely from the knowledge of the area of a blank (in the first case) and the area of a pixel (in the second case), these areas being scaled to the expected nominal area for these features.

In the case of isolated blanks, the intensity transmission after Fourier filtering is

$$T_{\text{obtained}} = d_{\text{blank}}^2 = \left(\frac{B \times S_{\text{blank}}}{N \times S_0} \right)^2, \qquad (3)$$

where d_{blank} is the density of blank pixels, B is the number of blank pixels in a representative area with a total number of pixels equal to N, S_{blank} is the surface of a blank pixel, and S_0 is the nominal surface of a pixel. Using the fact that $T_{\text{target}} = (B/N)^2$, one obtains the relation describing the transmission of regions with isolated blanks as

$$T_{\text{obtained}} = T_{\text{target}} \times \left(\frac{S_{\text{blank}}}{S_0} \right)^2. \qquad (4)$$

In the case of isolated pixels, the intensity transmission after Fourier filtering is

$$T_{\text{obtained}} = (1 - d_{\text{metal}})^2 = \left(1 - \frac{M \times S_{\text{metal}}}{N \times S_0} \right)^2, \qquad (5)$$

where d_{metal} is the density of metal pixels, M is the number

of metal pixels in a representative area with a total number of pixels equal to N, S_{metal} is the surface of a metal pixel, and S_0 is the surface of a pixel. Using the relation $T_{\text{target}} = \left[1 - (M/N) \right]^2$, one obtains

$$T_{\text{obtained}} = \left[\left(1 - \sqrt{T_{\text{target}}} \right) \times \frac{S_{\text{metal}}}{S_0} - 1 \right]^2. \qquad (6)$$

For transmissions between 10% and 45%, analytical derivation is not as simple. In the special case of a target transmission equal to 25%, the generated distribution of pixels is a checkerboard of metal and blank pixels [example in Fig. 108.49(b)], for which it can be seen that the transmission error can be predicted considering isolated metal pixels if the feature-size variation is due to the edge effect simulated below, i.e., using Eq. (6).

2. Simulations

A simulation was performed to quantify the impact of pixel-size mismatch on the transmission of shapers. It is assumed that the primary effect of pixel-size variation is an edge effect, i.e., a metal pixel neighboring a blank pixel is over-etched and an additional section of metal is removed from the corresponding edge. The offset is defined as the ratio of the length of metal additionally removed over the nominal size of the pixel (e.g., nominal 10-μm metal pixels losing 0.5 μm on each side correspond to a 5% offset, and an isolated metal pixel becomes a 9-μm pixel). A mask for a constant transmission T_{target} after filtering is first generated. The edge effect is simulated by increasing the transmission of every blank in the mask by n times the relative change due to the over-etching, where n corresponds to the number of neighboring metal pixels. The obtained transmission is obtained by calculating the actual transmission of the mask after this operation to get T_{obtained}. The transmission error is then defined as $(T_{\text{obtained}}/T_{\text{target}}) - 1$. While these simulations assume a specific process for the transmission degradation, it has been found to describe accurately our experimental results. One should note however that the formulas of Eq. (4) and Eq. (6) are valid for shapers with isolated blanks and pixels of arbitrary shape.

The transmission error is plotted in Fig. 108.54 as a function of the target transmission in the case of a 5% offset (e.g., 9-μm pixels obtained on a 10-μm grid) and a 10% offset (e.g., 8-μm pixels obtained on a 10-μm grid), with the corresponding analytical prediction calculated using the size of both the metal and blank pixels. The simulations and the analytical predictions of Eq. (4) and Eq. (6) agree well in their respective domain of validity. For over-etched metal pixels, the maximal transmission error is obtained for low target-intensity transmission smaller than 10%. The predicted transmission error at low

design transmission using the surface of a blank and Eq. (4) is, respectively, 44% and 96% for size offset equal to 5% and 10%. This error can be reduced by decreasing the offset in pixel size. While small pixels lead theoretically to better shaping capabilities, the absolute reduction in metal pixel size due to lithography is mostly independent of the pixel size, i.e., the offset becomes larger when using smaller pixels. For example, a process leading to a 10% offset error on 10-μm pixels would give only a 5% offset on 20-μm pixels. There is a trade-off between shaping capabilities and transmission error, unless some precompensation of the shaper design taking into account the feature size of the mask is performed.
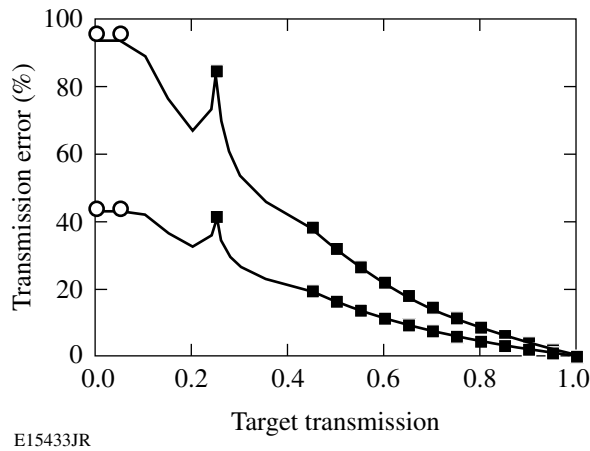
E15433JR

Figure 108.54

Transmission error simulated as a function of the target-intensity transmission for a pixel-size offset equal to 5% (lower curve) and 10% (upper curve). In each case, the circles correspond to the error prediction using Eq. (4) and the squares correspond to the error prediction using Eq. (6) (markers are plotted only in the domain of validity of these two equations).

3. Precompensation

Precompensation of the transmission error due to the feature size is made possible by the predictability of the transmission error. While an exact knowledge of the transmission error requires an exact knowledge of the feature sizes and shapes, one can rely on an approximate model of the pixel shape and size to precompensate the transmission by modifying the pixel density. One starts with the knowledge of the relation between design transmission and obtained transmission, written as $T_{\text{obtained}} = f(T_{\text{design}})$. It suffices to chose $T_{\text{design}} = f^{-1}(T_{\text{target}})$ to obtain $T_{\text{obtained}} = T_{\text{target}}$, where f^{-1} is the reciprocal function of f. Precompensation can be performed simply by applying the error diffusion algorithm to $f^{-1}[T_{\text{target}}(x,y)]$ instead of $T_{\text{target}}(x,y)$. In practice, the exact shape of the function f (and f^{-1}) is not known. It depends on the feature size of the generated shaper as well as the feature shape. These properties are

likely to be similar for different runs of the same fabrication process, which allows some precompensation of these effects at the design stage.

The function f calculated in the previous subsection for a 5% offset was used to precompensate the shaper design. As in the previous subsection, shapers with a target transmission ranging from 0% to 100% were generated by applying the error diffusion algorithm. The transmission obtained with these shapers was then calculated, following the previous procedure, for pixels corresponding to offsets equal to 4%, 5%, and 6%. The transmission error in the absence of precompensation for these three offsets is plotted in Fig. 108.55(a). It can be compared to the transmission error with precompensation of a 5% offset, which is plotted in Fig. 108.55(b). A significant reduction of the transmission error is obtained. As expected, the transmission error after precompensation is positive for an offset equal to 6%, approximately equal to zero for an offset of 5%, and negative for an offset equal to 4%.
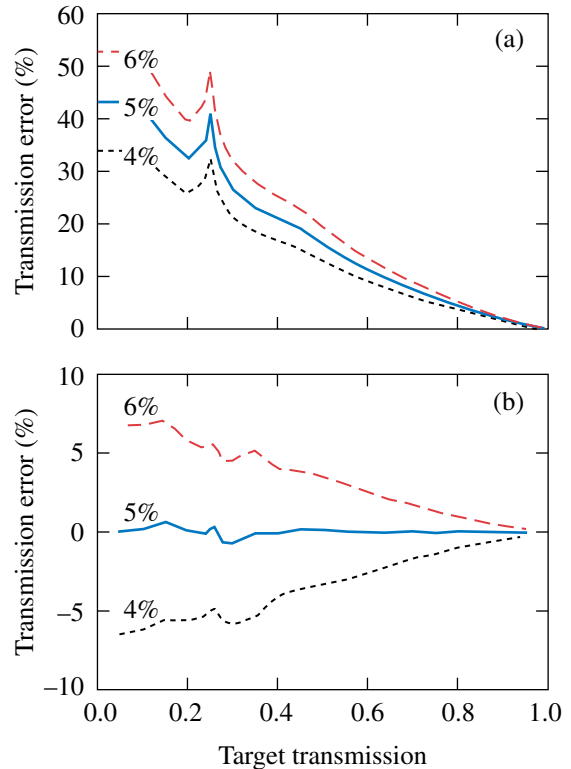
E15434JRC

Figure 108.55

Transmission error as a function of the target transmission for pixel-size offsets equal to 4% (dotted line), 5% (solid line), and 6% (dashed line) (a) without precompensation and (b) with precompensation of the pixel-size offset assuming a pixel-size offset equal to 5%.

Conclusion

The error diffusion algorithm has been studied in the context of the design of beam shapers for high-power laser applications. The high resolution and accurate reproduction of continuous shaping functions is beneficial to these applications. In particular, it has been shown that the shaped intensity has no significant hot spots, therefore decreasing the risk of damage in the laser system. The practical problem of accurate feature size reproduction has been studied in detail, and it has been shown that the transmission error can be reduced significantly by proper biasing of the target transmission before applying the design algorithm. The pixel size should be chosen by considering both the theoretical shaping capability and the influence of the practical fabrication process.

REFERENCES

1. U. Efron, *Spatial Light Modulator Technology: Materials, Devices, and Applications*, Optical Engineering, Vol. 47 (Marcel Dekker, New York, 1995).

2. I. N. Ross *et al.*, J. Opt. Soc. Am. B **19**, 2945 (2002).

3. V. Bagnoud *et al.*, Opt. Lett. **26**, 337 (2001).

4. T. Yu. Cherezova *et al.*, Appl. Opt. **40**, 6026 (2001).

5. A. J. Campillo *et al.*, Opt. Commun. **10**, 313 (1974).

6. G. Emiliani *et al.*, Appl. Opt. **28**, 2832 (1989).

7. G. Giuliani, Y. K. Park, and R. L. Byer, Opt. Lett. **5**, 491 (1980).

8. G. Dubé, Opt. Commun. **12**, 344 (1974).

9. J. M. Auerbach and V. P. Karpenko, Appl. Opt. **33**, 3179 (1994).

10. B. M. Van Wonterghem *et al.*, Appl. Opt. **36**, 4932 (1997).

11. G. H. Miller, E. I. Moses, and C. R. Wuest, Nucl. Fusion **44**, S228 (2004).

12. M. Henesian, Lawrence Livermore National Laboratory, Livermore, CA, private communication (2006).

13. J. H. Kelly, L. J. Waxer, V. Bagnoud, I. A. Begishev, J. Bromage, B. E. Kruschwitz, T. J. Kessler, S. J. Loucks, D. N. Maywar, R. L. McCrory, D. D. Meyerhofer, S. F. B. Morse, J. B. Oliver, A. L. Rigatti, A. W. Schmid, C. Stoeckl, S. Dalton, L. Folnsbee, M. J. Guardalben, R. Jungquist, J. Puth, M. J. Shoup III, D. Weiner, and J. D. Zuegel, J. Phys. IV France **133**, 75 (2006).

14. R. Ulichney, *Digital Halftoning* (MIT Press, Cambridge, MA, 1987).

15. J. Stoffel and J. Moreland, IEEE Trans. Commun. **29**, 1898 (1981).

16. R. W. Floyd and L. Steinberg, J. Soc. Inf. Disp. **17**, 75 (1976).

17. S. Weissbach and F. Wyrowski, Appl. Opt. **31**, 2518 (1992).

18. R. A. Ulichney, Proc. IEEE **76**, 56 (1988).

19. M. J. Madou, *Fundamentals of Microfabrication: The Science of Miniaturization* (CRC Press, Boca Raton, FL, 2002).

LLE's Summer High School Research Program

During the summer of 2006, 13 students from Rochester-area high schools participated in the Laboratory for Laser Energetics' Summer High School Research Program. The goal of this program is to excite a group of high school students about careers in the areas of science and technology by exposing them to research in a state-of-the-art environment. Too often, students are exposed to "research" only through classroom laboratories, which have prescribed procedures and predictable results. In LLE's summer program, the students experience many of the trials, tribulations, and rewards of scientific research. By participating in research in a real environment, the students often become more excited about careers in science and technology. In addition, LLE gains from the contributions of the many highly talented students who are attracted to the program.

The students spent most of their time working on their individual research projects with members of LLE's technical staff. The projects were related to current research activities at LLE and covered a broad range of areas of interest including computational hydrodynamics modeling, materials science, laser-fusion diagnostic development, fiber optics, database development, computational chemistry, and the computational modeling of electron, neutron, and radiation transport (see Table 108.VI).

The students attended weekly seminars on technical topics associated with LLE's research. Topics this year included laser physics, fusion, holographic optics, fiber optics, liquid crystals, atomic force microscopy, and the physics of music. The students also received safety training, learned how to give scientific presentations, and were introduced to LLE's resources, especially the computational facilities.

The program culminated on 30 August with the "High School Student Summer Research Symposium," at which the students presented the results of their research to an audience including parents, teachers, and LLE staff. The students' written reports will be made available on the LLE Web site and bound into a permanent record of their work that can be cited in scientific publications.

Two hundred and four high school students have now participated in the program since it began in 1989. This year's students were selected from approximately 60 applicants.

At the symposium, LLE presented its tenth William D. Ryan Inspirational Teacher Award to Mr. Thomas Lewis, a former earth science teacher (currently retired) at Greece Arcadia High School. This award is presented to a teacher who motivated one of the participants in LLE's Summer High School Research Program to study science, mathematics, or technology and includes a $1000 cash prize. Teachers are nominated by alumni of the summer program. Mr. Lewis was nominated by Benjamin L. Schmitt, a participant in the 2003 Summer Program, with a letter co-signed by 13 other students. "Mr. Lewis was an inspirational, monumental educator (scientific and otherwise), developing a course to be known as 'Advanced Earth Science' as a response to the Advanced Placement science program," Benjamin writes in his nomination letter. "He provided constant challenges and supplied his students with current publications and electronic media about their individual interests." His pursuit of direct student encouragement and interaction came with weekly invitations to his home for star-viewing events. Mr. Lewis "holds one of the most distinguished records in the New York State High School Science Olympiad... spending countless hours each year outside of normal school hours to lead practices, assist with studying... the construction of technical event projects. His devotion to student learning was unmatched by any other teacher or Science Olympiad coach to succeed him." Mr. Lewis announced that he would donate his $1000 award to the Science Olympiad.

Table 108.VI: High School Students and Projects—Summer 2006.

Name	High School	Supervisor	Project Title
Deshpreet Bedi	Brighton	F. Marshall	X-Ray Diffraction Measurements of Laser-Generated Plasmas
Ryan Burakowski	Churchville-Chili	T. Kosc	PCLC Flakes for OMEGA Laser Applications
Alexandra Cok	Allendale Columbia	S. Craxton	Optimization of Polar Direct Drive Beam Profiles for Initial NIF Targets
Zuzana Culakova	Brighton	K. Marshall	Organic Coatings for Hardening of Laser Optics
Eric Dobson	Harley	J. Delettrez	Modeling Collisional Blooming and Straggling of the Electron Beam in the Fast Ignition Scenario
Elizabeth Gregg	Naples Central	S. Mott/ J. Zuegel	Development of a Test Apparatus for the Optimization of Fiber Splicing
Daniel Gresh	Wheatland-Chili	R. Kidder	Implementing a Knowledge Database for Scientific Control Systems
Matt Heavner	Fairport	C. Stoeckl	Realtime Focal Spot Characterization
Sean Lourette	Fairport	C. Stoeckl	Neutron Transport Calculations Using Monte-Carlo Methods
Ben Matthews	York Central	D. Lonobile/ G. Brent	Precision Flashlamp Current Measurement—Thermal Sensitivity and Compensation Techniques
Ryan Menezes	Webster Schroeder	D. Harding	Evaluation of Confocal Microscopy for Measurement of the Roughness of Deuterium Ice
Rui Wang	Fairport	K. Marshall	Nickel Dithiolene Systems: Computational Modeling of Spectral Properties
Nicholas Whiting	Bloomfield	R. Epstein	Dynamic Energy Grouping in Multigroup Radiation Transport Calculations

FY06 Laser Facility Report

During FY06 the OMEGA Facility conducted 1394 target shots for a variety of users. Shaped-pulse cryogenic DT implosions highlighted the development of direct-drive cryogenic capability. A total of 12 D_2 and 15 DT direct-drive cryogenic target implosions were performed (see Table 108.VII). OMEGA Availability and Experimental Effectiveness averages for FY06 were 93.3% and 95.3%, respectively (see Fig. 108.56). Highlights of other achievements for FY06 include the following:

- The first of a series of direct-drive, ignition-scaled cryogenic targets containing tritium were imploded in February 2006. LLE achieved a DOE milestone in March by imploding two layered DT cryogenic targets containing tritium. The first high-yield, direct-drive, ignition-scaled, 50% DT cryogenic implosion was achieved in June 2006—the first time that such a target was imploded on an ICF facility. OMEGA is now fully capable of fielding high-tritium-fraction cryogenic

Table 108.VII: The OMEGA target shot summary for FY06.

Laboratory	Planned Number of Target Shots	Actual Number of Target Shots	IDI NIC	DDI NIC	Total NIC	Non-NIC
LLE	724	714	201	497	698	16
LLNL	325	348	243	0	243	105
LANL	121	125	54	0	54	71
NLUF	120	122	0	0	0	122
CEA	40	49	0	0	0	49
SNL	24	30	30	0	30	0
NWET	6	6	0	0	0	6
Total	1360	1394	528	497		369
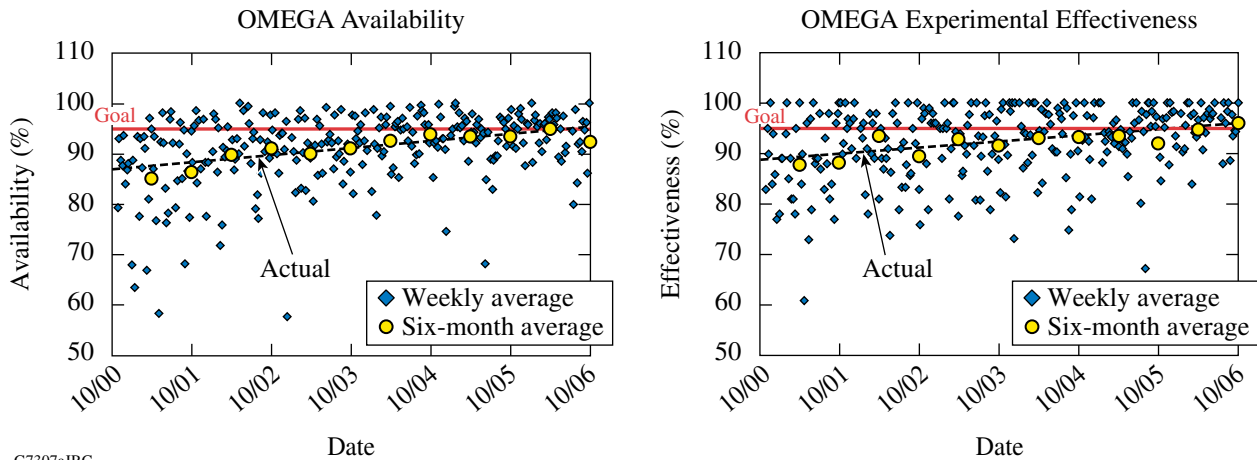
G7307aJRC

Figure 108.56
OMEGA Availability and Experimental Effectiveness data from FY01 to FY06.

targets and has the infrastructure in place to support the corresponding radiological issues.

• A full set of 42 new indirect-drive-ignition distributed phase plates (IDI DPP's) were designed and fabricated for National Ignition Campaign (NIC) experiments on OMEGA. The phase plates produce an elliptical far field (200 μm × 300 μm) at normal incidence and a nearly circular spot at the plane of the laser entrance hole (LEH) and can be oriented for use in both pent and hex configurations. Hohlraum energetics experiments using IDI DPP's were successfully conducted in August, completing a DOE milestone for the National Ignition Campaign. The primary objective of these experiments is to study the effect of laser-beam smoothing with phase plates on the radiation temperature and scattering losses of the hohlraum.

• Low-adiabat, high-contrast pulse shapes are required for OMEGA ignition-scaled cryogenic DT target experiments. Such pulse shapes are typically characterized by a narrow picket pulse on top of a low-intensity foot pulse, followed by a high-intensity drive pulse. The new front end on OMEGA— the integrated front-end source (IFES)—is a highly stable optical-pulse-generation system based on fiber amplification of an optical signal that is temporally carved from a continuous-wave fiber laser. The use of fiber-optic lasers and amplifiers and waveguide temporal modulators makes IFES ideally suited for producing reliable, stable pulse shapes. Recent experiments on OMEGA have required >100:1-contrast-ratio pulse shapes. The electrical waveform that drives the waveguide modulators to shape the pulse is produced using LLE's aperture-coupled-strip-line (ACSL) technology. The shape is designed to precompensate the temporal distortions in the laser due to amplifier gain saturation and nonlinear conversion in the frequency-conversion crystals (FCC's). Figure 108.57 shows (on a logarithmic scale) the design template and the measured ultraviolet laser pulse produced on target by OMEGA for pulse shape LA279901P. The match between the designed and measured shapes is excellent, particularly in the following critical pulse parameters: the picket energy, the >l00:1-contrast foot, and the rising edge of the drive pulse.

• A year-long project to upgrade the active-shock-breakout (ASBO) diagnostic was completed in April 2006. The upgrade
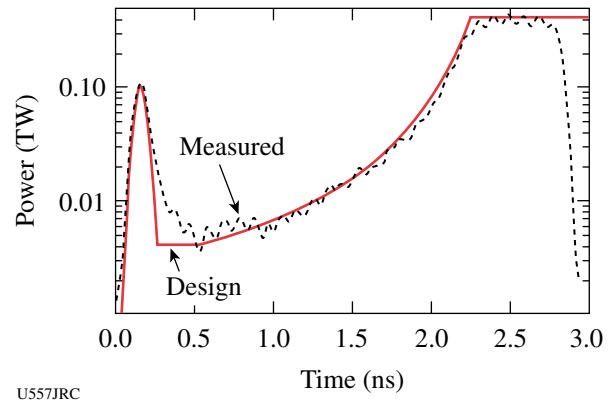
Figure 108.57
OMEGA single-beam pulse shape from low-adiabat cryogenic target implosions (shot #42966) using pulse shape LA279901P.

enables high-precision measurements and ease of operation for equation-of-state (EOS) and shock-timing experiments. Using the existing system as a baseline, the upgrade incorporates a new optical layout that uses the Rochester Optical Streak System (ROSS) streak cameras as detectors for the two velocity interferometer system for any reflector (VISAR) channels. The result is an outstanding optical device that provides excellent performance and smooth operation using the accurately calibrated ROSS cameras. Many experiments are using the new ASBO system. CCD camera data-acquisition capability for x-ray framing cameras was extended to TIM's 4 and 5 and is now available on all TIM's.

• The OMEGA EP short-pulse beam-transport tube was installed during an extended maintenance week in June 2006. The beam-transport tube connects the OMEGA EP grating compression chamber located within the OMEGA EP Target Bay to port P9 on the OMEGA target chamber. Significant structural modifications within the OMEGA target area were required to facilitate the installation of the short-pulse beam tube including target bay platform structural modifications, modifications required to facilitate access to OMEGA UV transport optics, and the addition of two Target Bay jib cranes. Facility modifications planned for FY07 include the relocation of TIM 2 from port H7 to port H3, installation of the off-axis parabola in port H7, and installation of the OMEGA EP transport mirrors on the east side of the OMEGA target chamber.

National Laser Users' Facility and External Users' Programs

During FY06, 680 target shots were taken on OMEGA for external users' experiments, accounting for 48.8% of the total OMEGA shots for the year. The external users during this year included seven collaborative teams participating in the National Laser Users' Facility (NLUF) program and many collaborative teams from the National Laboratories (LLNL, LANL, and SNL) and the Commissariat à l'Énergie Atomique (CEA) of France. Some of this work is highlighted in this section.

NLUF Program

In FY06, the Department of Energy (DOE) issued a solicitation for NLUF grants for the period of FY07–FY08. A total of 12 proposals were submitted to DOE for the NLUF FY07/08 program. An independent DOE Technical Evaluation Panel comprised of Prof. Ani Aprahamian (University of Notre Dame), Dr. Steven Batha (LANL), Dr. Ramon Leeper (SNL), Prof. Howard Milchberg (University of Maryland), and Dr. Robert Turner (LLNL) reviewed the proposals on 18 April 2006 and recommended that six of the twelve proposals receive DOE funding and shot time on OMEGA in FY07–FY08. Table 108.VIII lists the successful proposals.

FY06 NLUF Experiments

FY06 was the second of a two-year period of performance for the NLUF projects approved for the FY05–FY06 funding and OMEGA shots. Six of these NLUF projects were allotted OMEGA shot time and received a total of 122 shots on OMEGA in FY06. Some of this work is summarized in this section.

Isentropic Compression Experiments (ICE) for Measuring EOS on OMEGA
Principal Investigators: Y. M. Gupta and J. R. Asay (University of Washington)

This experimental effort is geared toward developing new areas of high-pressure research. The aim of the FY06 shots was to continue development of techniques to generate high-accuracy, quasi-isentrope, equation-of-state data. This will make possible, for the first time, "cold" stress-density loading curves for standard materials at loading rates up to ten times higher than possible with other methods in the Mbar regime. For the FY05 NLUF allocation, a platform was developed to produce high-accuracy and high-pressure stress-strain data on aluminum.[1] This was the first such data to be measured with a

Table 108.VIII: FY07–FY08 NLUF Proposals.

Principal Investigator	Affiliation	Proposal Title
R. P. Drake	University of Michigan	Experimental Astrophysics on the OMEGA Laser
R. Falcone	University of California, Berkeley	X-Ray Compton Scattering on Compressed Matter
P. Hartigan	Rice University	Laboratory Experiments on Supersonic Astrophysical Flows Interacting with Clumpy Environments
R. Jeanloz	University of California, Berkeley	Recreating Planetary Core Conditions on OMEGA—Techniques to Produce Dense States of Matter
R. Mancini	University of Nevada, Reno	Multiview Tomographic Study of OMEGA Direct-Drive Implosion Experiments
R. D. Petrasso, C. K. Li	Massachusetts Institute of Technology	Monoenergetic Proton Radiography of Laser/Plasma-Generated Fields and ICF Implosions

laser driver and was taken with ramp compression timescales more than ten times faster than had previously been possible. A stiffer response of aluminum was observed than had been previously observed at slower ramp compression experiments on the Z facility at Sandia National Laboratory. In addition, it was observed that the elastic–plastic transition is much larger than expected from previous work at Z. This points to a strong rate dependence in the material strength. The new high-strain-rate data provided by these experiments are being used to benchmark models that incorporate time dependence being developed at Washington State University (WSU).

On 26 April 2006, 14 shots were performed on isentropic compression targets. The ICE-EOS package, as shown in Fig. 108.58, consists of a Au hohlraum, a plastic reservoir followed by a vacuum gap, and a triple-stepped Ta target. Fifteen beams from the OMEGA laser at 0.35-μm wavelength, containing a combined energy of 5 kJ in a 2-ns temporally flat pulse, are focused symmetrically onto the inner walls of the Au hohlraum (1.7-mm LEH, 2.2-mm diameter, 1.7-mm length). This confined high-Z geometry results in a near-blackbody distribution of thermal x rays ($T_h \sim 120$ eV) with uniform temperature gradients over a spatial region close to the diameter of the hohlraum. The hohlraum is attached to a 25-μm-thick Be foil glued to a 180-μm-thick, 12% Br-doped polystyrene foil (C$_8$H$_6$Br$_2$). The x-ray field within the hohlraum launches an ablatively driven shock through the foil. The initial region of planarity is expected to approach the diameter of the halfraum and can extend over millimeters. The Bromine dopant absorbs high-energy Au M-band x rays (~2 to 5 keV) generated within the hohlraum, which otherwise could preheat the Ta step sample. After breakout from the rear-surface shock, heating and momentum cause the Br-CH to dissociate and unload across a 600-μm vacuum gap. Transit across the vacuum gap causes the mass-density gradients along the target axis to relax as a function of distance from the original Br-CH/vacuum-gap interface. The unloading Br-CH monotonically loads up against the Ta sample, and the imparted momentum launches a ramp stress wave through the material. The temporal profile of the compression wave may be shaped by varying the size of the vacuum gap, the density of the reservoir, or the temperature within the hohlraum. In the FY06 experiments the main targets consisted of 25/40/55/70 μm Ta or W. A significant change in the target design from the previous campaigns in FY05 was the inclusion of a Be ablator and 1-μm CH liner on the inner wall of the Au hohlraum. The purpose of this modification was to keep the hohlraum open for ~80 ns to facilitate future on-axis radiography experiments that would diagnose material properties (e.g., material strength) during compression. In this context an "open" hohlraum means no on-axis, line-of-sight Au content that would

serve to absorb the flash x-ray photons used for radiography. Be has a high-ablation velocity, and its inclusion (1) increases the x-ray ablative shock pressure into the sample for a given input laser energy and (2) serves to fill the holhraum rapidly and thus acts as a filler, which delays the on-axis stagnation of the cylindrically converging Au holhraum material. The 1-μm-CH liner serves to further tamp the hohlraum collapse. The primary goal of the FY06 NLUF shots was to use this planar drive to extract a single-shot series of equation-of-state (EOS) data for Ta and W up to peak pressures in excess of 1 Mbar.
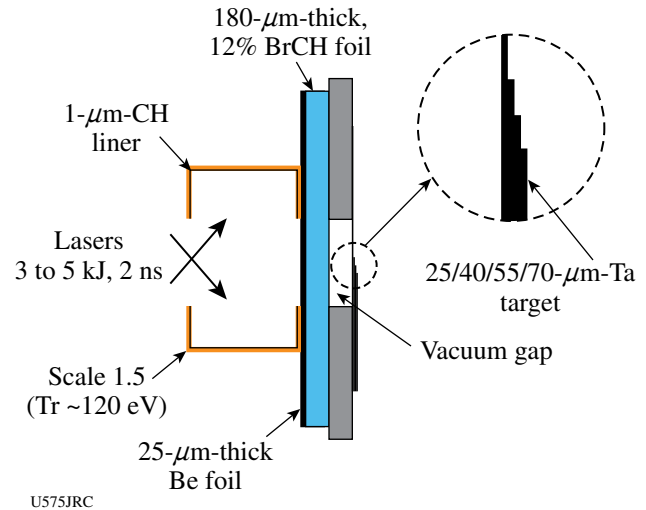

Figure 108.58
Schematic of ICE–EOS target package. The inclusion of a Be ablator and a 1-mm CH liner material serves to keep the hohlraum open for ~100 ns, as was verified in a separate radiography campaign.

The time history of the Ta/vacuum interface acceleration is recorded with a line-imaging velocity interferometer [velocity interferometry system for any reflector (VISAR)] with two channels set at different sensitivities. The time-resolved fringe movement recorded by a streak camera is linearly proportional to the velocity of the reflecting surface, which in this case is the Ta/vacuum interface. This allows an accurate measurement of the free-surface velocity as a function of time. The streak camera output of the VISAR for the target conditions described in Fig. 108.58 is shown in Fig. 108.59. The recently upgraded LLE VISAR provides a greater target field of view than had previously been possible, thereby allowing the use of four separate steps on a single shot for the first time, which ultimately increases the accuracy of the equation-of-state measurement.

The VISAR image provides spatial resolution at the target plane over ~800 μm and temporal resolution of the interferometer fringe displacement over a 30-ns time window. A planar
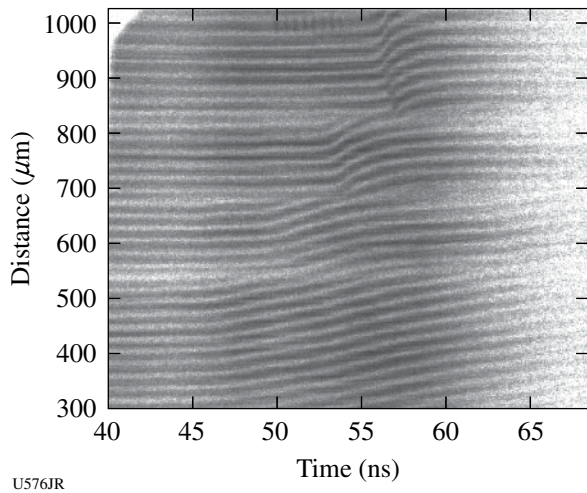
Figure 108.59
VISAR streak record for target conditions described in Fig. 108.58.

drive was observed across the field of view with smooth ramp unloading from the 25-, 40-, 55-, and 70-μm-Ta samples at progressively later times. The velocity sensitivity (set by the resolving element within the VISAR) is 0.995 km s^{-1} fringe shift^{-1}. Using Fourier analysis and after deconvolving the data for temporal and spatial distortions within the streak camera, the time-resolved free-surface velocity (U_{FS}) profile for each Ta thickness (Fig. 108.60) can be extracted. There is a very pronounced elastic–plastic precursor wave on all steps. An
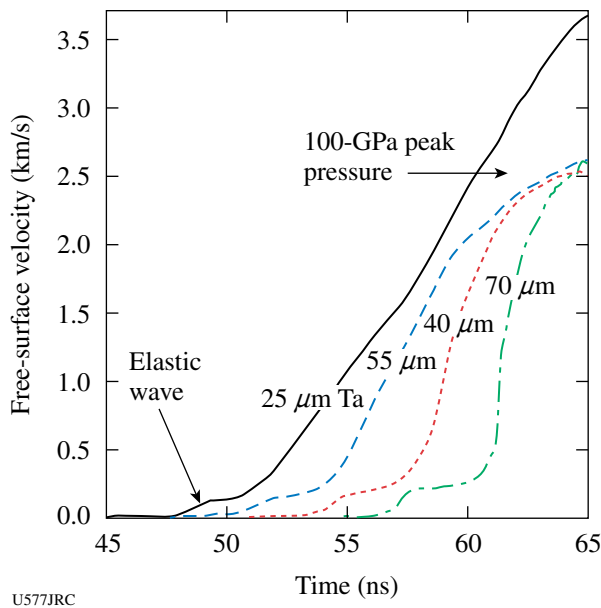
Figure 108.60
Free-surface velocity profile deduced from the data in Fig. 108.59.

increase in this elastic–plastic wave as a function of Ta thickness/ramp rise time is observed. This is an important observation that points to a rate dependence in the material response. Analysis of this data is ongoing.

Using the iterative analysis technique described by Rothman *et al.*,[2] the free-surface velocity profiles in Fig. 108.60 can be used to generate a path through stress-density space up to 1 Mbar (Ref. 1). In future experiments techniques will be developed to shape the pressure profile of the ramp compression wave by using graded density reservoir materials.[3] This will increase the shock-up distance within the target, which in turn will facilitate larger step heights resulting in lower error bars. In addition, the use of graded density reservoirs is expected to increase the accessible peak pressure on OMEGA to greater than 4 Mbar.

Laser–Plasma Interactions in High-Energy-Density Plasmas
Principal Investigator: H. Baldis (University of California, Davis)

High-temperature hohlraums (HTH) are designed to reach high radiation temperatures by coupling a maximum amount of laser energy into a small target in a short time. These 400- to 800-μm-diam gold cylinders fill rapidly with hot plasma during irradiation with multiple beams in 1-ns laser pulses. The high-Z plasmas are dense, (electron density $n_e/n_c \sim 0.1$ to 0.4), hot (electron temperature $T_e \sim 10$ keV), and bathed in a high-temperature radiation field (radiation temperature $T_{rad} \sim 300$ eV). Here the critical density n_c equals 9×10^{21}/cm^3. The laser beams heating this plasma are intense ($\sim 10^{15}$ to 10^{17} W/cm^2). The coupling of the laser to the plasma is a rich regime for laser–plasma interaction (LPI) physics. The LPI mechanisms in this study include beam deflection and forward scattering. To understand the LPI mechanisms, the plasma parameters must be known. An L-band spectrometer is used to measure the electron temperature. A ride-along experiment is to develop the x-radiation emitted by the thin back wall of the half-hohlraum into a thermal radiation source.

Figure 108.61 shows the experimental setup. About twenty laser beams in three cone angles are incident into a 600-μm-diam, 660-μm-long half-hohlraum. The side walls of the hohlraum are gold, usually 20 μm thick. The back wall is thin, ~1 μm of gold or 1 μm of gold overcoated with 1 μm of parylene. The high- and intermediate-angle beams are focused at the center of the laser entrance hole (LEH), but the low-angle beams are focused ~250 to 400 μm in front of the LEH to avoid hitting the back wall. An LPI probe beam is incident almost normal to the hohlraum axis and aimed to an interaction region,

which is the plasma that is 200 μm in front of the LEH. The transmission and forward scatter of this beam are measured with the temporally and spectrally resolved spectrometers and calorimeters in the full-aperture backscatter (FABS) diagnostic. Because of the laser-beam configuration on the OMEGA laser, one can use FABS to measure the forward-scattered light from opposing beams. If the beam is deflected, it falls onto the NBI plate. A time-averaged image of this deflection is recorded by the NBI camera. The L-band spectrometer views the plasma in the LEH region. The x-radiation emitted by the thin back wall can be used to heat a physics target. To characterize this source, the heating of a witness placed ~400 μm outside the back wall (Fig. 108.61) was measured.

Beam deflection is measured with the NBI plate. Figure 108.62 shows images of the NBI plate as a function of LPI

Figure 108.61
Experimental setup of a hot hohlraum experiment.

probe-beam intensity for two independent interaction beams. As the intensity increases, the beam deflection increases (the cross marks the center of the beam). The LPI beam is "bent" by the plasma flowing out of the target. Beam deflection occurs when the ponderomotively induced density depressions in the plasma move downstream and carry the light refracted into them. The images from NBI 25 and NBI 30 correspond to interaction beams B46 and B61, traversing the plasma at angles 31° and 9°, respectively, with respect to the normal to the axis of symmetry of the hohlraum. The beam deflections at 5×10^{15} W/cm^2 are approximately 15° and 7.2°, respectively. This is the first observation of beam deflection as a function of laser intensity for different optical paths along the plasma.

Understanding the measured LPI mechanisms depends on knowing the plasma parameters. Radiation-hydrodynamics codes are used to predict the plasma conditions. These must be benchmarked by measurements of n_e and T_e. In highly charged gold, the $3d \rightarrow 2p$ transitions of individual ionization states are separated by about 40 eV. If these lines can be resolved, the spectrum gives the distribution of the ionization states of gold. This, combined with models that predict the ionization state as a function of electron temperature, would give T_e.

The L-band spectrometer is designed to measure the $3d \rightarrow 2p$ transitions in gold with high resolution. It is a transmission crystal spectrometer mounted to a single-strip framing camera. It captures a single-time and space-resolved, high-resolution spectrum. Figure 108.63(a) shows a measured spectrum. There is a group of lines, peaking at 10,100 eV, with half-width of about 250 eV. Simulated spectra [Fig. 108.63(b)] from the nonlocal thermodynamic equilibrium (NLTE) code *FLYCHK* (for $\langle Z \rangle$ as a function of electron temperature) and *FLYSPEC* (for spectral lines) show similar features: a group of lines about 200 eV wide. The centroid moves to higher x-ray energy with higher electron temperature. A comparison of the data with simulation shows the measured electron temperature is ~7 to 8 keV.
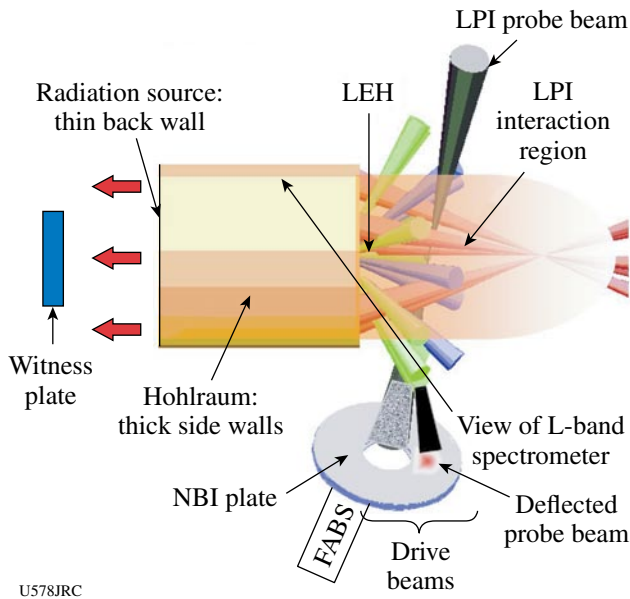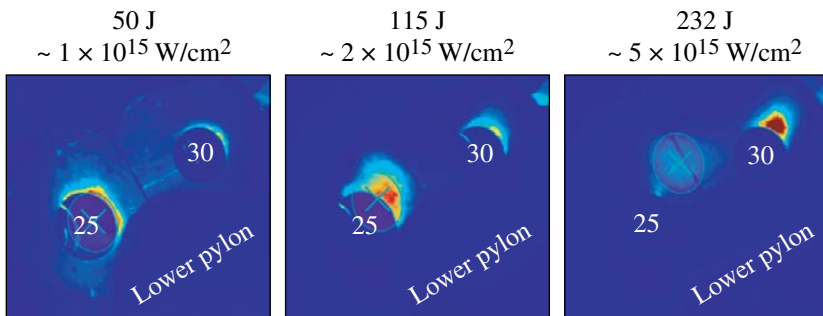
50 J
~ 1×10^{15} W/cm^2

115 J
~ 2×10^{15} W/cm^2

232 J
~ 5×10^{15} W/cm^2

Figure 108.62
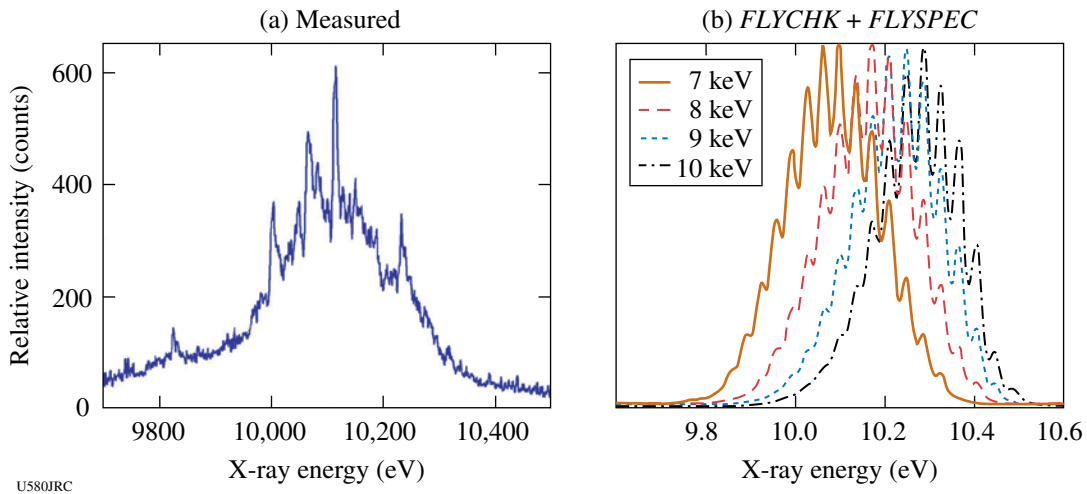Images of NBI plates show beam deflection as a function of LPI probe-beam intensity.

U579JRC

Figure 108.63

(a) L-band spectrometer measurement of $3d \rightarrow 2p$ transitions in Au. (b) Simulated spectra using the code *FLYCHK*.

Measured stimulated Brillouin forward scattering (SBFS) is shown in Fig. 108.64. The SBFS confirms the time at which the plasma reached the interaction region, by the transition from 3ω laser light to SBFS. The absence of 3ω light after 1 ns may indicate that the nonlinear beam deflection has shifted the beam toward the NBI plate, with the light missing the collecting lens. It is possible that the SBFS is *not* deflected because of its lower intensity.

The use of the back wall as a radiation source is demonstrated by using it to heat a Cr witness plate. The arrangement for the HTH half-hohlraum with a witness plate is shown in Fig. 108.65. Figure 108.65(a) shows a schematic of the target. The witness plate (WP) is mounted ~400 μm from the back wall, at an 11° tilt to the back wall so that the imaging diagnostic views the WP edge-on. The WP is a thin chromium foil
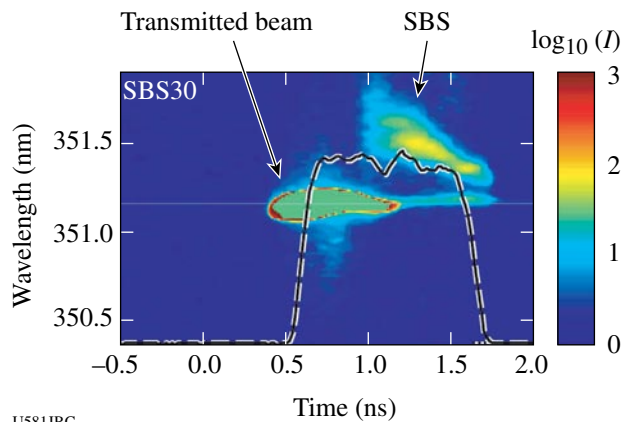
Figure 108.64
Streak camera image showing forward SBS.
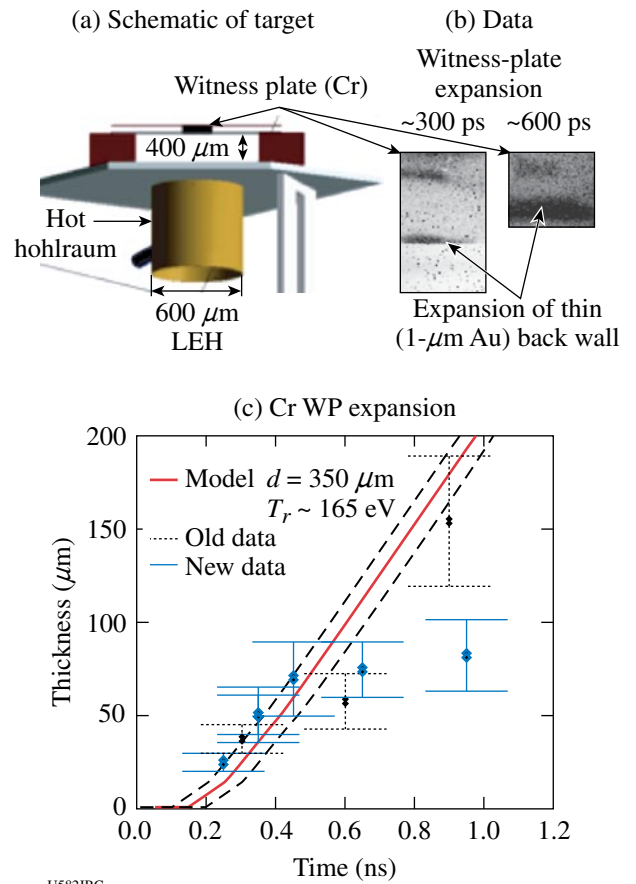
Figure 108.65
New radiation source: the thin back wall of an HTH half-hohlraum is used to heat a witness plate (WP). (a) The sketch of the target shows a WP mounted ~300 μm from the back wall at an 11° angle so it is viewed edge-on by the OMEGA diagnostic. (b) The data show a WP glowing after it has been heated by the back wall (also glowing). (c) The measured expansion of the Cr WP.

sandwiched in plastic (1 μm on each side). Figure 108.65(b) shows the heated WP at two different times. Since these were taken on two different shots, the distance of the WP from the back wall is slightly different; however, the WP is clearly expanding as it is heated. Figure 108.65(c) shows the measured width of the WP as a function of time from several shots on several different days. The solid line is the predicted expansion from a radiation–hydrodynamic simulation, assuming the WP is heated solely by radiation from the back wall. The data are consistent with the simulation, which predicts the radiation temperature in the plate to be ~165 eV.

The following additional measurements of plasma parameters in the LPI region have been performed: (a) the M-shell spectra of gold, (b) Raman backscatter, and (c) 2ω and 4ω Thomson scattering. These data are still being analyzed.

Experimental Astrophysics on the OMEGA Laser
Principal Investigator: R. P. Drake (University of Michigan)
Co-investigators: B. A. Remington, H. F. Robey, S. G. Glendinning, D. D. Ryutov, M. Herrmann, A. R. Miles, A. J. MacKinnon, B. E. Blue, and J. F. Hansen (LLNL); M. Koenig (LULI, Ecole Polytechnique, France); D. Arnett (University of Arizona); R. Rosner and T. Plewa (University of Chicago); J. Stone (Princeton University); S. Bouquet (CEA, France); J. P. Knauer and T. R. Boehly (LLE); Y. Zhang and J. Glimm (SUNY Stony Brook)

The OMEGA laser can address important issues in astrophysics because, through laser ablation, it can produce pressures of tens of Mbars over areas of square millimeters. Two such issues are the contribution of hydrodynamic instabilities to the structure in supernovae and the dynamics of radiative shock waves. After successfully creating collapsed radiative shock structures in both argon and xenon gas, an experiment was performed to Thomson-scatter light from the 4ω beam off of a shock front in argon gas.

In the experiment, ten smoothed beams of the OMEGA laser irradiate a 20-μm beryllium disk with UV light at an irradiance of ~5×10^{14} W/cm^2 for 1 ns. This launches the disk via ablation pressure at a high velocity into a 600-μm-diam, 6-mm-long polyimide tube filled with 1.1 atm (0.001 g/cm^3) of argon gas. This target had openings covered with 3000-Å polyimide facing the 4ω probe beam and the UV spectrometer and streak camera in TIM-2. The scattering volume was 3.7 mm from the initial drive disk position. The 4ω probe beam fired in a 2-ns pulse at 200 J, with a best-focus spot size of 100 μm. The target axis for this experiment was parallel to the probed ion-acoustic waves.

Figure 108.66 shows spectral data from the first experiments to obtain Thomson-scattering data from a shock front. The signal lasted 300 ps, starting at 20.1 ns after the drive beams turned on. Before that, the signal was from the tail end of a destroyer beam blasting off the polyimide cover facing the collection diagnostic in TIM-2. The spectrum of the scattered light and a fit to the data are shown in Fig. 108.67. The overall spectrum is shifted in frequency by a Doppler shift, implying that the flow velocity of the shocked fluid is 110 km/s. Fits to the spectrum using the kinetic theory of Thomson scattering, combined with an evaluation of the average charge using an "average atom" model, give an ion temperature of 300 eV, an electron temperature of 250 eV, and an average charge of 13.7. These are sensible values for the argon near the shock front.

Astrophysical Jets and HED Laboratory Astrophysics
Principal Investigator: P. Hartigan (Rice University)

A variety of objects in the universe are surrounded by accreting disks of matter, and most of these systems drive highly collimated supersonic jets out the poles of these disks. Examples include jets from young stars, planetary nebulae, x-ray binaries, and black holes at the centers of active galaxies. The goal of this
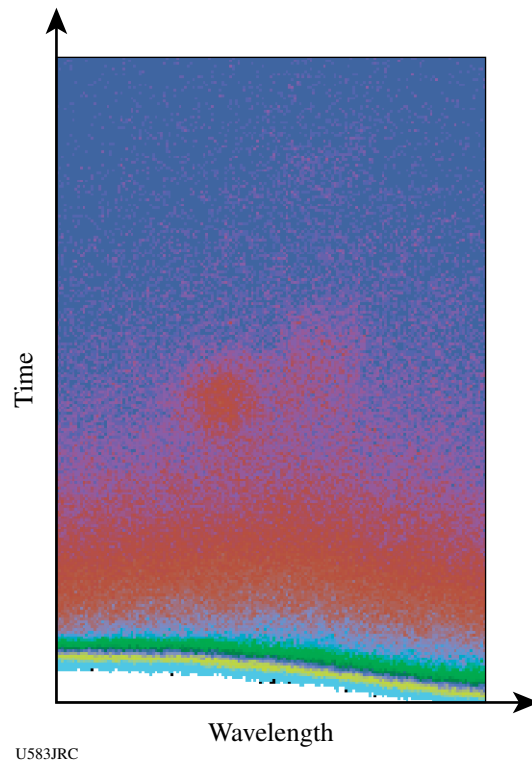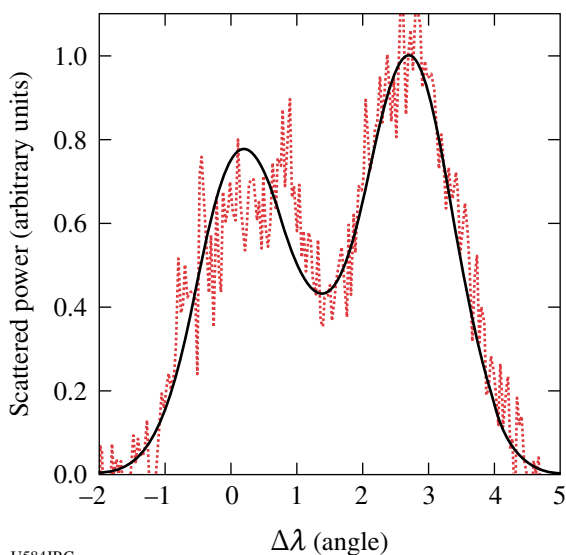

U583JRC

Figure 108.66
Streak camera data showing Thomson-scattered-light spectral evolution for collapsed radiative shock.

Figure 108.67
Thomson-scattered spectrum and fit to the data for Fig. 108.66.

project is to create laboratory analogs of the jet phenomenon in the laboratory and follow what happens when such a jet interacts with an obstacle in the flow as it is observed to do in many astrophysical situations. An astrophysics fluid dynamics code (*AstroBEAR*) and the *RAGE* code at Los Alamos are both used to help design the experiment and interpret the results.

In the past year, two shot days were allotted for the project, and both succeeded in producing excellent images of shocks in the jet and the ball as the latter was being destroyed and entrained by the flow. The targets consisted of a dense ball

embedded at various offset distances (impact parameters) from the axis of the jet. The data set now includes a continuous range of impact parameters and times so we can follow the process as a function of these two variables. Sample images from the experiment are shown in the Fig. 108.68. Astrophysical observations of a deflected jet are scheduled for the end of November, and we will be comparing the new spectra from that effort with numerical datacubes of the *RAGE* and *AstroBEAR* simulations of the laser experiments to improve our understanding of the dynamics of these flows.

Recreating Planetary Core Conditions on OMEGA
Principal Investigator: R. Jeanloz (University of California, Berkeley)

Significant technical as well as scientific breakthroughs in the NLUF high-pressure experiments on planetary fluids were made this past year. The approach that is used involves driving a laser-induced shock wave through a sample already precompressed in a diamond-anvil cell (Fig. 108.69). This combines the benefits of static and dynamic methods of high-pressure experiments, allowing the final pressure–volume–temperature (P–V–T) state of the sample to be tuned across a broad range of thermodynamic conditions (Fig. 108.70). In fact, much-higher compressions, thus more-extreme interatomic interactions, are achieved through this approach than through traditional shock-wave (Hugoniot) measurements.

One of the major technical accomplishments of this program has been the significant improvement of the understanding of
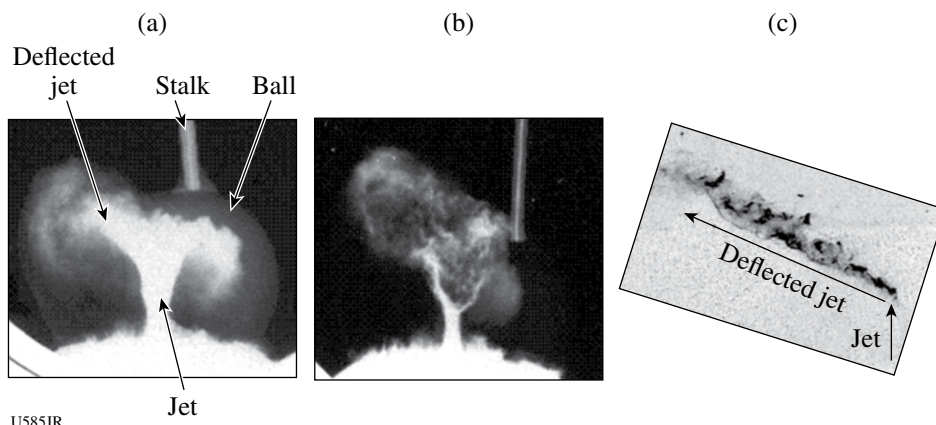
Figure 108.68
Deflected jets in the laboratory and in the universe. (a) OMEGA image of a jet deflecting from a ball located 300 μm from the axis of the jet, at 150 ns, taken with an Fe backlighter. Shocks are clearly visible in the ball and ahead of the deflected jet, which is starting to fragment. (b) Same as (a) with a 350-μm offset at 200 ns and a Zn backlighter. (c) Hubble Space Telescope image of the deflected jet HH 110. The jet emerges from a young star off the bottom of the image and deflects off an opaque dark cloud of gas and dust.

the interferometry records obtained from the shock experiments (Fig. 108.71). Despite the use of antireflection coatings, the components in these experiments generate residual reflections that cause "ghost fringes" to appear in the VISAR records. This source of noise is now understood, to the point that the "ghost fringes" serve as internal calibrants for the records and a joint inversion of the records can be performed to obtain far better velocity resolution than previously thought possible.

In addition to equation-of-state measurements, one of the key measurements obtained from the VISAR records is the optical reflectivity of the shock front: it is possible to determine whether one is looking through the shock front or off its surface

by the way the velocity fringes. The reflectivity at optical wavelengths can be converted to an equivalent of electrical conductivity, allowing us to determine the competing *P–T* conditions under which helium becomes metallic (Fig. 108.72). This is important because the metallization conditions for helium, far more extreme than those for hydrogen, determine the depths at which hydrogen and helium—the primary constituents of giant planets—can behave as metallic alloys. Without such alloying, it is expected that helium separates from the much lighter hydrogen, and the gravitational energy released by this "differentiation" process is thought to be a major source of heat and internal evolution of giant-planetary interiors. Indeed, experiments now underway will allow the documentation of the enhanced reflectivity of hydrogen + helium mixtures (Fig. 108.73), promising to offer significant new constraints on models of planetary evolution and origins.

(a)

(b)

Figure 108.69
Photograph of (a) a loaded diamond cell subjected to laser-shock compression and (b) schematic cross section of the diamond cell. The diamond anvil of the entry (drive-laser) side must be thin in order to minimize attenuation of the shock front before it enters the sample. Diagnostics include velocity interferometry (using VISAR) as well as pyrometry (not shown).
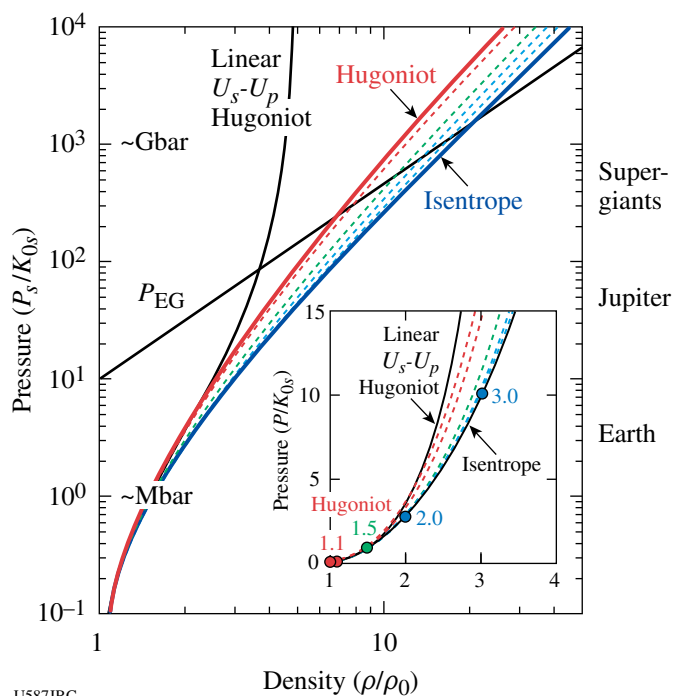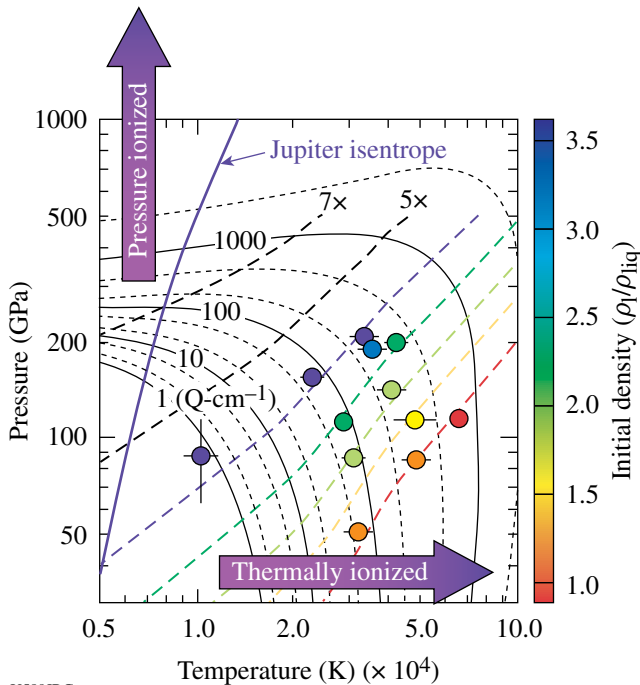

Figure 108.70
Pressure–density (*P–ρ*) equations of state, normalized by the zero-pressure bulk modulus (*K*) and density illustrating the range of conditions that can be achieved between the single-shock Hugoniot and isentrope as a function of precompression by factors of 1.1, 1.5, 2.0, and 3.0 (see inset), all calculated from the Birch–Murnaghan[4] and Mie–Grüneisen[5] approaches assuming $K'_0 = 4$, a Grüneisen parameter varying as $\gamma/\rho = $ constant, and $\gamma_0 = 1.5$ (subscripts 0 and *s* indicate zero-pressure and isentropic conditions, respectively). The linear shock-velocity U_s versus particle-velocity U_p relationship, and the density dependence of the ideal electron–gas pressure (P_{EG}) are shown for comparison, as are Mbar and Gbar pressures and planetary-center conditions (Earth, Jupiter, and supergiants) corresponding to a typical bulk-modulus value of 100 GPa (= 1 Mbar). The inset shows the lower-pressure range on a linear plot.
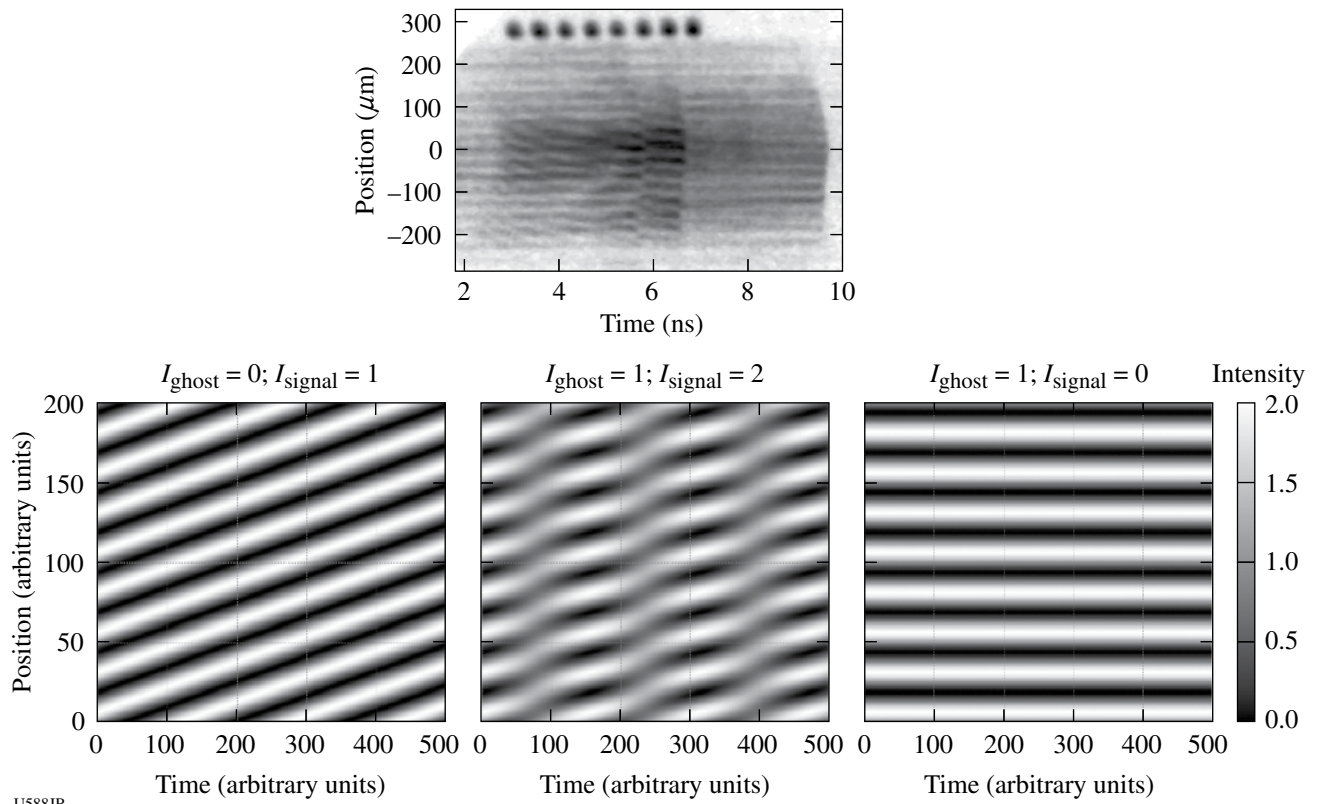
U588JR

Figure 108.71

(Top) Velocity-interferometry (using VISAR) record from a laser-shock experiment on precompressed helium showing the presence of "ghost fringes" due to residual reflections from diamond and other surfaces. (Bottom) Simulations of the ghost fringes, from 100% signal (no ghost) on the left to 100% ghost (no signal) on the right; center panel shows a 2:1 intensity ratio for signal:ghost.

U589JRC

Figure 108.72

Reflectivity measurements as a function of pressure–temperature conditions achieved in helium (circles shaded according to the precompressed density ρ_1 prior to shock loading) quantified in terms of equivalent electrical conductivity (solid and dotted contours). The data clearly probe the trade-offs between pressure and temperature in causing metallization (ionization), with predicted trajectories for different amounts of precompression indicated by the dashed lines and the model temperature distribution (isentrope) inside Jupiter shown for comparison.
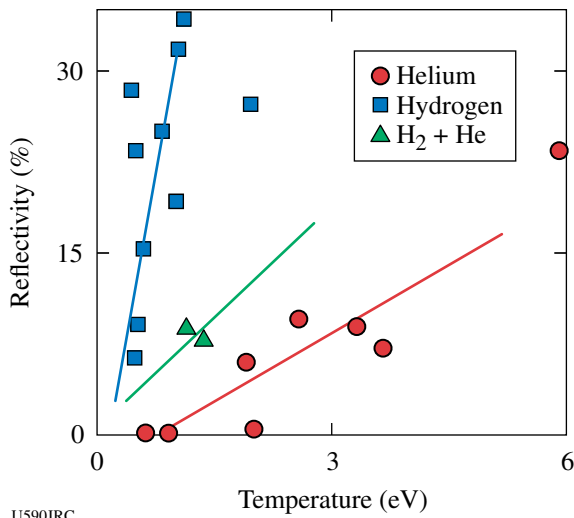
Figure 108.73
High-pressure reflectivity of hydrogen, helium, and hydrogen + helium mixtures under shock compression, shown as a function of Hugoniot temperature determined from pyrometry.

Three-Dimensional Study of the Spatial Structure of Direct-Drive Implosion Cores on OMEGA
Principal Investigator: R. Mancini (University of Nevada, Reno)

The objective of this project is to study the three-dimensional (3-D) structure of the temperature and density spatial profiles of OMEGA direct-drive implosion cores using data from gated narrowband x-ray core images recorded along three quasi-orthogonal directions. To this end, this experiment uses plastic shell targets filled with deuterium gas and a tracer amount of argon for spectroscopic diagnostic purposes. Three identical multimonochromatic imagers (MMI) have been designed, built, and fielded on OMEGA implosion experiments to perform observations along the lines of sight (LOS) of TIM-2, TIM-3, and TIM-4; this set of TIM's represents a quasi-orthogonal system of x-y-z Cartesian axes. The implosions were driven with 60 OMEGA beams, 23 kJ of UV energy, and a 1-ns square laser pulse. At the collapse of the implosion, the hot and dense core plasma achieved temperatures in the 1- to 1.5-keV range and electron number densities in the 1×10^{24} cm^{-3} to 2×10^{24} cm^{-3} range. X-ray K-shell line emission from the argon dopant is a suitable spectroscopy diagnostic for this temperature and density range.

Core images (recorded by MMI instruments) that are formed by a large array of 10-μm-diam pinholes and reflected off a depth-graded WB$_4$C multilayer mirror with an average bilayer thickness of 15 Å yield narrowband x-ray images in the photon energy range from 3 to 5 keV. They have a magnification of 8.5,

provide spatial resolution of approximately 10 μm, and record gated (framed) images characteristic of a 50-ps time interval. Indeed, these instruments record data with simultaneous space, time, and photon energy resolution. As an illustration of the data recorded by MMI, Figs. 108.74 and 108.75 display a time history of narrowband x-ray core images from OMEGA shot 42643 at the collapse of the implosion, based on the argon Ly$_\beta$ ($1s$ ^2S–$3p$ ^2P, $h\nu$ = 3936 eV) and He$_\beta$ ($1s^2$ ^1S–$1s2p$ ^1P, $h\nu$ = 3684 eV) line emissions. The photon energy narrowband of these images is given by the (mainly) Stark-broadening widths of the line shapes, which for the plasma conditions of these cores is 60 to 70 eV. Core dimensions are in the 60- to 100-μm range. At early times, images recorded along both quasi-orthogonal directions show cores that are large and mostly round. For later times, one LOS shows a core shape that evolves into an oval shape, while the other LOS shows an object that remains more rounded but
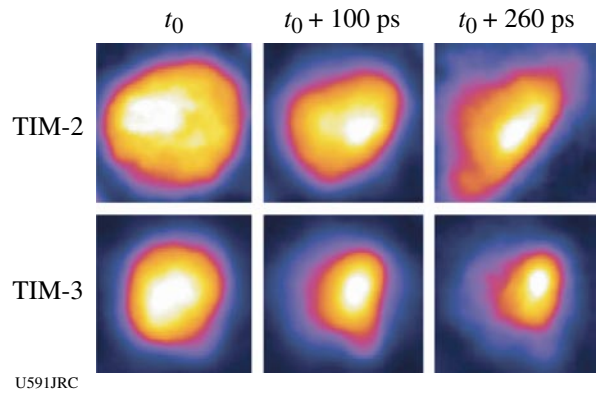

Figure 108.74
Gated argon Ly$_\beta$ narrowband core images recorded along two quasi-orthogonal directions on OMEGA shot 42643.

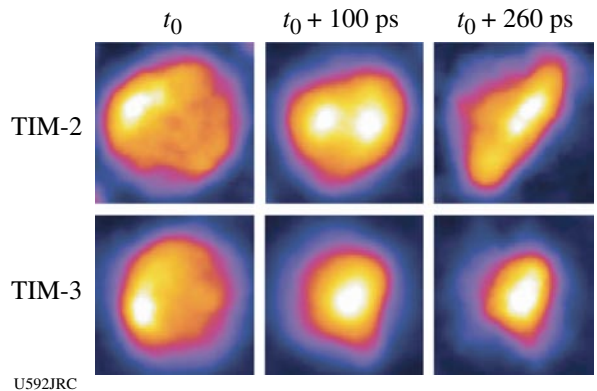

Figure 108.75
Gated argon He$_\beta$ narrowband core images recorded along two quasi-orthogonal directions on OMEGA shot 42643.

getting smaller. Both observations suggest the evolution of a 3-D core from rounded to ellipsoidal shapes with a well-defined orientation in space. It is also interesting to observe the regions of greatest brightness associated with the Ly_β and He_β line emissions, which depends on both temperature and density conditions in the core. Detailed spectral modeling and analysis of the emissivity and opacity of the argon x-ray emission permit a reconstruction of spatial structure of the plasma. In this connection, Fig. 108.76 displays a temperature map based on the analysis of the second frame of data (i.e., $t_0 + 100$ ps) displayed in Figs. 108.74 and 180.75. The range of values of this spatial profile is consistent with the range of temperatures extracted from the analysis of data independently recorded with streaked spectrometers in the same experiment. Several analysis methods are currently being investigated that simultaneously consider data observed along several LOS's.
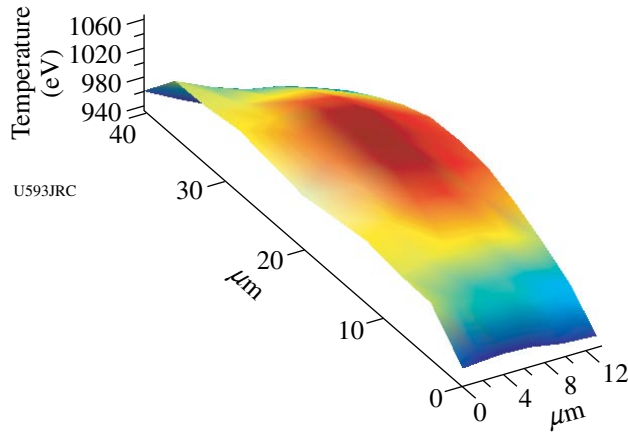
Figure 108.76
Core temperature map for OMEGA shot 42643 extracted from TIM-2 data in Figs. 108.74 and 108.75 for $t_0 + 100$ ps.

Implosion Dynamics and Symmetry from Proton Imaging, Spectrometry, and Temporal Measurements

Principal Investigators: R. D. Petrasso and C. K. Li (Massachusetts Institute of Technology)

As part of the MIT NLUF program, data was taken in an ongoing series of experiments using proton radiography to study transient E and B fields generated by the interaction of OMEGA laser beams with plastic foils. High-resolution, time-gated radiography images of a plastic foil driven by a 10^{14}-W/cm^2 laser implied B fields of ~0.5 MG and E fields of ~1.5×10^8 V/m. Simulations of these experiments with *LASNEX + LSP* have been performed and are in overall (though not exact) agreement with the data both for field strengths and for spatial distributions; this is the first direct experimental test of the laser-generated B-field package in *LASNEX*. The experiments also demonstrated that laser phase plates substantially reduce medium-scale chaotic field structure. The results have recently been published in *Physical Review Letters*[6] and in *Review of Scientific Instruments*.[7]

In each experiment, two plastic foils were illuminated by a single OMEGA laser beam, and a projection radiograph was made of each foil using a backlighter providing monoenergetic 14.7-MeV protons and a CR-39 area detector for image recording. One foil was perpendicular to the backlighter–detector direction, giving a face-on view of the resultant field structure, while the other foil was parallel to the backlighter–detector direction, giving a side-on view. The backlighter was formed by imploding a D^{3}He-filled, glass-shell capsule with 20 OMEGA laser beams (see Fig. 108.77). Since the burn duration of the D^{3}He implosion was short (~150 ps) relative to the 1-ns duration of the foil illumination, and the relative timing of the implosion and the foil illumination was adjustable, it was possible to record images at different times relative to the foil illumination.
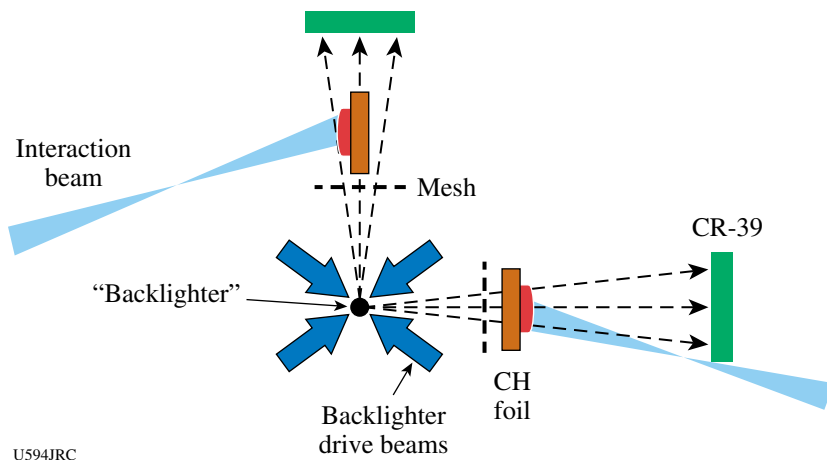

Figure 108.77
Schematic illustration of experimental setup and the physical relationship between the proton backlighter (imploded D^{3}He-filled capsule), mesh, CH foils, CR-39 imaging detectors, and OMEGA laser beams. The distances of components from backlighter were 0.8 cm for mesh, 1 cm for foil, and 36 cm for detector. The hole-to-hole spacing in the mesh was 150 μm.

The distortion in the mesh pattern at the detector shows how the proton trajectories were deflected through interaction with the fields generated by laser–plasma interaction at the foil. Sample images recorded at different times are shown in Fig. 108.78 (face-on) and Fig. 108.79 (side-on). These images have been analyzed in collaboration with LLNL and LLE to provide information about the time evolution of the field-induced distortion.[6,7]
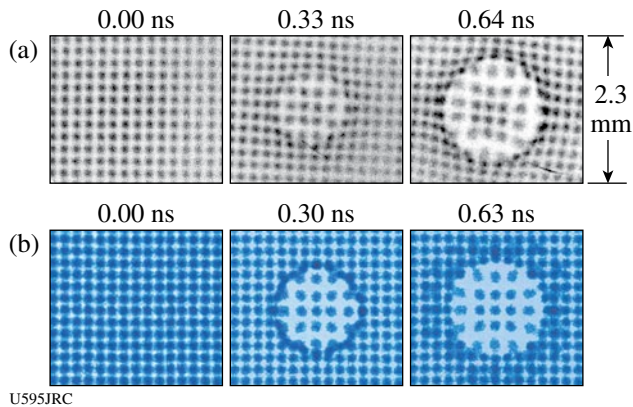

Figure 108.78

(a) Measured face-on D^{3}He proton images showing the effects of the *B* field generated by laser–plasma interactions at 0.0, 0.33, and 0.64 ns, respectively, after the interaction beam was turned on. The labeled dimensions of the image are scaled to the location of the foil. (b) Images simulated by *LASNEX + LSP* for the conditions that produced the experimental images shown in (a).
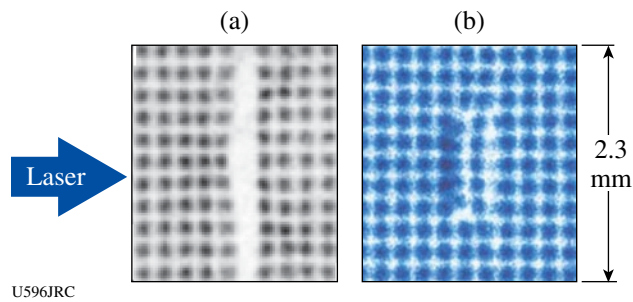
Figure 108.79

(a) Data and (b) simulation for the side-on images. The distortion in the center column of (a) resulted from the *E* field. The large separation between the two center columns of beamlets in (a) is due to attenuation by the CH foil, which is 50 μm thick but 3 mm long in the direction parallel to the proton trajectories; this effect is not seen in (b) because proton–foil interactions were not modeled in the *LSP* simulation.

FY06 LLNL OMEGA Experimental Programs

In FY06 LLNL led 354 shots on the OMEGA system. This total represents a shot rate of approximately 4% higher than nominal (340 shots scheduled for the year), an excellent achievement when one considers that LLNL's programmatic needs frequently dictated difficult reconfigurations from one day to the next, especially during split days.

National Ignition Campaign (NIC) Experiments: One of the first experiments of the year was designed to examine the direct effects of laser-heated gas on an implosion capsule within a gas-filled hohlraum. Plastic hohlraums (to minimize radiation drive) and foam witness balls were used in a NIF-foot-scale experiment. The x-ray backlighting data are shown in Fig. 108.80. Arrows point to regions where there is a departure from spherical symmetry due to pressure from the laser-heated gas that filled the hohlraum.

Several shot days were devoted to the study of collective x-ray scattering from plasmons in warm (10 to 15 eV), dense (2 to 3 $\times$ 10^{23} electrons/cm^3) matter. By fitting the data to theoretical models, the electron density is obtained from the scattered x-ray data and found to be in agreement with simulations.

Throughout FY06 a number of laser–plasma interaction experiments were carried out, some in collaboration with CEA, using a gas-filled hohlraum arranged so that one OMEGA beam (beam 30) could be used as an on-axis probe. Spatially imaged Thomson scattering and a time-resolved transmitted beam diagnostic (3ω TBD) were successfully fielded on OMEGA. Various experimental results are shown in Fig. 108.81 (electron and ion temperatures in the gas as a function of time), Fig. 108.82 (Brillouin scattering reduced as electron temperature increases), and Fig. 108.83 (Raman scattering measured as a function of density for fixed intensity). Experiments using a defocused beam with phase plates showed interaction instabilities decreasing with the average intensity, as predicted. Finally, a semiautomated mechanism for calibration of the near-backscatter plate was fielded and tested.[8]

An albedo (ratio of radiant energy emitted divided by radiant energy absorbed) experiment compared gold hohlraums and "cocktail" (mixtures of gold and uranium) 180-eV hohlraums and found, as predicted, a slight increase for the cocktail case.

In another collaboration with CEA, the OMEGA laser was used in the direct-drive configuration to illuminate spheres of gold, uranium, and a cocktail mixture to measure the conversion of laser energy into x-ray energy. Particular attention was given to obtaining detailed measurements in the 2- to 5-keV range.

An extensive series of experiments were performed for platform development, and use of that platform, for measuring the
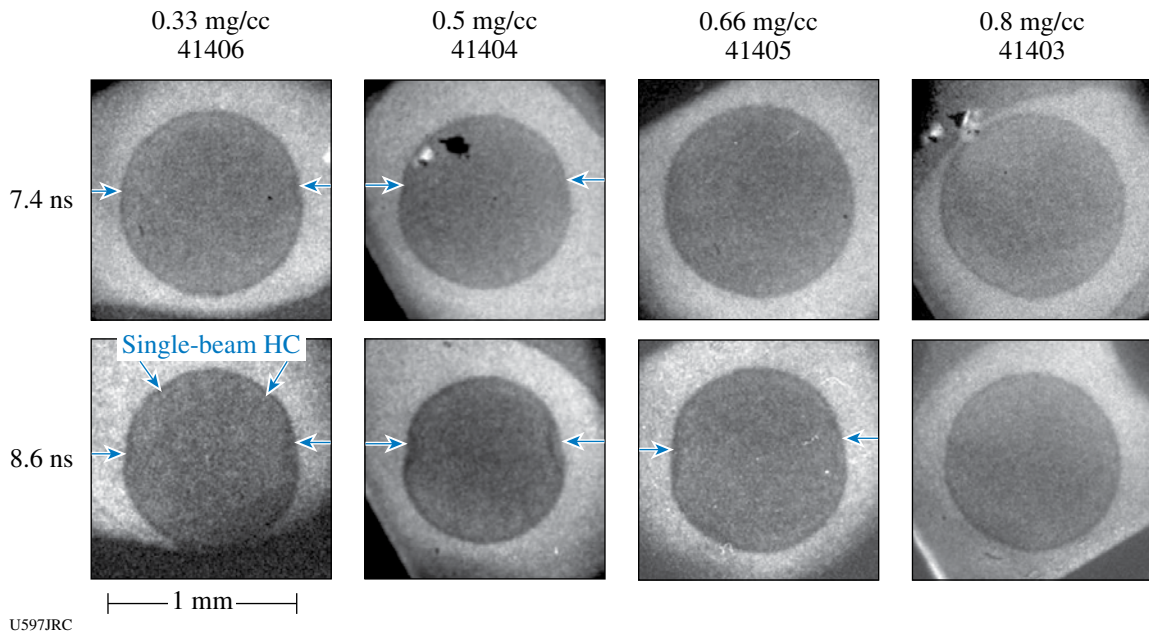
Figure 108.80
X-ray-backlit images of foam spheres, showing (arrows) effects of pressure from laser-heated hohlraum fill gas. Good backlighting foam-ball data were measured for the 0.3- to 0.8-mg/cc hohlraum fill range of interest for HC.
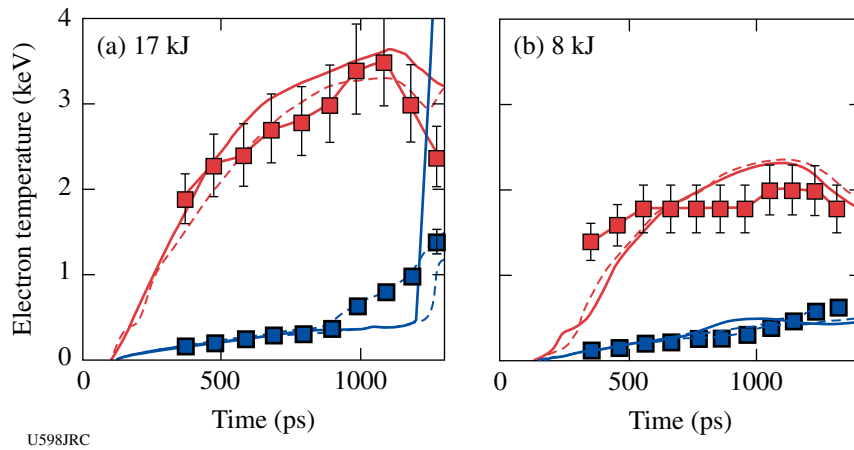

Figure 108.81
Electron temperature (open squares), ion temperature (dark squares), and simulations (solid lines) as a function of time along the laser beam path. The measured electron- and ion-temperature evolution validates the simulations of the plasma conditions along the interaction beam path.

Rayleigh–Taylor growth of ablator materials, being ablatively accelerated by x-ray drive. The planar ablator samples were mounted on the end of a one-ended hohlraum ("halfraum"). X-ray backlighting of the planar samples was used in both side-on and face-on geometry. The latter required imaging through the halfraum. Side-on images were obtained with both 2-D framing cameras and 1-D streak cameras, depending on the experiment. One goal is to be able to measure RT growth in Be from its inherent grain structure; this requires that the platform be capable of nearly 1000× growth, to increase the structure to observable size and simulate expected NIF conditions. Figure 108.84 shows face-on data for two materials, Be and diamond. The initially imposed 1-D perturbations have grown to measurable size. Figure 108.85 shows a summary of these results for diamond. Analysis and simulations are still ongoing to form a more complete understanding of the processes.

U599JRC

Figure 108.82
Measured SBS reflectivity (points) follows linear gain calculation (solid line) and drops with electron temperature, as predicted. Stimulated Brillouin scattering is reduced to zero for electron temperatures above 2.5 keV.

U600JRC
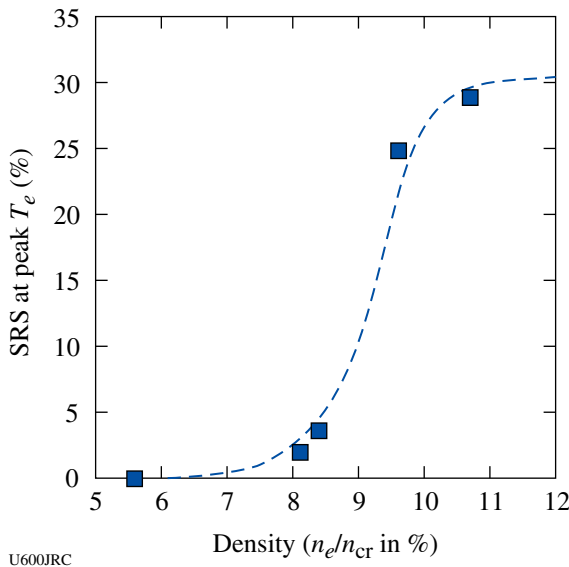
Figure 108.83
Density scaling of SRS at an intensity of 1.5×10^{15} W/cm^{-2}. Raman-scattering levels are consistent with linear gain calculations, varying with electron density for fixed laser intensity.
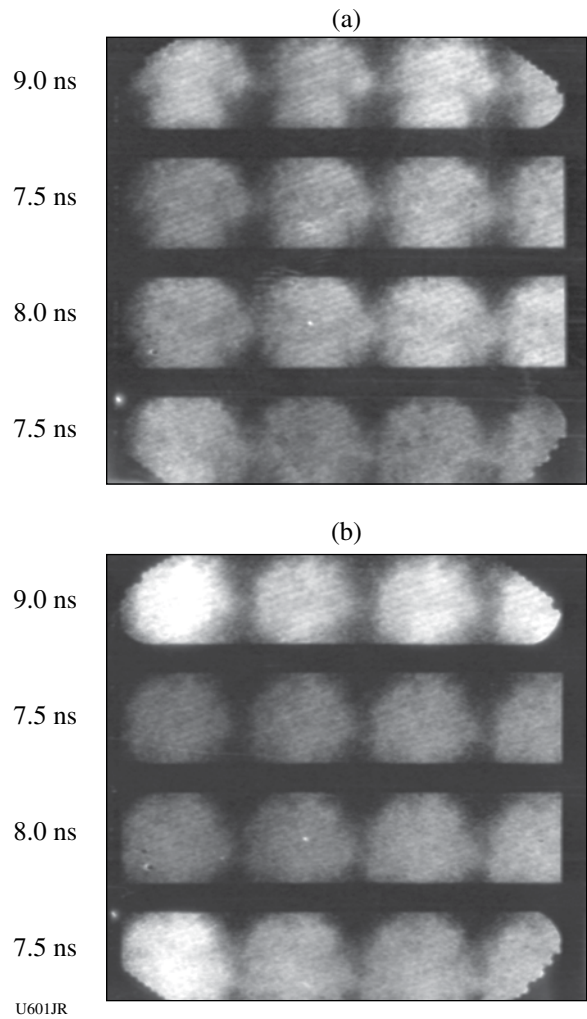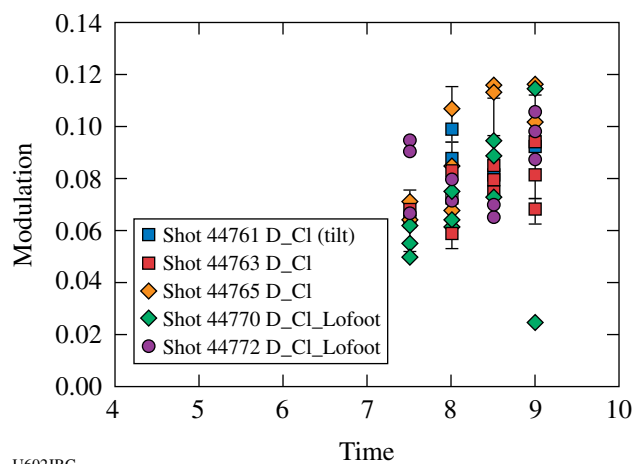

U601JR

Figure 108.84
X-ray-backlit images of ablatively accelerated planar foils. Observation of large growth of 150-nm amplitude initial perturbations demonstrated (lines running diagonally lower left to upper right) for both (a) carbon (diamond) and (b) Be ablators, as expected, based on previous CH(Ge) results.
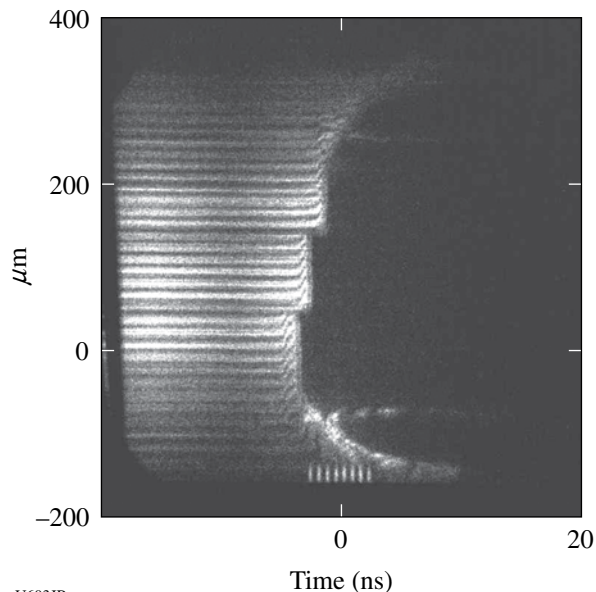
Figure 108.85
Modulation depth for diamond foils (see Fig. 108.84) for various times and laser drives.

Figure 108.86
ASBO data: shocks in Be driven by x rays from window. The abrupt turnoff of the reflected light (fringes) coincides with the time of shock breakout from the three different thicknesses of Be (thinnest at bottom).

A concern with gas-filled hohlraums is that they must, of necessity, have a window to contain the gas. Despite the fact that these windows are thin and low Z, they are the first objects irradiated by the laser beams, and they can generate x rays that may affect the capsule. To obtain quantitative data, Be step wedges (planar Be samples with three different thicknesses) were exposed to x rays produced by the interaction of the OMEGA laser with a thin plastic window. The resulting shock and preheating of the Be were measured with the active shock breakout (ASBO) diagnostic. An example of such data is shown in Fig. 108.86. The termination of the fringes (time runs left to right) coincides with the shock breaking out of the rear surface of the three steps (thickest step at top). Still other experiments used the ASBO, VISAR, and streaked optical pyrometer (SOP) to infer changes in the state—specifically, melting points—of Be and diamond, under varying levels of x-ray preheat and shock compression.

A series of implosion experiments modeled NIF fill tubes with a deliberately placed perturbation on the surface of the capsule. The inner layer of the capsule contained a mid-Z (Ti) dopant. Under certain conditions, the perturbation resulted in a hydrodynamic jet of material moving through the imploded core. This jet was detected by the x-ray emission from the Ti dopant. While this experiment looked at the effect of the tube above the capsule, another experiment ("planar fill tube"), done in collaboration with LANL, investigated the effect of the fill hole using a planar analog. Initial experiments gave promising results using foams as a stand-in for solid DT and showed a jet of the indirectly driven ablator material propagating through the hole.

One design for x-ray backlighters on the NIF looks like a peaked roof. Several OMEGA shots were carried out with this geometry to ascertain the x-ray conversion efficiency, and also the spatial uniformity, of this design. The results showed these targets capable of meeting the NIF specifications.

High-Energy-Density Science (HEDS) Experiments: Approximately one third of the LLNL OMEGA shots were for HEDS experiments.

One experiment used very small hohlraums to generate a thermal source of x rays at high photon energies, while at the same time examining the laser–plasma interaction issues associated with such targets. Figure 108.87 shows the x-ray spectra from the 10-keV region, along with model calculations for various thermal temperatures.

Late in FY06 LLNL executed a day of experiments using "double-shell" targets. This represented the culmination of extensive target fabrication work; x-ray tomographic images of the targets are shown in Fig. 108.88. The experiment used a variety of diagnostics, such as time-resolved x-ray backlighting, shown in Fig. 108.89. These data are now undergoing detailed analysis.

The nonlocal thermodynamic equilibrium (NLTE) experiments have as their goal the study and understanding of the radiative effects of high-Z (atomic number) dopants on implosions. Capsules containing deuterium, plus dopant gas, were directly driven by the OMEGA laser. Both spectroscopic x-ray and nuclear diagnostics were employed. Figure 108.90 shows the dramatic order-of-magnitude change in secondary neutrons (those arising as a result of tritium being generated in primary

nuclear fusion reactions) observed when a small amount of xenon is added. This is indicative of higher densities in the imploded fuel as a result of radiative cooling from the xenon.

Several experiments were carried out to prove the concept of an experimental platform for measuring x-ray opacities in warm, dense matter. These included the development of broadband soft-x-ray backlighters, point backlighters at higher energies, and a hohlraum drive to heat the samples to the desired conditions, along with the necessary diagnostics. These experiments will continue into FY07.

Dynamic hohlraums are directly driven, capsule-within-a-capsule targets. The idea is shown in Fig. 108.91; xenon gas within the outer capsule becomes hot and radiates, causing an x-ray-driven implosion of the inner, deuterium-containing capsule. Data obtained include x-ray-streaked images of the self-emitted x rays, multiple x-ray images, charged-particle information (collaboration with MIT), and multiple standard OMEGA neutron diagnostics. These data are currently being analyzed and compared with simulations.

We continued with our ICE (isentropic compression experiments) in FY06. Various improvements were made to targets, to increase planarity and temporal behavior of the shockless drive. Equation-of-state data were obtained for various materials.

The "shock-sphere" experiment conducted on OMEGA is an example of laboratory astrophysics. In this case, it is model-
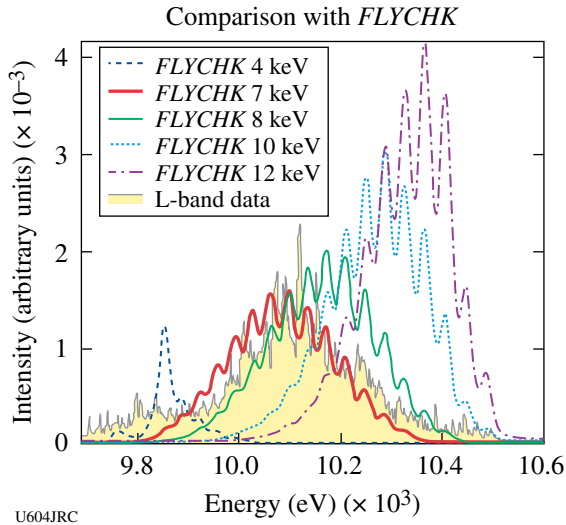

Figure 108.87
Spectroscopic data (gray, shaded area) from small, high-temperature hohlraum are best fit by model calculations (*FLYCHK*) between 7 and 8 keV (between thick and thin solid curves).
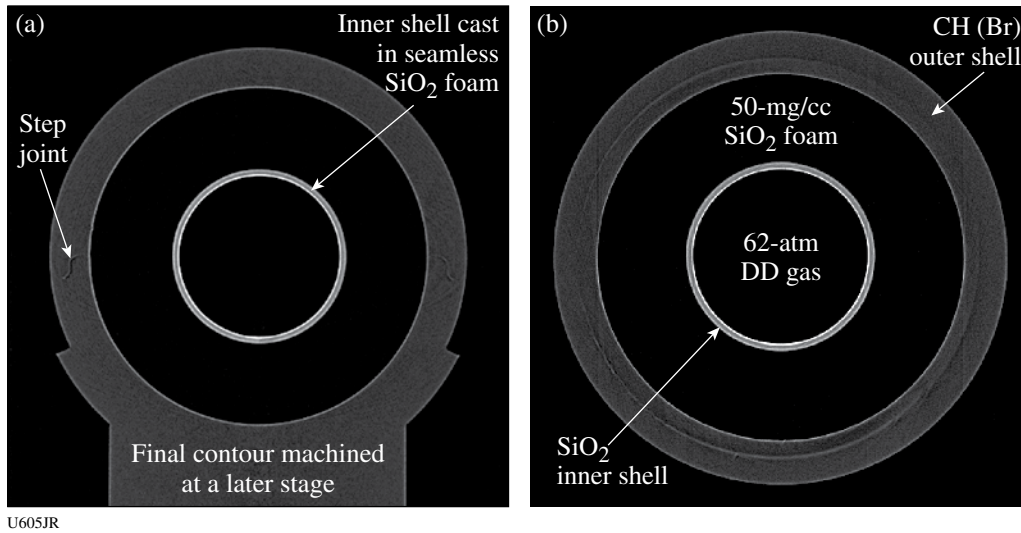

Figure 108.88
SiO$_2$ double-shell implosions. 3-D tomography of each double-shell capsule was performed to verify that all capsules meet all required specifications.
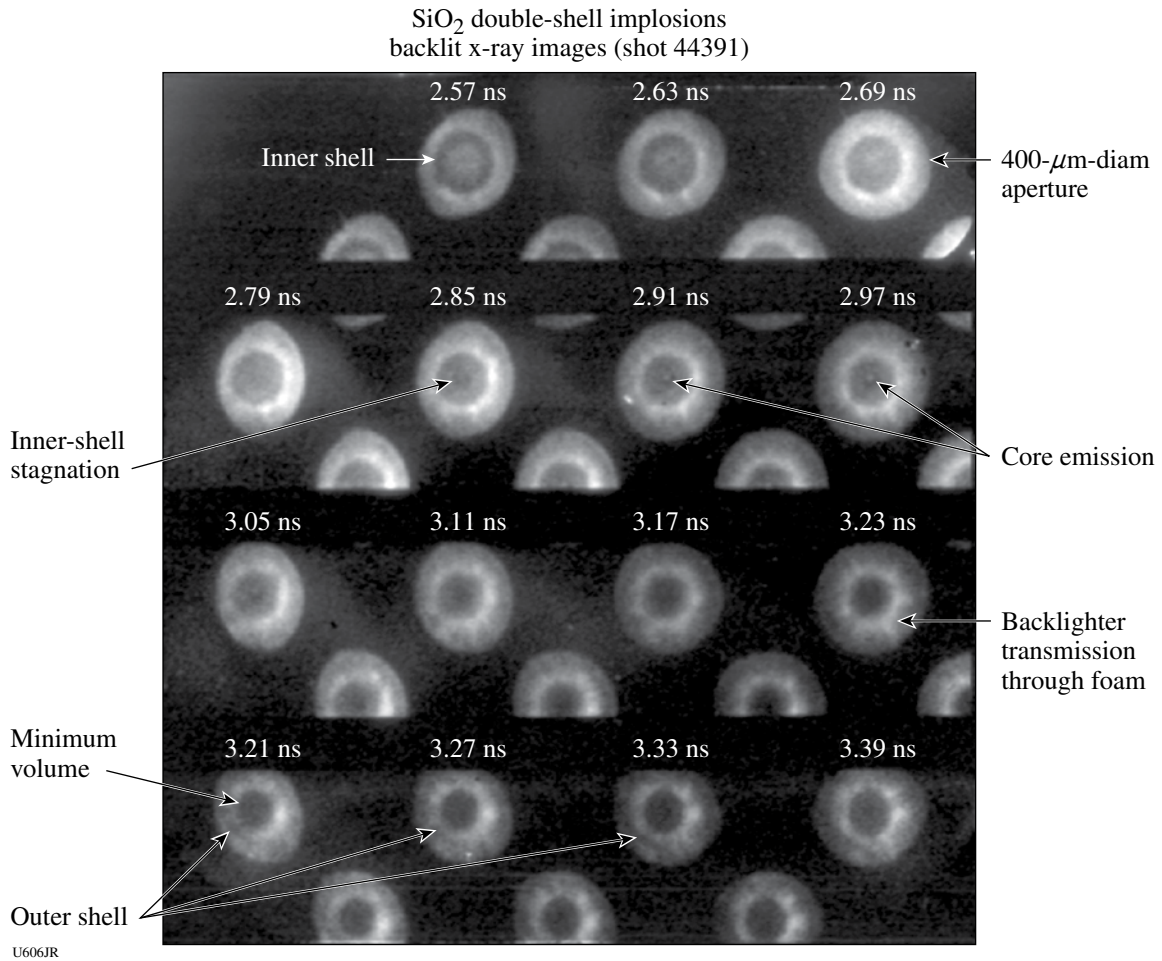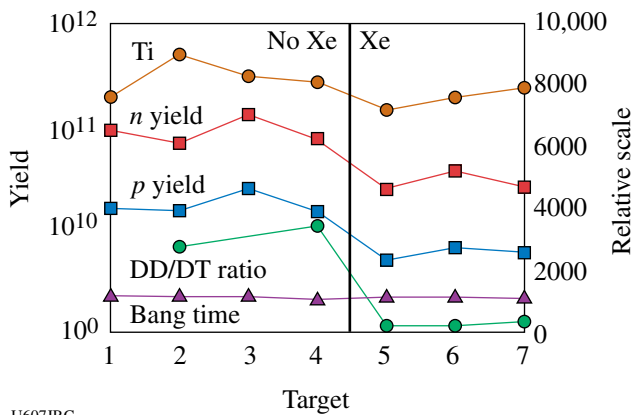
SiO$_2$ double-shell implosions
backlit x-ray images (shot 44391)

Figure 108.89
Example of backlit x-ray images obtained from double-shell experiments.

Figure 108.90
Addition of Xe has a significant impact on implosion parameters in NLTE experiments, as shown by neutron data. Note the order-of-magnitude change in DT (secondary) neutrons, due to the radiative cooling by xenon atoms.
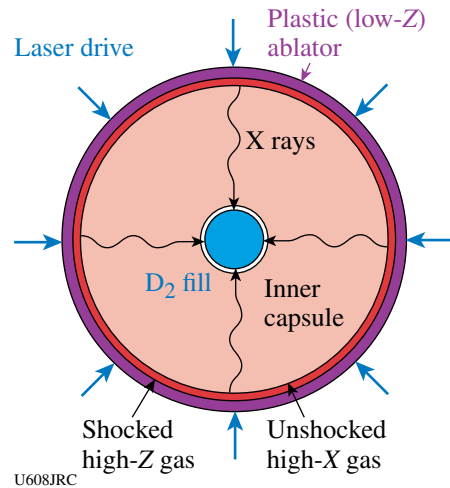
Figure 108.91
Concept of "dynamic hohlraum;" Xe gas between shells produces x rays that ablatively implode inner shell.

ing the passage of a shock in low-density material past denser spherical objects and examining how the shock passage induces mixing of material into the interstellar medium. Figure 108.92 shows an example of the data. The laser-generated shock is moving toward the lower left, past the two spherical objects. (The grid is for diagnostic reference.) X-ray backlighting provides images at various times. On the right (at 12 ns) the shock is still visible, just to the right of the spheres. These data are being used to benchmark model calculations, which will then be applied to astronomical observations for comparison.

Another experiment looked at the propagation of "jets" into a low-density background material ("DDP experiment"), again using x-ray backlighting after lengthy (15- to 35-ns) time delays. The cell size of the low-density material (a copper foam) was varied, and the results compared to simulations. Figure 108.93 shows a schematic of the experiment and an example of the data. As the jet of material moves upward, vortices form to the left and right ("roll up"), in agreement with hydrodynamic simulations.

Finally, another collaboration (CEA, NRL, and LLNL) used OMEGA shots for x-ray source and effects experiments. Various targets were investigated for their ability to produce copious x rays in the region around 10 keV, as shown in Fig. 108.94.

FY06 LANL OMEGA Experimental Programs

Los Alamos National Laboratory (LANL) successfully fielded a range of experiments on OMEGA during FY06 studying the physics relevant to inertial confinement fusion (ICF) and high-energy-density (HED) science in support of the national
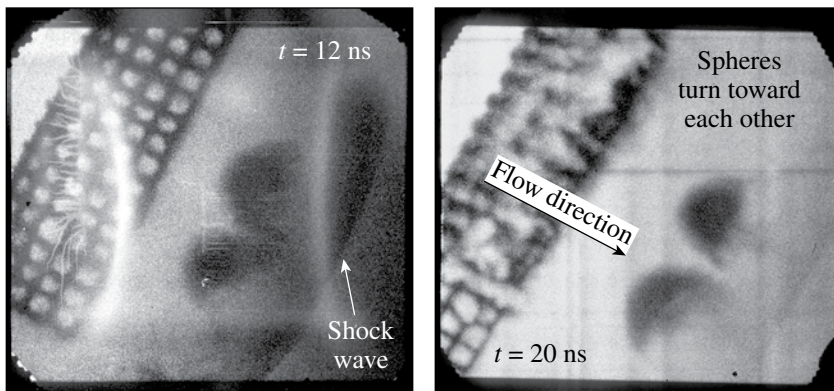
U609JR

Figure 108.92
X-ray-backlit images of shock (visible on right of the right-hand image, moving away from reference grid) and spheres imbedded in the low-density medium. Interacting clouds turn toward each other and eject material downstream after shock passage.
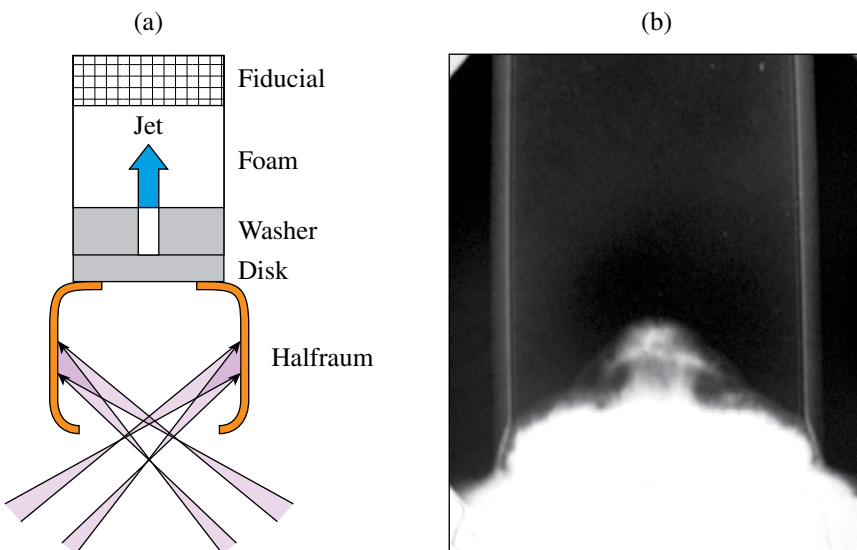
U610JRC

Figure 108.93
(a) Layout of DPP experiment (x-ray backlighting not shown, perpendicular to page through the foam). (b) Data at 15 ns. Note the classic "roll up" of the upward-moving jet.

DMX spectra indicate 80 to 170 J/sphere at 10 keV
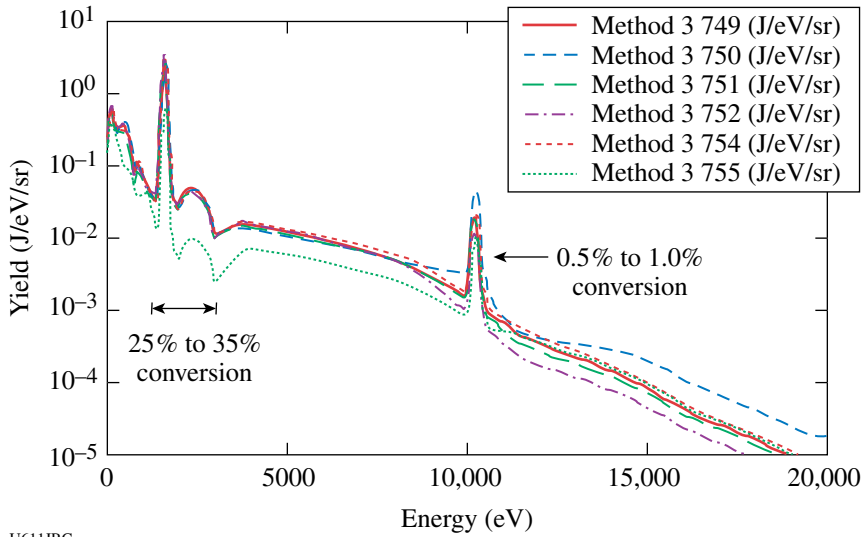and up to 6 kJ/sphere in the 1- to 3-keV band.

Figure 108.94
Laser and target conditions that optimize the 10-keV x-ray output have been identified.

U611JRC

ignition effort. Many of these experiments were focused on developing underlying physics, diagnostics, and platforms for future experiments on the National Ignition Facility (NIF). LANL conducted a total of 125 target shots on OMEGA. Collaborations with LLNL, LLE, MIT, and AWE remain an important component of LANL's program on OMEGA. With the consolidation of ignition research in the United States into the National Ignition Campaign (NIC), healthy partnerships are required to achieve success in the national scientific objectives.

Off-Hugoniot Heated Hydrodynamics: The off-Hugoniot (OH) campaign continued in FY06 with three days of experiments. High-quality data were obtained on 37 of 39 system shots. These experiments studied material dynamics under heated and shocked conditions. In ignition capsules, defects,

arising from the manufacturing process, undergo significant evolution due to heating from Au M-band radiation prior to passage of the main shock. It has not been demonstrated that our hydrocodes accurately capture the physics of this interaction. The OH platform provides the means to study the complex interaction between shocks and heated material.

The OH platform utilizes a beryllium (Be) housing that is coated with a thin layer of tin (Sn). Inside the housing are layers of foam and epoxy. Thirty-three beams strike the tin and produce L-shell radiation that permeates throughout the package, heating the epoxy and foam (Fig. 108.95). A short time later, seven beams launch a strong shock into the foam. As the heated epoxy expands in the foam, the shock interaction with this system is radiographed onto Agfa-D7 film.
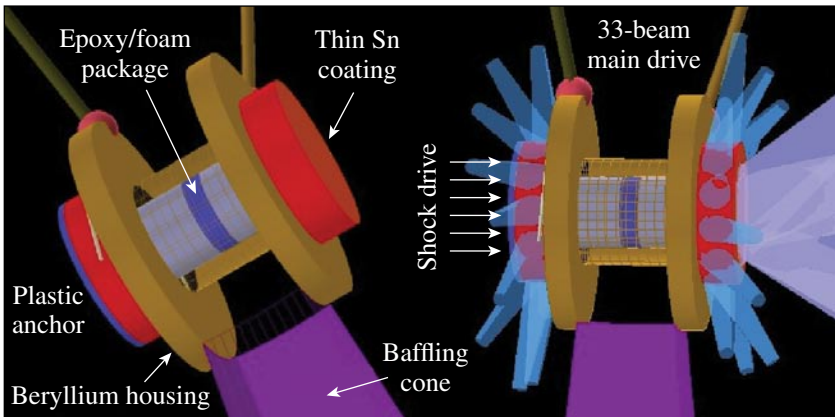
Figure 108.95
The target configuration for the off-Hugoniot experiment. A beryllium housing filled with layers of epoxy and foam is heated by exciting Sn L-shell radiation. The evolution of the epoxy expanding into the foam is imaged via radiography.

U612JRC

An example of the improved data quality is shown in Fig. 108.95. Data from heat-only experiments [Fig. 108.96(a)] clearly show the epoxy expansion and shock in the foam. Moreover, the use of the calibrated D7 film allows complete resolution of the evolving density profiles. When a defect is heated and a strong shock is introduced [Fig. 108.96(b)], the residual density perturbations from the healing defect distort the shock front as it propagates through the epoxy. The resulting density profiles and spatial deformation of the shock front provide tight constraints for our ignition design hydrocodes like *RAGE* and *PETRA*.

Inhomogeneous Radiation Flow: Inhomogeneously mixed materials can occur in a variety of environments. Two examples are ICF capsules, where shell material mixes with the fuel and turbulent flows, and astrophysical systems, such as molecular clouds and star-forming regions, where density clumps can form. Models for the transport of radiation in inhomogenously mixed

materials exist, each differing in the statistical treatment of the material mixtures. However, there is little experimental data to test these models. The inhomogeneous radiation flow experiment aims to provide data that can be used to test different models.

Figure 108.97 shows an overview of the experiment. A laser-driven hohlraum is heated to roughly 205 eV, which generates a temperature front. The temperature front propagates through gold-loaded foam, heating it. The soft-emission (~300 eV) of the heated foam is measured to determine the position of the radiation front. Two different gold-doped foams were examined: one loading with gold particles of diameters between 0.3 and 1.0 μm and another with very fine gold particles, diameters less than 0.1 μm.

Figure 108.98 displays preliminary measurements of the temperature-front position (circles) and the simulated trajectory

(a)   (b)
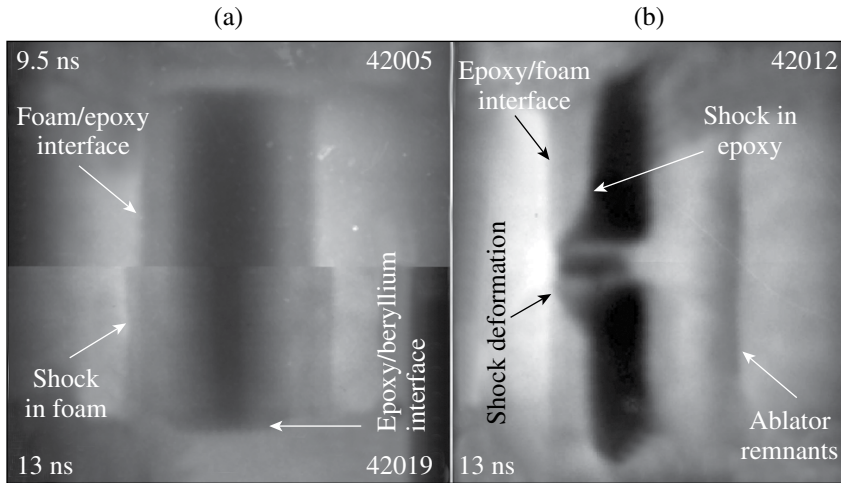
U613JR

Figure 108.96
(a) Radiographs of a heated-only, epoxy disk at 9.5 and 13.0 ns after the onset of heating. The deformation in the beryllium/epoxy interface and the shock formed by the epoxy expansion are both clearly visible. (b) Data from a heated and shocked 37.5-μm rectangular gap.
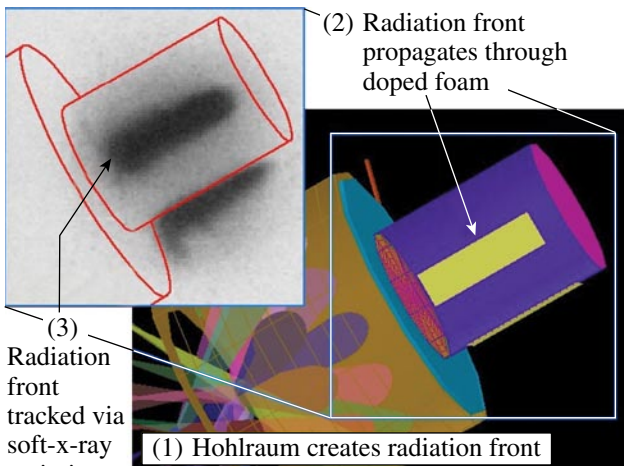
U614JRC

Figure 108.97
Sixteen beams heat a gold hohlraum that produces a radiation front that propagates through the foam. Diagnostic slits allow measurement of the front's progression.

of the temperature front (solid line). The simulation appears to be in good agreement with the data.

Beryllium Fill-Tube Defect Studies: Be shells are impermeable to gaseous and liquid DT. To fill an ICF capsule with a Be shell, a fill tube is used. The fill tube is attached to the shell through a counter-bored fill hole. Fill tubes and fill-tube holes for Be ICF capsules inject shell material into the fuel perturbing the implosion. Mixing between the shell material and the fuel cools the fuel and degrades the efficiency of the ICF capsule.

As part of the LANL/LLNL NIC effort, experiments designed to quantify the amount of Be mass ejected by the jet formed by the fill-tube hole were conducted. These experiments were performed in planar geometry due to complications of fabricating and diagnosing in spherical geometry. This experiment focused on large-aspect-ratio (depth/diameter), from 2 to 20,
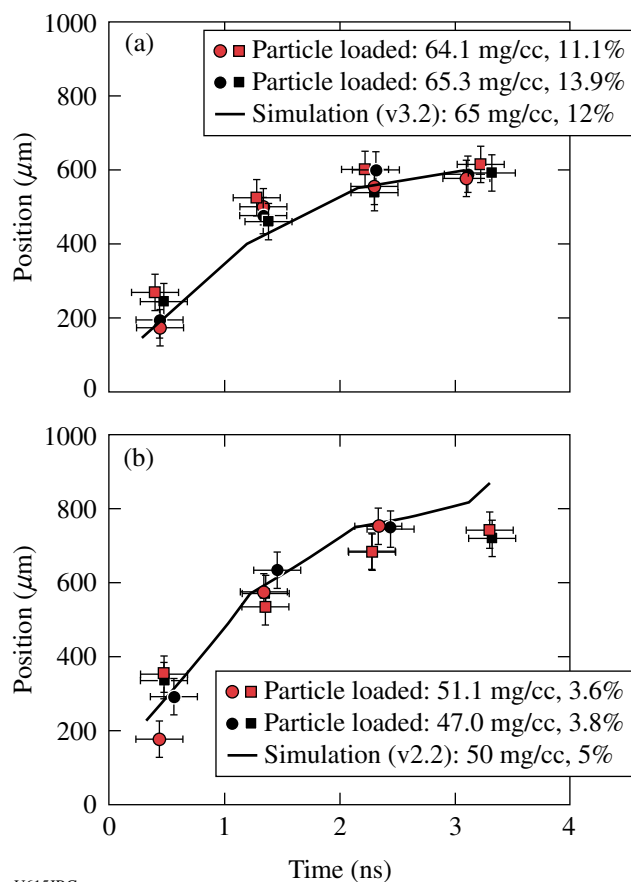

Figure 108.98
Simulations using NYM are in excellent agreement with the two cases examined: (top) 65-mg/cc foam with approximately 12% gold by weight and (bottom) 50-mg/cc foam with 5% gold by weight. [NYM simulations courtesy of M. Taylor (AWE).]

holes. The experimental configuration is shown in Fig. 108.99. A hohlraum is heated to 170- to 180-eV temperature. The temperature drive ablates and shocks the 100-μm-thick Be (3% Cu–doped) ablator. The shock ejects some material down the fill-tube hole and also propagates into the Be (3% Cu–doped) washer. The shock in the washer pushes material into the hole that jets into the foam.
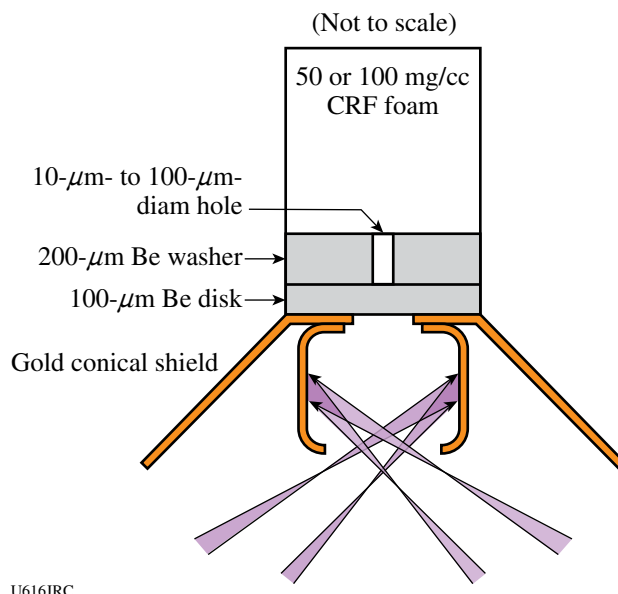

Figure 108.99
A heated gold hohlraum drives a shock into the beryllium disk, creating a jet as the Be is forced out the small hole at the bottom. The Be jet and disk are imaged from two orthogonal directions.

The mass of material jetted into the foam is measured with point-projection radiography at either 4.3 keV or 2.8 keV. Data have been obtained for jets formed by 100-, 50-, 40-, and 30-μm-diam holes. Figure 108.100 shows preliminary data of the jet formed by a 50-μm-diam fill-tube hole. The data were recorded with 4.3-keV x rays, 15 ns after the laser drive. The jet is roughly 170 μm across at the head and approximately 170 μm in length.

High-Z Shell Implosions: Two days of experiments studied the progression from non-LTE to LTE as the dopant gas concentration in a deuterium-filled capsule is increased. The presence of the high-Z dopants increases the radiation losses from the plasma, allowing the plasma to compress to a smaller volume. The physics of ignition and burn in high-Z capsules—specifically the effect of high-Z dopants on energy balance, equilibration, yield, and transport in implosions—is examined with measurements of yield, ρR, T_e, T_i, T_r, and implosion size.
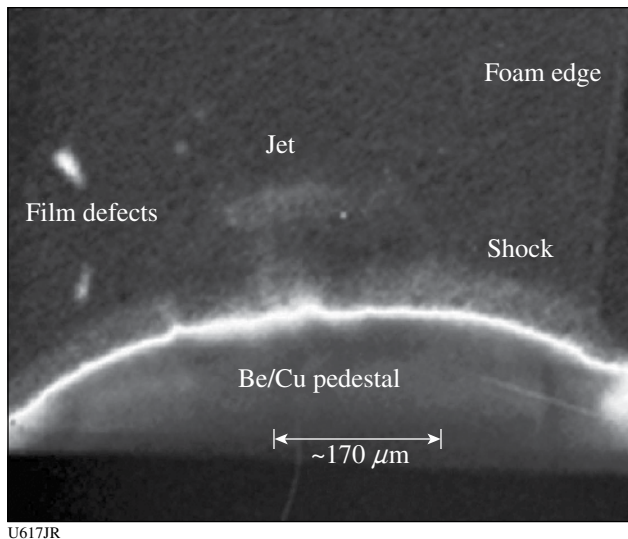
U617JR

Figure 108.100
The jet caused by a 50-μm-diam hole taken 15 ns after onset of the laser drive. Visible are the jet and the shock wave that has passed through the Be. The radiograph was obtained with 4.3-keV x rays.

These experiments used a 5-μm-thick SiO$_2$ spherical shell of 430-μm radius, filled with 7 atm of deuterium and 3 atm of ^{3}He. The ^{3}He allows measurement of the proton spectrum from the D^{3}He reaction and thus determines the target's ion temperature and ρR. Kr dopants were used as spectroscopic tracers to measure the electron temperature in the plasma from the helium lines. Variation of electron density is achieved by adjusting the Xe gas concentration. The experiments produced a wealth of data that is being used to determine how equilibrium is reached and to validate code calculations (Fig. 108.101).

High-Z Dopant Impact in Stimulated Raman Scattering (SRS): Experiments at the Helen laser observed a clear decrease in stimulated Raman backscattered (SRS) light when a small percentage, ~1%–2%, of a high-Z dopant such as Ar or Xe was added to a CH-filled gas-bag target. This experimental observation prompted interest in the phenomenon, especially as a mitigation strategy for reducing SRS in NIF hohlraums. However, the exact physical mechanism of the high-Z dopant effects was unknown, especially the fact that only small amounts of high-Z dopant are required. Theoretical investigation of the effects of high-Z dopants on SRS at LANL found that the addition of high-Z dopants leads to beam spray of the laser via thermally enhanced forward stimulated Brillouin scattering (FSBS). This beam spray causes a reduction is SRS due to a reduction in the spatial coherence of the laser. Thermal effects due to inverse-Bremsstrahlung absorption of the laser have a Z^2 dependence, meaning that a small amount of high-Z

material, compared to the background plasma Z, can have a large effect on the thermal response.
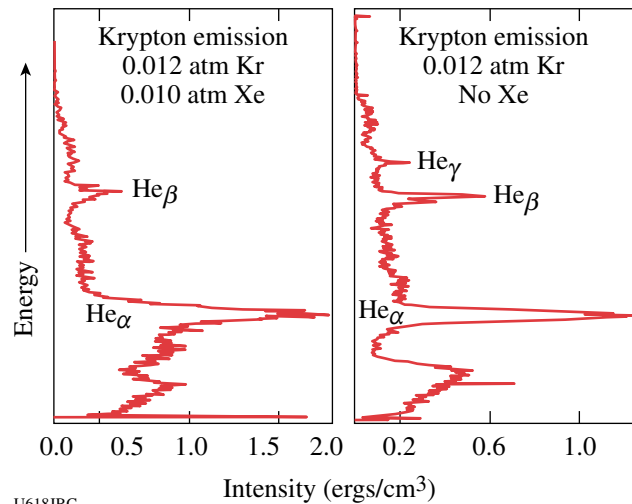

U618JRC

Figure 108.101
13- to 15-keV Krypton spectra of implosions doped (left) and undoped (right) with Xe. The enhanced cooling from Xe emission is observed by the reduction in He$_\gamma$ and He$_\beta$ emission of the Krypton spectra.

Through a strong collaboration by LANL, LLNL, and AWE, experiments were conducted at LLE using C$_5$H$_{12}$ gas-filled hohlraum targets to validate theory. SRS was measured for various amounts of Xe dopant added to the hohlraum gas fill. As the percentage of Xe dopant exceeded ~5%, SRS from the uniform interior hohlraum plasma region decreased. Figure 108.102 shows that the SRS reflectivity at wavelengths of ~550 nm, corresponding to an electron density of $n/n_c \sim 0.11$, where n_c is the critical density for 351-nm light, is reduced with the addition of 8.7% Xe compared to that of 3.6% Xe early in the interaction-beam laser pulse. This is an indication that high-Z dopants may affect SRS. However, measurements of the beam spray for the transmitted beam did not change significantly between the two cases. Thus, it is inconclusive whether the effect is due to beam spray or another mechanism such as reabsorption of SRS light via inverse Bremsstrahlung. Interestingly, large amounts of SRS come from the plasma expanding from the hohlraum based on hydrodynamic simulations and the wavelength of SRS at ~520 nm corresponding to an electron density $n/n_c \sim 0.06$.

In FY07 experiments, the laser intensity will be lowered to values closer to the critical onset intensity for SRS. The theory predicts a stronger effect of high-Z dopants at that intensity. In addition, the SRS reflectivity from the plasma expanding from the hohlraum should be decreased based on past experiments at the NOVA laser.
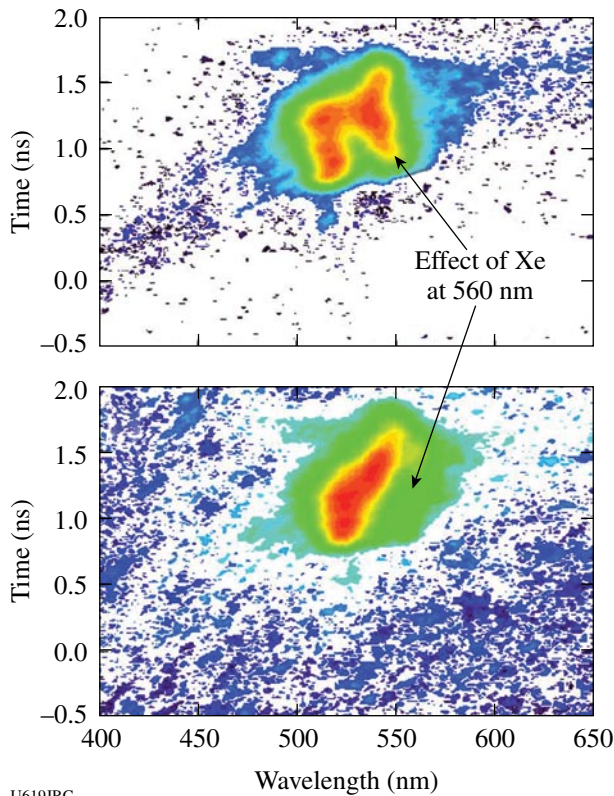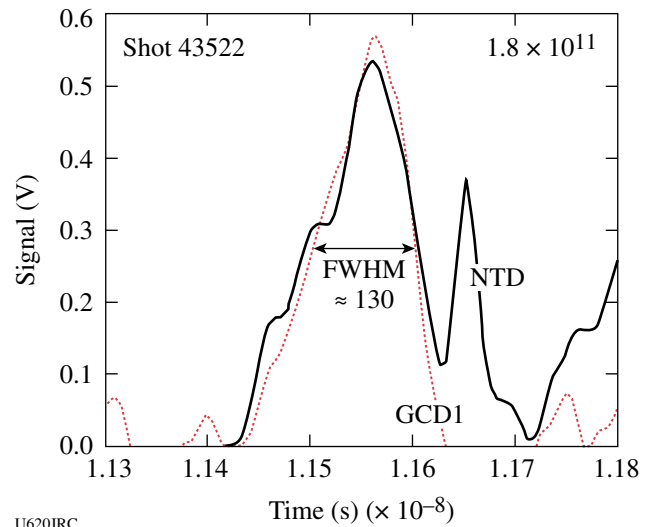
Figure 108.102
SRS spectra with (a) 3.6% and (b) 8.7% Xe dopant added to C_5H_{12} gas-filled hohlraums show a reduction in reflectivity at the interior electron density of $n/n_c \sim 0.11$ (~550 nm). However, most of the SRS reflectivity comes from the plasma expanding from the hohlraum at a lower electron density, $n/n_c \sim 0.06$ (~520 nm).
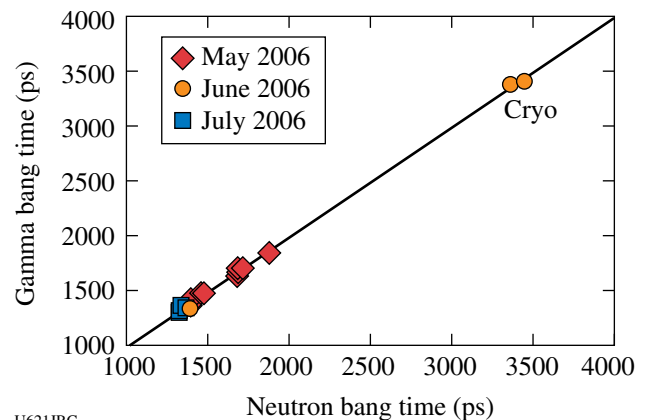

Figure 108.103
Gamma (GCD) and neutron reaction history (NTD) showing the consistency between burn history and peak neutron bang time.

Figure 108.104
Peak-neutron-bang-time measurements of GCD and NTD are consistent over a wide time window.

Gas Cherenkov Detector Development: The Gas Cherenkov Detector (GCD) is a collaborative effort between LANL, AWE, Photek, Inc., and NSTec to develop a fast "bang-time" diagnostic for NIF. The project benefited greatly from the multi-institutional diagnostic development efforts in FY06. Implementation of an ultrafast microchannel plate enhanced time response by a factor of 2.5 to better than 100 ps. This increased bandwidth enabled quality reaction histories of fusion burn using gammas (Fig. 108.103) to be obtained with speeds comparable to or exceeding that of the neutron temporal diagnostic (NTD). Moreover, bang-time measurements, i.e., the time of peak fusion reactivity, were achieved with a precision of 25 ps, when cross calibrated to NTD. This development should allow the gamma bang time/reaction history detector being planned for NIF to easily exceed the NIF system design requirement of 50 ps. The bang-time measurements, shown in Fig. 108.104, were obtained over a three-month period starting in May and ending with the 50/50 DT Cryo shots in July.

FY06 Sandia National Laboratories OMEGA Experimental Programs
SNL carried out 30 shots on OMEGA in FY06 including the following experiments:

Beryllium Ablation Rate Measurements in Planar Geometry: For a successful NIF ignition experiment, the ablator mass remaining at the end of the capsule implosion must be in the range of 3%–5% of the original ablator mass. If too much of the ablator burns off, the DT fuel will be preheated and the required fuel ρR cannot be achieved with the absorbed energy of the baseline ignition capsule. If too little of the ablator mass

burns off, the peak implosion velocity will be reduced and the hot-spot energy density will not be adequate for ignition. Thus, it is imperative that the mass ablation rate be known to high precision for the entire range of hohlraum temperatures encountered in the NIF ignition pulse shape. The experimental technique for ablation rate measurements in planar geometry is illustrated in Fig. 108.105 (details in Ref. 9). Basically, ablator samples are placed over an opening on the end of a halfraum. Laser beams enter through the LEH and provide the input power required to maintain the radiation field. The Dante array of K- and L-edge filtered photocathodes views the hohlraum wall through the LEH, and a time- and spectrally resolved measurement of the hohlraum radiation field is obtained from this data. An x-ray framing camera views the interior surface of the ablator sample, and the relative x-ray re-emission of the ablator versus the Au wall is determined. The streaked x-ray imager (SXI) diagnostic views the exterior surface of the abla-tor sample. The SXI employs an imaging slit, a transmission grating, an offset slit, and a streak camera to provide a highly time-resolved streaked image of the x-ray burnthrough flux on the exterior-facing side of the sample (as shown in Fig. 108.105). The combined information from these three measurements over a series of experiments is used to determine the mass ablation rate (mg/cm^2/ns) as a function of hohlraum radiation temperature. In FY06, reduced-scale halfraums and increased SXI magnification were used to extend the ablation rate data for Be and Cu-doped Be into the 200- to 270-eV temperature range. As shown in Fig. 108.106, the measurements have been directly compared to the equivalent mass ablation rate in the baseline NIF ignition capsule calculations.[10–12]
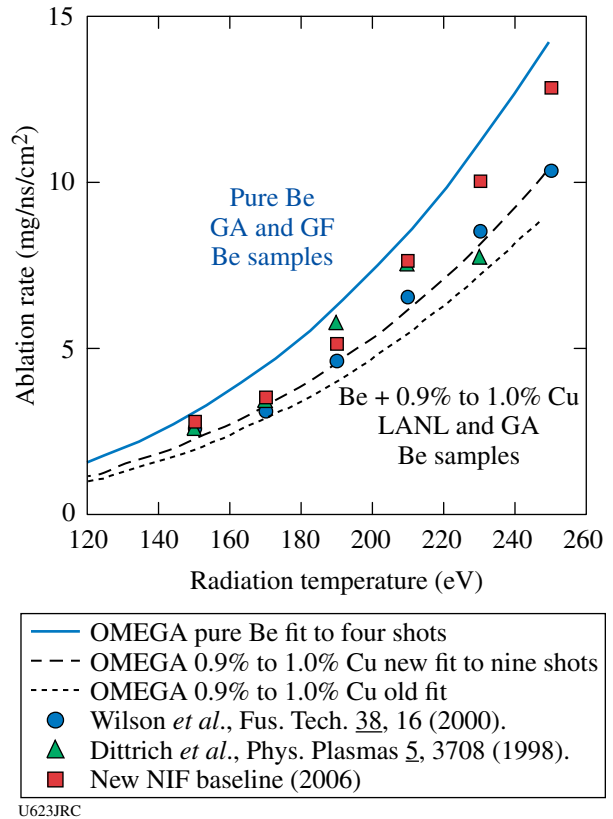

Figure 108.106
Ablation rate plotted as a function of radiation temperature from the OMEGA experiments (solid and dashed lines) and comparison to the baseline NIF capsule calculation. The range in the measured ablation rate seems to depend on view factor and spectrum as well as sample type and dopant concentration. Complete understanding of this data is work in progress.
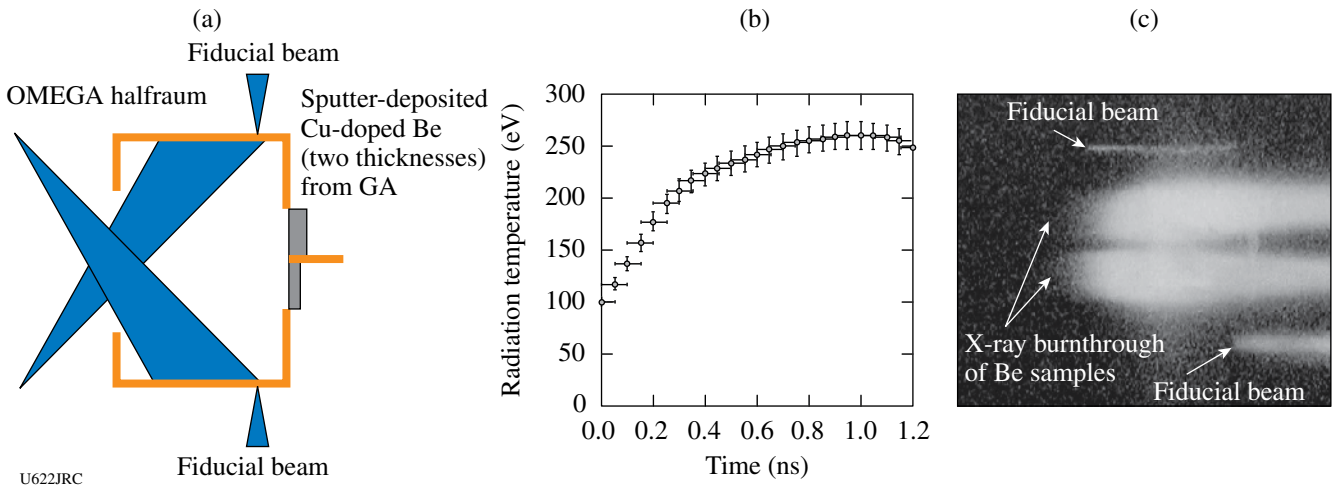

Figure 108.105
(a) Schematic of an ablation-rate measurement experiment. (b) DANTE-derived radiation temperature as a function of time. (c) Sample SXI streaked data showing burnthrough of Be samples.

Beryllium X-Ray Burnthrough and Ablation-Rate Measurements in Convergent Geometry: Since the ignition capsule's radius-time trajectory will vary with the shock-timing adjustments, it will be necessary to experimentally determine the burnthrough/no-burnthrough threshold of an imploding ablator shell and to iterate this burnthrough threshold measurement with the NIF shock-timing experiments. In FY06, SNL performed a series of experiments to develop a convergent ablation rate and burnthrough measurement technique. As illustrated in Fig. 108.107, the convergent burnthrough experiments are a logical extension of the planar ablation rate experiments. In the convergent experiments, a beryllium hemi-shell was mounted in a halfraum. The halfraum was larger than the sizes used in planar experiments, and specific beam-pointing adjustments were required to obtain acceptable capsule illumination symmetry (<±5% in flux). An important diagnostic concern was that pinhole SXI imaging (rather than

slit imaging) was required for the convergent measurement, and a new technique was developed to verify the pointing and alignment accuracy to within ±50 μm. The SXI pinhole imaging setup is illustrated in Fig. 108.108, and the alignment verification technique is illustrated in Fig. 108.109. Key features of the burnthrough and no-burnthrough SXI streaks were verified in the FY06 experiments, and a preliminary unfold of convergent ablation rate was obtained from one of the experiments. Figure 108.110 shows an example x-ray streak image illustrating the spatial and time fiducials and an overlay of computationally simulated ablation-front and implosion features.

VISAR Measurement of Hohlraum Radiation Temperature: In FY05, a new technique for time-resolved measurement of hohlraum radiation temperature was successfully tested in a series of OMEGA experiments.[13] In FY05, we performed a series of experiments to extend the measurement techniques of Ref. 13 to situations in which shaped laser pulses have been used to produce sudden increases in the hohlraum radiation field, resulting in multiple shock fronts that converge within the quartz sample. As can be seen in Fig. 108.111, the interferometer technique appears to work well for this situation. Based on FY06 results, it is conceivable that a new series of Dante-interferometer calibration shots can be used to produce empirical relationships for the situation of multiply shocked quartz.

Development of a NIF Shock-Timing Diagnostic: The x-ray flux absorbed by an indirect-drive ICF capsule consists of a combination of blackbody x rays emitted from the high-Z hohlraum walls and higher-energy (>1 keV) x rays that originate in and near the hot, low-density plasma in which the laser light is absorbed. The high-energy photons can penetrate beyond the capsule. In previous LLE/SNL/LLNL collaborative experiments,[14] we found that, as hohlraum temperatures were increased beyond 135 eV, the ASBO window was preheated and became opaque. In the first half of FY06, the approach was to position the window completely out of the
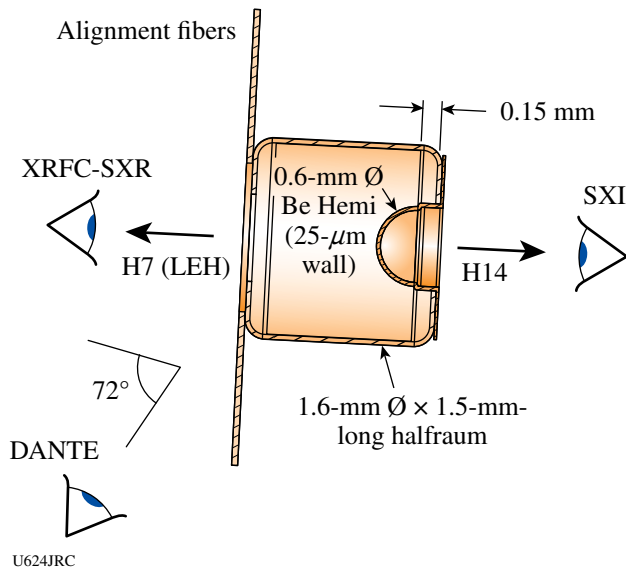

Figure 108.107
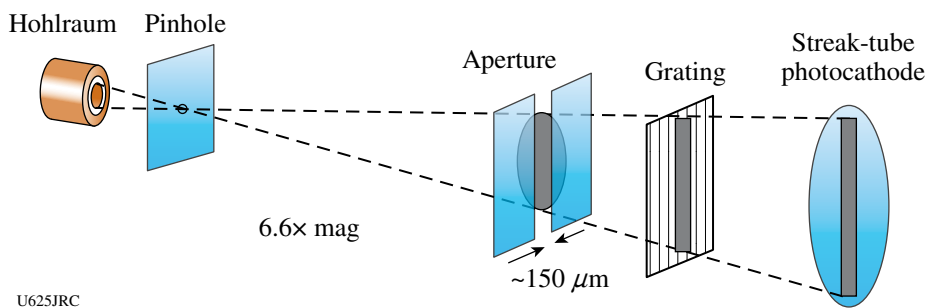Illustration of a convergent burnthrough experiment.

Figure 108.108
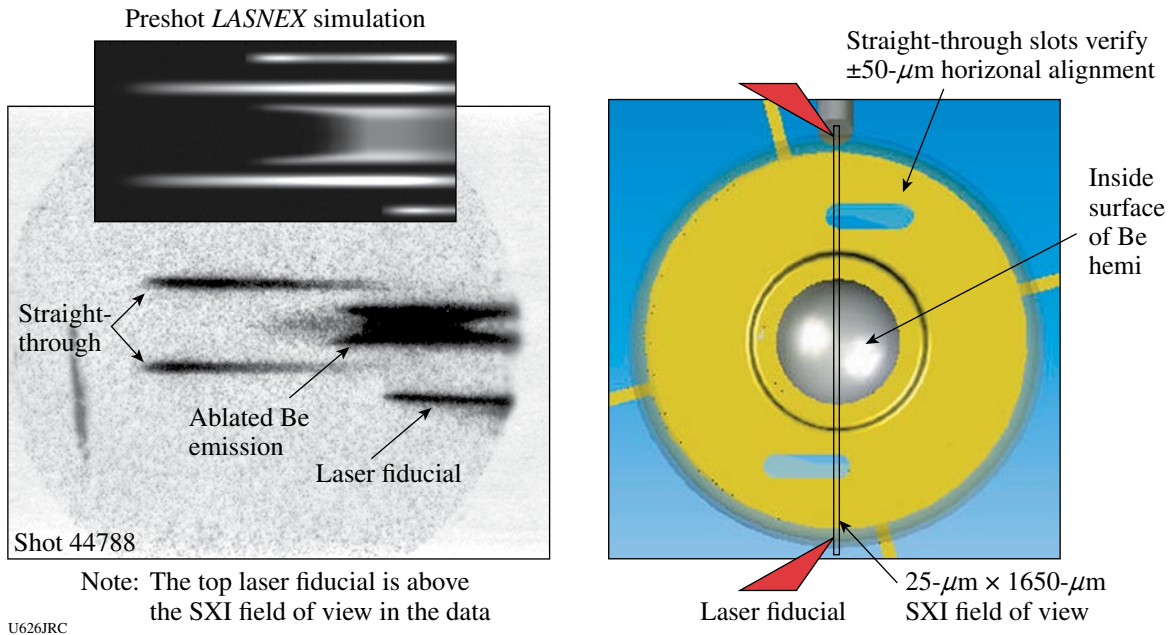Schematic showing SXI pinhole imaging setup.

Preshot *LASNEX* simulation

Straight-through slots verify ±50-μm horizonal alignment

Straight-through

Ablated Be emission

Laser fiducial

Shot 44788

Note: The top laser fiducial is above the SXI field of view in the data

U626JRC

Inside surface of Be hemi

Laser fiducial

25-μm × 1650-μm SXI field of view

Figure 108.109
Illustration of the alignment verification technique.

OMEGA shot 44788 SXI image

Simulated SXI image using 44788 Dante Tr

1.0 mm

Overlay of simulated ablation front and stagnation

$t = 0$ ns

$t = 2.5$ ns

U627JRC
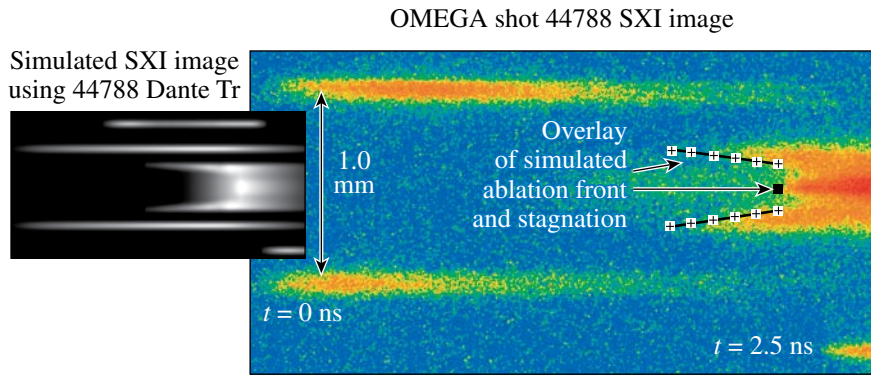
Figure 108.110
Sample SCI data (right) and simulation from a convergent breakthrough experiment (left).

ASBO

SOP

Tr increasing   Second shock   First shock   Second shock

U628JRC

SOP lineout

First shock

Second shock
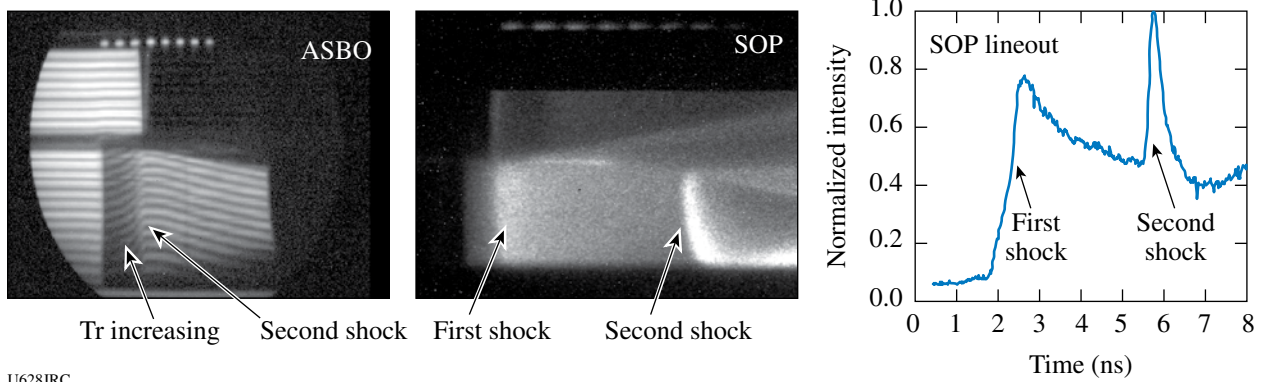
Normalized intensity

Time (ns)

Figure 108.111
Illustration of the VISAR technique to measure hohlraum radiation temperature.

line of sight of the laser spots in a halfraum geometry. This approach improved the situation and resulted in successful ASBO measurements for halfraum temperatures exceeding 140 eV (see Fig. 108.112). In late FY06, a series of experiments was started in which a NIF-like shock-timing geometry was tested. The first so-called "line-of-sight" hohlraum targets (Fig. 108.113) were designed and assembled at SNL. The targets worked well, but the experimental results indicated that further refinements in the design will be required for a successful shock-timing technique.
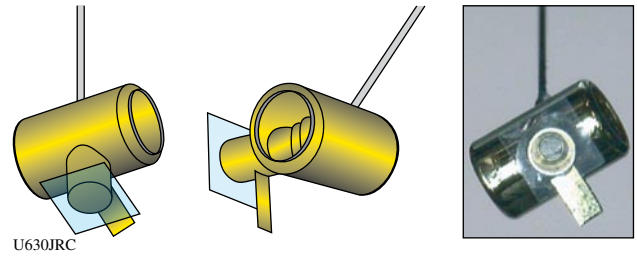

Figure 108.113
Schematic of hohlraum used to test a NIF-like shock-timing geometry.

FY06 CEA OMEGA Experimental Programs

In FY06, CEA carried out 49 target shots on OMEGA on several campaigns including studies of Rayleigh–Taylor instabilities in indirect-drive targets and the implementation of high-resolution x-ray imaging. Some of this work is outlined in this section.

Rayleigh–Taylor Instabilities in Indirect Drive: Mode-Coupling Experiments: Rayleigh–Taylor instabilities in indirect drive have been investigated by CEA on OMEGA since 2002 by using a rugby wall-shaped hohlraum.[15] Rugby hohlraums are, in fact, alternative designs for pre-ignition experiments with reduced energy on LMJ,[16] and the control of symmetry in a rugby hohlraum was also one of the goals of CEA FY06 symmetry experiments. A sketch of a rugby hohlraum is shown in Fig. 108.114 together with a diagram of the experimental configuration used for the RTI experiments. The cavity is heated with 40 beams (pulse shape PS26) in a three-cone (21°, 42°, and 59°) irradiation scheme. The 21° beams propagate across the hohlraum and are absorbed in the slanted part of the wall on the opposite side of the laser entrance hole. Dual-axis radiographies (side-on and face-on) are performed on each shot to measure the foil acceleration and the perturbation growth.

Previous experimental campaigns were devoted to the measurement of single-mode RT growth rate (wavelengths $\lambda = 50$ and $70\ \mu$m) and the study of the feedout mechanism[17] in the case where the modulations were placed on the cold face [rear side, Fig. 108.114(a)] of the radiatively driven plastic foils.

The FY06 campaign focused on mode coupling with germanium-doped foils (CHGe, 2.8% in atomic weight) modulated front side with a two-mode pattern ($\lambda = 35$ and $70\ \mu$m). Depending on the relative phase between the two modes (in phase or in opposite phase), one or the other wavelength is predicted to become predominant during the growth. As illustrated in Fig. 108.115, if we compare two face-on pictures taken at the same time after t_0 ($t = 2.7$ ns), one sees clearly on the lineouts that
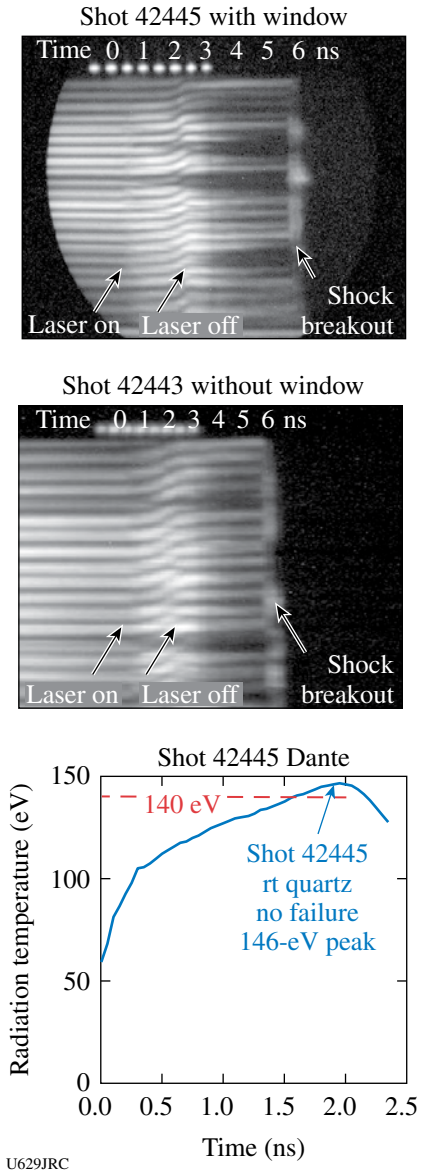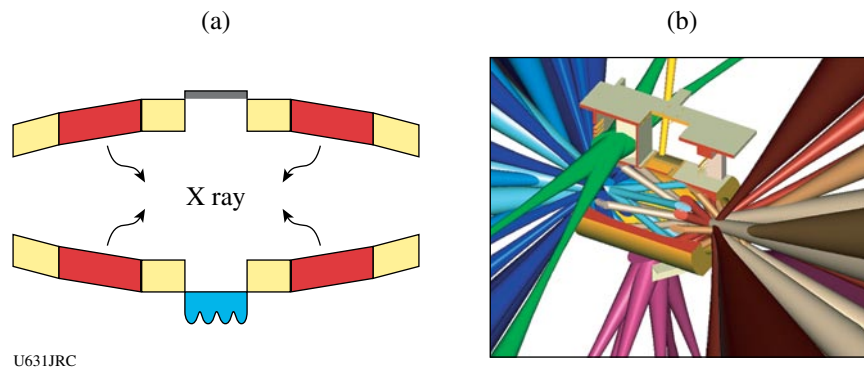

Figure 108.112
Illustration of successful ASBO measurement in radiation fills exceeding 140 eV.

U631JRC

Figure 108.114
(a) Sketch of a rugby hohlraum. (b) Diagram of the configuration for RTI experiments. The 21° beams propagate across the cavity and are absorbed in the slanted part of the wall on the opposite side of the laser entrance hole.
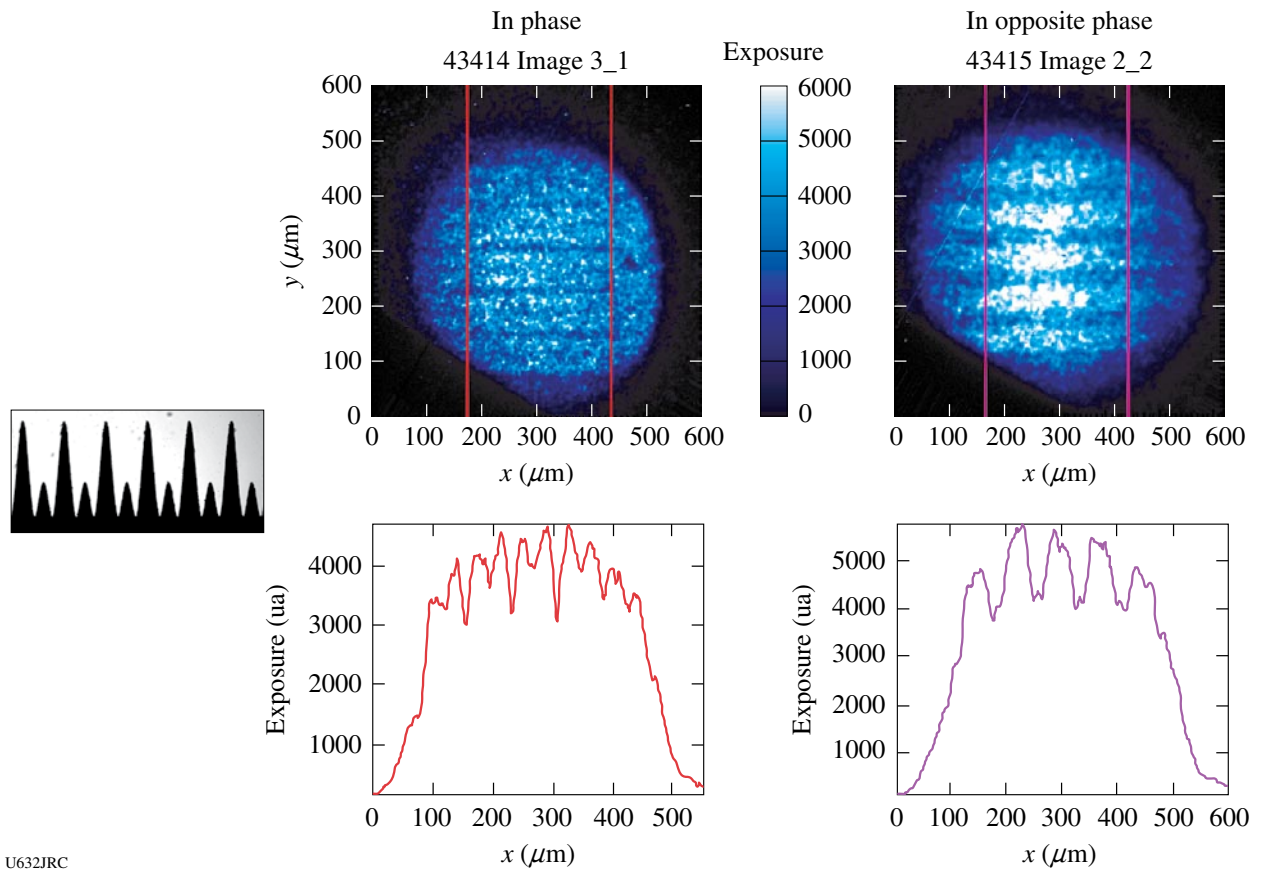
U632JRC

Figure 108.115
Lineouts across two face-on pictures taken at the same time ($t = 2.7$ ns) for the two-mode patterns ($\lambda = 35$ and 70 μm) under study. On the left, in phase pattern with the preponderant $\lambda = 35$-μm mode. On the right, the opposite phase pattern where $\lambda = 70$ μm predominates.

the $\lambda = 35$-μm mode overwhelms the $\lambda = 70$-μm mode for the in-phase case, and inversely for the opposite-phase pattern. As a consequence, the growth of the $\lambda = 35$-μm mode in the opposite-phase pattern is predicted to be delayed in time (due to a phase inversion) in comparison with a pure $\lambda = 35$-μm monomode. This trend is recovered in Fig. 108.116 on the plot showing the evolution of the optical depth versus time for both cases.

High-Resolution X-Ray Imaging (HRXI): For several years, Commissariat à l'Énergie Atomique in France (CEA/DIF Center[18]) has been developing HRXI, a high-resolution, time-resolved, x-ray imaging diagnostic. In FY06, HRXI was implemented and tested for the first time on OMEGA. HRXI combines two state-of-the-art technologies: a high-resolution x-ray microscope and a high-speed x-ray streak camera. The resulting instrument achieves a spatial and temporal resolution of ~5 μm and ~30 ps, respectively. The experimental configuration is shown in Fig. 108.117. The Wolter x-ray microscope for HRXI, used previously on Phebus experiments,[19] consists of two similar off-axis toroidal mirrors. The microscope had a focal length of 218 mm and a magnification ratio of 16. The mirrors were coated with a 30-nm Ni coating (energy cutoff ~6 keV). The microscope features an integrated visible-light

alignment system enabling the simultaneous projection of two crosses in the object plane and the image plane.
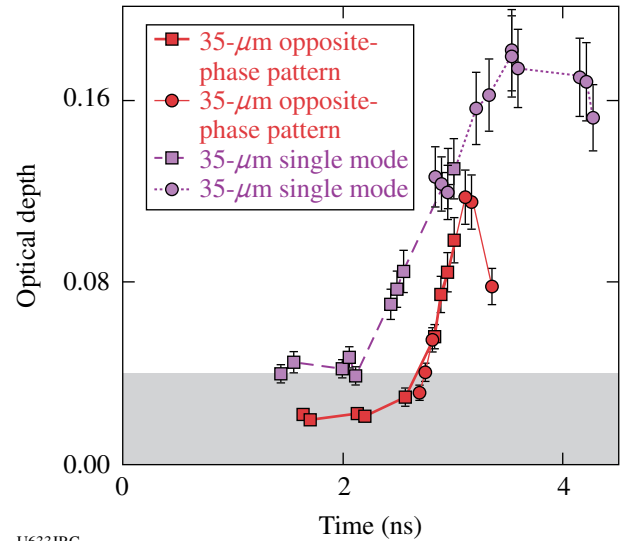
U633JRC

Figure 108.116
Growth (in optical depth) of the $\lambda = 35$-μm mode for the opposite phase pattern (solid symbols) and for a pure monomode perturbation (open symbols).
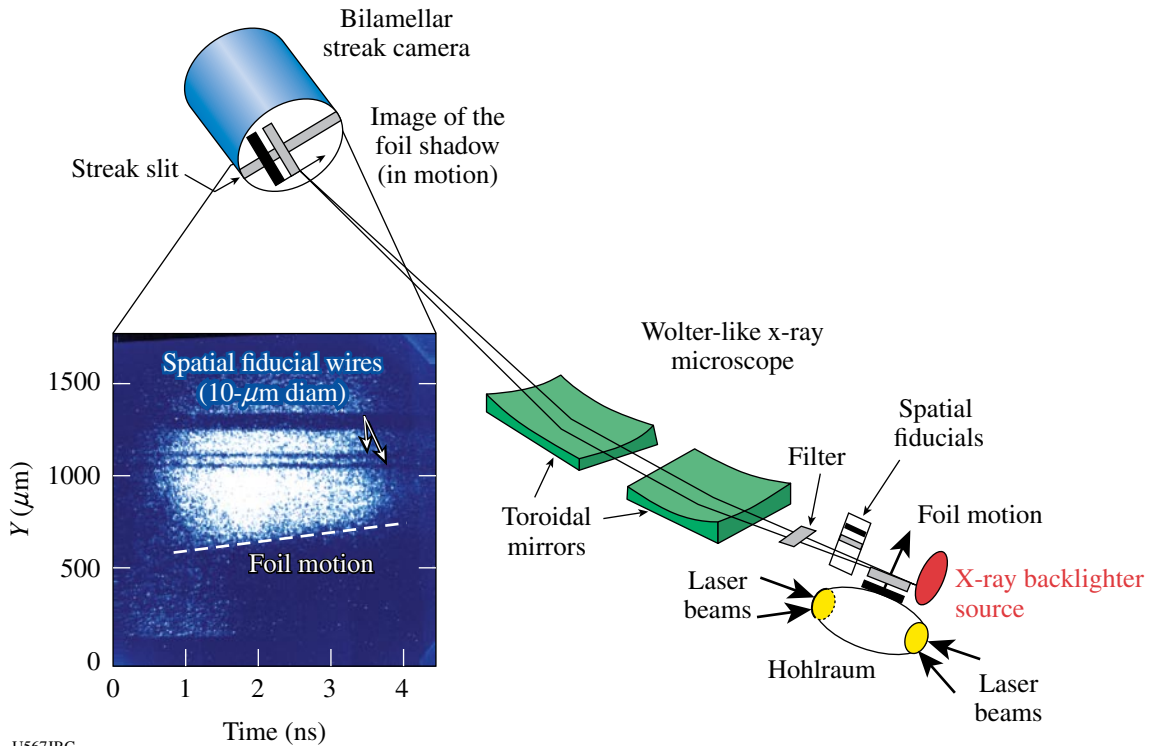
U567JRC

Figure 108.117
HRXI setup with a streaked image recorded during OMEGA shot 43418.

The streak camera includes a bilamellar-type streak tube,[20] which achieves both high temporal (30 ps) and spatial resolution (15 lp/mm). To match to the emitted x-ray backlighter spectrum used for these experiments (Ti foil emission near 4.8 keV), a transmission-mode photocathode was used with a thin CsI coating (10 nm) that was deposited on a self-sustaining CH foil of 800-nm thickness. The streak tube's P20 phosphor screen was read out with a cooled 1340×1300-pixel CCD with a 20-μm pixel size.

HRXI was sucessfully tested for the first time on OMEGA during a joint CEA/DOE-LLE campaign on 27 April 2006. For these tests, HRXI recorded the acceleration of a thin, Ge-doped CH (45-μm) foil driven by radiation from a rugby-wall–shaped hohlraum heated by 40 OMEGA beams with a 2-ns-time-duration, PS26 pulse shape. The foil was accelerated to a velocity of 60 μm/ns. The inset in Fig. 108.117 shows a streak record of the motion of this thin foil in time using a 3-ns x-ray backlighter source. Three test objects were placed close to the foil to assess the spatial resolution of the diagnostic. Two 10-μm-diam wires are clearly visible in the middle and along the streak image, leading to an actual estimated spatial resolution on the streaked image of less than 5 μm.

REFERENCES

1. R. F. Smith *et al.*, "Stiff Response in Aluminum Under Ultrafast Shockless Compression up to 110 Gpa," submitted to Physical Review Letters.

2. S. D. Rothman *et al.*, J. Phys. D **38**, 733 (2005).

3. R. F. Smith *et al.*, "Graded-Density Reservoirs for Accessing High Pressure Low Temperature Material States," to be published in Astrophysics and Space Science.

4. R. Jeanloz, Geophys. Res. Lett. **8**, 1219 (1981).

5. M. H. Rice, R. G. McQueen, and J. M. Walsh, Solid State Phys. **6**, 1 (1958).

6. C. K. Li, F. H. Séguin, J. A. Frenje, J. R. Rygg, R. D. Petrasso, R. P. J. Town, P. A. Amendt, S. P. Hatchett, O. L. Landen, A. J. Mackinnon, P. K. Patel, V. A. Smalyuk, T. C. Sangster, and J. P. Knauer, Phys. Rev. Lett. **97**, 135003 (2006).

7. C. K. Li, F. H. Séguin, J. A. Frenje, J. R. Rygg, R. D. Petrasso, R. P. J. Town, P. A. Amendt, S. P. Hatchett, O. L. Landen, A. J. Mackinnon, P. K. Patel, V. Smalyuk, J. P. Knauer, T. C. Sangster, and C. Stoeckl, Rev. Sci. Instrum. **77**, 10E725 (2006).

8. D. H. Froula *et al.*, Phys. Plasmas **13**, 052704 (2006).

9. R. E. Olson, R. J. Leeper, A. Nobile, J. A. Oertel, G. A. Chandler, K. Cochrane, S. C. Dropinski, S. Evans, S. W. Haan, J. L. Kaae, J. P. Knauer, K. Lash, L. P. Mix, A. Nikroo, G. A. Rochau, G. Rivera, C. Russell, D. Schroen, R. J. Sebring, D. L. Tanner, R. E. Turner, and R. J. Wallace, Phys. Plasmas **11**, 2778 (2003).

10. D. C. Wilson *et al.*, Fusion Technol. **38**, 16 (2000).

11. T. R. Dittrich *et al.*, Phys. Plasmas **5**, 3708 (1998).

12. S. W. Haan *et al.*, Fusion Sci. Technol. **49**, 553 (2006).

13. R. E. Olson *et al.*, Rev. Sci. Instrum. **77**, 10E523 (2006).

14. R. E. Olson, R. J. Leeper, G. A. Rochau, D. K. Bradley, P. M. Celliers, and T. R. Boehly, J. Phys. IV France **133**, 179 (2006).

15. A. Casner *et al.*, J. Phys. IV France **133**, 163 (2006).

16. J. Giorla *et al.*, Plasma Phys. Control. Fusion **48**, B75 (2006).

17. D. P. Smitherman *et al.*, Phys. Plasmas **6**, 932 (1999).

18. J. L. Bourgade *et al.*, CEA/DIF Center, Service SCEP, BP 12, Bruyères le Châtel, 91680, France.

19. Ph. Troussel *et al.*, Rev. Sci. Instrum. **76**, 063707 (2005).

20. A. Mens *et al.*, in *19th International Congress on High-Speed Photography and Photonics*, edited by B. Garfield and J. Rendell (SPIE, Bellingham, WA, 1990), Vol. 1358, pp. 315–328.

Publications and Conference Presentations

Publications

G. P. Grim, C. W. Barnes, P. A. Bradley, C. R. Christensen, A. Hauer, G. L. Morgan, J. A. Oertel, M. D. Wilke, D. C. Wilson, C. Barrera, S. W. Haan, B. A. Hammel, J. A. Koch, R. A. Lerche, M. J. Moran, V. L. Glebov, T. C. Sangster, J.-L. Bourgade, L. Disdier, I. Lantuejoul, and O. Landoas, "Neutron Imaging at the NIF," J. Phys. IV France **133**, 913 (2006).

M. Houry, E. Delagnes, D. Riz, B. Canaud, L. Disdier, F. Garaude, Y. Giomataris, V. Yu. Glebov, Ph. Legou, Ph. Rebourgeard, and C. Sangster, "DEMIN: A Neutron Spectrometer, Micromegas-Type, for Inertial Confinement Fusion Experiments," Nucl. Instrum. Methods Phys. Res. A **557**, 648 (2006).

I. V. Igumenshchev, "Three-Dimensional Simulations of Spherical Accretion Flows with Small-Scale Magnetic Fields," Astrophys. J. **649**, 361 (2006).

J. R. Marciante and J. D. Zuegel, "High-Gain, Polarization-Preserving, Yb-Doped Fiber Amplifier for Low-Duty-Cycle Pulse Amplification," Appl. Opt. **45**, 6798 (2006).

F. H. Séguin, J. L. DeCiantis, J. A. Frenje, C. K. Li, J. R. Rygg, C. D. Chen, R. D. Petrasso, J. A. Delettrez, S. P. Regan, V. A. Smalyuk, V. Yu. Glebov, J. P. Knauer, F. J. Marshall, D. D. Meyerhofer, S. Roberts, T. C. Sangster, C. Stoeckl, K. Mikaelian, H. S. Park, H. F. Robey, and R. E. Tipton, "Measured Dependence of Nuclear Burn Region Size on Implosion Parameters in Inertial Confinement Fusion Experiments," Phys. Plasmas **12**, 082704 (2006).

J. D. Zuegel, V. Bagnoud, J. Bromage, I. A. Begishev, and J. Puth, "High-Performance OPCPA Laser System," J. Phys. IV France **133**, 701 (2006).

Forthcoming Publications

R. Betti, K. Anderson, T. R. Boehly, T. J. B. Collins, R. S. Craxton, J. A. Delettrez, D. H. Edgell, R. Epstein, V. Yu. Glebov, V. N. Goncharov, D. R. Harding, R. L. Keck, J. H. Kelly, J. P. Knauer, J. P. Knauer, S. J. Loucks, J. A. Marozas, F. J. Marshall, A. V. Maximov, D. N. Maywar, R. L. McCrory, P. W. McKenty, D. D. Meyerhofer, J. Myatt, P. B. Radha, S. P. Regan, C. Ren, T. C. Sangster, W. Seka, S. Skupsky, A. A. Solodov, V. A. Smalyuk, J. M. Soures, C. Stoeckl, W. Theobald, B. Yaakobi, C. Zhou, J. D. Zuegel, J. A. Frenje, C. K. Li, R. D. Petrasso, and F. H. Séguin, "Progress in Hydrodynamics Theory and Experiments for Direct-Drive and Fast Ignition Inertial Confinement Fusion," to be published in Plasma Physics and Controlled Fusion.

R. Betti and J. Sanz, "Bubble Acceleration in the Ablative Rayleigh–Taylor Instability," to be published in Physical Review Letters.

R. Betti, A. A. Solodov, J. A. Delettrez, and C. Zhou, "Gain Curves for Fast-Ignition at Densities Around 300 g/cc," to be published in Physics of Plasmas.

J. Bromage, C. Dorrer, I. A. Begishev, N. G. Usechak, and J. D. Zuegel, "Highly Sensitive, Single-Shot Characterization for Pulse Widths from 0.4 ps to 85 ps Using Electro-Optic Shearing Interferometry," to be published in Optics Letters.

V. Yu. Glebov, D. D. Meyerhofer, T. C. Sangster, C. Stoeckl, S. Roberts, C. A. Barrera, J. R. Celeste, C. J. Cerjan, L. S. Dauffy, D. C. Eder, R. L. Griffith, S. W. Haan, B. A. Hammel, S. P. Hatchett, N. Izumi, J. R. Kimbrough, J. A. Koch, O. L. Landen, R. A. Lerche, B. J. MacGowan, M. J. Moran, E. W. Ng, T. W. Phillips, P. M. Song, R. Tommassini, B. K. Young, S. E. Caldwell, G. P. Grim, S. C. Evans, J. M. Mack, T. J. Sedillo, M. D. Wilke, D. C. Wilson, C. S. Young, D. Casey, J. A. Frenje, C. K. Li, R. D. Petrasso, F. H. Séguin, J. L. Bourgade, L. Disdier, M. Houry, I. Lantejoule, O. Landoas, G. A. Chandler, G. W. Cooper, R. J. Leeper, R. E. Olson, C. L. Ruiz, M. A. Sweeney, S. P. Padalino, C. Horsfield, and B. A. Davis, "Development of Nuclear Diagnostics for the National Ignition Facility," to be published in Review of Scientific Instruments (invited).

V. Yu. Glebov, C. Stoeckl, T. C. Sangster, C. Mileham, and R. A. Lerche, "High-Yield Bang Time Detector for the OMEGA Laser," to be published in Review of Scientific Instruments.

V. N. Goncharov, "Ablative Richtmyer–Meshkov Instability: Theory and Experimental Results," to be published in the Proceedings of Scottish Summer School.

V. N. Goncharov, "Direct-Drive Inertial Fusion: Basic Concepts and Ignition Target Designing," to be published in the Proceedings of Scottish Summer School.

M. Haurylau, S. P. Anderson, K. L. Marshall, and P. M. Fauchet, "Electrically Tunable Silicon 2-D Photonic Bandgap Structures," to be published in IEEE Journal of Quantum Electronics.

B. Hu, R. Betti, and J. Manickam, "Kinetic Stability of the Internal Link Mode in ITER," to be published in Physics of Plasmas.

S. D. Jacobs, "Manipulating Mechanics and Chemistry in Precision Optics Finishing," to be published in Science and Technology of Advanced Materials.

Z. Jiang and J. R. Marciante, "Mode-Area Scaling of Helical-Core, Dual-Clad Fiber Lasers and Amplifiers Using an Improved Bend-Loss Model," to be published in the Journal of the Optical Society of America B.

T. Z. Kosc, C. J. Coon, G. V. Babcock, K. L. Marshall, A. Trajkovska-Petkoska, and S. D. Jacobs, "Exploring Motion Reversal in Polymer Cholesteric-Liquid-Crystal Devices," to be published in the Proceedings of SPIE.

T. Z. Kosc, A. A. Kozlov, and A. W. Schmid, "Formation of Periodic Microstructures on Multilayer Dielectric Gratings Prior to Total Ablation," to be published in Optics Express.

B. E. Kruschwitz, J. H. Kelly, M. J. Shoup III, L. J. Waxer, E. C. Cost, E. T. Green, Z. M. Hoyt, J. Taniguchi, and T. W. Walker, "High-Contrast Plasma-Electrode Pockels Cell (PEPC)," to be published in Applied Optics.

N. N. Lepeshkin, S. G. Lukishova, R. W. Boyd, and K. L. Marshall, "Feedback-Free, Single-Beam Pattern Formation by Nanosecond Pulses in Dye-Doped Liquid Crystals," to be published in the Proceedings of SPIE.

S. G. Lukishova, A. W. Schmid, R. Knox, P. Freivald, L. Bissell, R.W. Boyd, C. R. Stroud, Jr., and K. L. Marshall, "Room Tem-perature Source of Single Photons of Definite Polarization," to be published in the Journal of Modern Optics.

J. A. Marozas, "Fourier-Transform-Based Continuous Phase-Plate Design Technique: A High-Pass Phase-Plate Design as an Application for OMEGA and the NIF," to be published in the Journal of the Optical Society of America A.

F. J. Marshall, J. P. Knauer, D. Anderson, and B. L. Schmitt, "Absolute Calibration of Kodak Biomax-MS Film to X Rays in the 1.5- to 8-keV Range," to be published in Review of Scientific Instruments.

K. L. Marshall, A. G. Noto, G. Painter, and N. Tabirian, "Computational Chemistry Methods for Predicting the Chiroptical Properties of Liquid Crystal Systems. II. Application to Chiral Azobenzenes," to be published in the Proceedings of SPIE.

P. W. McKenty, M. D. Wittman, and D. R. Harding, "Effect of Experimentally Observed Hydrogenic Fractionation in ICF Ignition-Target Performance," to be published in the Journal of Applied Physics.

A. V. Okishev and J. D. Zuegel, "Intracavity-Pumped Raman Laser Action in a Mid-IR, Continuous-Wave (cw) MgO: PPLN Optical Parametric Oscillator," to be published in Optics Express.

M. B. Schneider, D. E. Hinkel, O. L. Landen, R. Bahr, H. A. Baldis, C. Constantin, D. H. Froula, V. Yu. Glebov, R. F. Heeter, A. B. Langdon, M. J. May, J. McDonald, J. S. Ross, W. Seka, M. Singh, C. Stoeckl, L. J. Suter, K. Widmann, and B. K. Young, "Plasma Filling in Reduced-Scale Hohlraums Irradiated with Multiple Beam Cones," to be published in Physics of Plasmas.

S. N. Shafrir, J. C. Lambropoulos, and S. D. Jacobs, "A Magnetorheological Polishing-Based Approach for Studying Precision Microground Surfaces of Tungsten Carbides," to be published in Precision Engineering.

W. Słysz, M. Węgrzecki, J. Bar, P. Grabiec, M. Górska, V. Zwiller, C. Latta, P. Böhi, A. J. Pearlman, A. S. Cross, D. Pan, J. Kitaygorsky, I. Komissarov, A. Verevkin, I. Milostnaya, A. Korneev, O. Minayeva, G. Chulkova, K. Smirnov, B. Voronov, G. N. Gol'tsman, and R. Sobolewski, "Fiber-Coupled, Single-Photon Detector Based on NbN Superconducting Nanostructures for Quantum Communications," to be published in the Journal of Modern Optics.

V. A. Smalyuk, S. B. Dumanis, J. A. Delettrez, V. Yu. Glebov, D. D. Meyerhofer, S. P. Regan, T. C. Sangster, and C. Stoeckl, "Hot-Core Assembly in Cryogenic D_2 Direct-Drive Spherical Implosions," to be published in Physics of Plasmas–Brief Communication.

C. Stoeckl, V. Yu. Glebov, P. A. Jaanimagi, D. D. Meyerhofer, T. C. Sangster, M. Storm, S. Sublett, W. Theobald, M. H. Key, A. J. MacKinnon, P. K. Patel, D. Neely, and P. A. Norreys, "Operation of Target Diagnostics in a Petawatt Environment," to be published in Review of Scientific Instruments (invited).

S. Sublett, J. P. Knauer, I. V. Igumenshchev, A. Frank, and D. D. Meyerhofer, "Double-Pulse Laser-Driven Jets on OMEGA," to be published in Astrophysics and Space Science.

W. Theobald, J. E. Miller, T. R. Boehly, E. Vianello, D. D. Meyerhofer, T. C. Sangster, J. H. Eggert, and P. M. Celliers, "X-Ray Preheating of Window Materials in Direct-Drive Shock-Wave Timing Experiments," to be published in Physics of Plasmas.

A. Trajkovska, C. Kim, K. L. Marshall, T. H. Mourey, and S. H. Chen, "Photoalignment of a Nematic Liquid Crystal Fluid and Glassy–Nematic Oligofluorenes on Coumarin-Containing Polymer Films," to be published in Macromolecules.

Conference Presentations

V. A. Smalyuk, R. Betti, T. R. Boehly, J. A. Delettrez, V. Yu. Glebov, V. N. Goncharov, J. P. Knauer, D. Y. Li, R. L. McCrory, D. D. Meyerhofer, P. B. Radha, S. P. Regan, T. C. Sangster, S. Skupsky, J. M. Soures, C. Stoeckl, B. Yaakobi, O. Sadot, D. Shvarts, J. A. Frenje, C. K. Li, R. D. Petrasso, and F. H. Séguin, "Experimental Studies of Nonlinear, Directly-Driven, Rayleigh–Taylor Instability on OMEGA," 10th International Workshop on the Physics of Compressible Turbulent Mixing, Paris, France, 17–21 July 2006.

The following presentations were made at the International Conference on Computational Science and Education, Rochester, NY, 7–10 August 2006:

J. A. Delettrez, "A Survey of the Use of Computer Technology at the Laboratory for Laser Energetics."

P. B. Radha, "Modeling Inertial Confinement Fusion Implosions Through Large-Scale Simulations."

The following presentations were made at Optics and Photonics 2006, San Diego, CA, 13–17 August 2006:

T. Z. Kosc, K. L. Marshall, A. Trajkovska-Petkoska, C. J. Coon, and S. D. Jacobs, "Exploring Motion Reversal in Polymer Cholesteric Liquid Crystal Devices."

N. N. Lepeshkin, S. G. Lukishova, R. W. Boyd, and K. L. Marshall, "Feedback-Free, Single-Beam Pattern Formation by Nanosecond Pulses in Dye-Doped Liquid Crystals."

K. L. Marshall, A. G. Noto, G. Painter, and N. Tabirian, "Computational Chemistry Methods for Predicting the Chiroptical Properties of Liquid Crystal Systems. II. Application to Chiral Azobenzenes."

The following presentations were made at the Applied Superconductivity Conference 2006, Seattle, WA, 27 August–1 September 2006:

G. N. Gol'tsman, A. Korneev, O. Minaeva, A. Antipov, A. Divochiy, N. Kaurova, B. Voronov, D. Pan, A. Cross, A. Pearlman, I. Komissarov, W. Słysz, and R. Sobolewski, "Low-Kinetic-Inductance Superconducting Single-Photon Detectors for GHz-Rate and High Quantum Efficiency Counting of Infrared Photons."

M. Khafizov, X. Li, R. Sobolewski, Y. Cui, and X. X. Xi, "Mechanisms of Light Detection by Superconducting Current-Biased MgB_2 Microbridges."

J. Kitaygorsky, I. Komissarov, A. Jukna, R. Sobolewski, O. Minaeva, N. Kaurova, A. Korneev, B. Voronov, I. Milostnaya, and G. N. Gol'tsman, "Dark Counts in Nanostructured NbN Single-Photon Detectors and Bridges."

X. Li, M. Khafizov, R. Sobolewski, Š. Chromik, V. Štrbík, M. Valerianova, and P. Odier, "Ultrafast Carrier Dynamics and Photoresponse of Hg-Ba-Ca-Cu-O Superconducting Microbridges."

———

S. P. Regan, H. Sawada, D. D. Meyerhofer, R. Epstein, V. N. Goncharov, I. V. Igumenshchev, D. Li, P. B. Radha, J. A. Delettrez, T. R. Boehly, F. J. Marshall, T. C. Sangster, V. A. Smalyuk, B. Yaakobi, S. H. Glenzer, O. L. Landen, G. Gregori, and R. C. Mancini, "Diagnosing Shock-Heated and Compressed Matter in Direct-Drive Inertial Confinement Fusion (ICF)," 12th International Workshop on Radiative Properties of Hot Dense Matter, Albufeira, Algarve, Portugal, 11–15 September 2006.

———

The following presentations were made at Boulder Damage Symposium XXXVIII, Boulder, CO, 25–27 September 2006:

B. Ashe, K. L. Marshall, C. Giacofei, A. L. Rigatti, T. J. Kessler, A. W. Schmid, J. B. Oliver, J. Keck, and A. Kozlov, "Evaluation of Cleaning Methods for Multilayer Diffraction Gratings."

S. Papernov and A. W. Schmid, "Using Gold Nanoparticles as Artificial Defects in Thin Films: What Have We Learned About Laser-Induced Damage Driven by Localized Absorbers?"

———

The following presentations were made at ICUIL 2006, Cassis, France, 25–29 September 2006:

J. Bromage, C. Dorrer, I. A. Begishev, N. G. Usechak, and J. D. Zuegel, "Single-Shot Pulse Characterization from 0.4 to 85 ps Using Electro-Optic Shearing Interferometry."

J. Bromage, L. J. Waxer, I. A. Begishev, C. Dorrer, J. H. Kelly, and J. D. Zuegel, "Femtosecond Optimization of a Stretcher–Compressor Pair Using a Picosecond-Resolution Diagnostic."

C. Dorrer, A. Consentino, and J. D. Zuegel, "Development of High-Fluence Beam Shapers."

T. J. Kessler, J. Bunkenburg, C. Kellogg, F. Dewitt, J. Barone, L. S. Iwan, and K. McGowan, "Holographic Exposure System for Patterning Large Gratings with High Wavefront Quality and Uniform Groove Profile."

T. J. Kessler, H. Huang, and D. Weiner, "Diffractive Optics for Compensation of Axial Chromatic Aberration in a High-Energy Short-Pulse Laser."

L. J. Waxer and D. Eimerl, "Modeling the Pulse-Shape Output of OMEGA EP."

J. D. Zuegel, I. A. Begishev, W. A. Bittle, R. Boni, J. Bromage, C. Dorrer, P. A. Jaanimagi, and J. R. Marciante, "Laser and Diagnostic Technologies Developed for Integrated Pulse-Width Control on OMEGA EP."